

**Deeply Buried Nuclei in the Infrared-Luminous Galaxies NGC 4418 and Arp 220
II. Line Forests at $\lambda = 1.4\text{--}0.4$ mm and Circumnuclear Gas Observed with ALMA**KAZUSHI SAKAMOTO,¹ SERGIO MARTÍN,^{2,3} DAVID J. WILNER,⁴ SUSANNE AALTO,⁵ AARON S. EVANS,^{6,7} AND
NANASE HARADA^{1,8}¹*Academia Sinica, Institute of Astronomy and Astrophysics, Taipei, Taiwan*²*European Southern Observatory, Alonso de Córdova 3107, Vitacura Casilla 763 0355, Santiago, Chile*³*Joint ALMA Observatory, Alonso de Córdova 3107, Vitacura 763 0355, Santiago, Chile*⁴*Harvard-Smithsonian Center for Astrophysics, 60 Garden Street, Cambridge, MA 02138, USA*⁵*Department of Earth and Space Sciences, Chalmers University of Technology, Onsala Observatory, 439 92 Onsala, Sweden*⁶*Department of Astronomy, University of Virginia, P.O. Box 400325, Charlottesville, VA 22904, USA*⁷*National Radio Astronomy Observatory, 520 Edgemont Road, Charlottesville, VA 22903, USA*⁸*National Astronomical Observatory of Japan, Mitaka, Tokyo, 181-8588, Japan***ABSTRACT**

We present the line observations in our ALMA imaging spectral scan toward three deeply buried nuclei in NGC 4418 and Arp 220. We cover 67 GHz in $f_{\text{rest}}=215\text{--}697$ GHz at about $0''.2$ (30, 80 pc) resolution. All the nuclei show dense line forests; we report our initial line identification using 55 species. The line velocities generally indicate gas rotation around each nucleus, tracing nuclear disks of ~ 100 pc sizes. We confirmed the counter-rotation of the nuclear disks in Arp 220 and that of the nuclear disk and the galactic disk in NGC 4418. While the brightest lines exceed 100 K, most of the major lines and many ^{13}C isotopologues show absorption against even brighter continuum cores of the nuclei. The lines with higher upper-level energies, including those from vibrationally-excited molecules, tend to arise from smaller areas, indicating radially varying conditions in these nuclei. The outflows from the two Arp 220 nuclei cause blueshifted line absorption below the continuum level. The absorption mostly has small spatial offsets from the continuum peaks to indicate the outflow orientations. The bipolar outflow from the western nucleus is also imaged in multiple emission lines, showing the extent of $\sim 1''$ (400 pc). Redshifted line absorption against the nucleus of NGC 4418 indicates either an inward gas motion or a small collimated outflow slanted to the nuclear disk. We also resolved some previous confusions due to line blending and misidentification.

Keywords: Active galaxies (17), Interstellar medium (847), Galaxy nuclei (609), Luminous infrared galaxies (946), Galaxy winds (626), Interstellar molecules (849), Galaxy kinematics (602)

1. INTRODUCTION

The infrared-luminous galaxies NGC 4418 and Arp 220 have local prototypes of extremely obscured, luminous, and compact galactic nuclei. NGC 4418 ($D = 34$ Mpc; $1''=165$ pc) is an Sa-type galaxy having 8–1000 μm luminosity L_{IR} of $10^{11.2} L_{\odot}$ (Armus et al. 2009). Arp 220 ($D = 85$ Mpc; $1''=412$ pc) has $L_{\text{IR}} = 10^{12.3} L_{\odot}$ (Armus et al. 2009) and is a galaxy merger whose two nuclei are $\sim 1''$ apart from each other; we call the eastern nucleus Arp 220E and the western one Arp 220W. NGC 4418 is a luminous infrared galaxy (LIRG, $\log L_{\text{IR}}/L_{\odot} = 11\text{--}12$), and Arp 220

is the nearest ultraluminous infrared galaxy (ULIRG, $\log L_{\text{IR}}/L_{\odot} = 12\text{--}13$; Sanders & Mirabel 1996).

These nuclei have obscuring column densities as large as $\sim 10^{25}\text{--}10^{26}$ H cm $^{-2}$ (González-Alfonso et al. 2004, 2012; Downes & Eckart 2007; Sakamoto et al. 2008, 2013, 2021; Scoville et al. 2017; González-Alfonso & Sakamoto 2019; Dwek & Arendt 2020). They are bright and compact ($\lesssim 100$ pc) in imaging in mid-IR (Wynn-Williams & Becklin 1993; Soifer et al. 1999; Evans et al. 2003), submillimeter (Sakamoto et al. 2008, 2013; Wilsson et al. 2014), millimeter (Downes & Solomon 1998; Scoville et al. 2017; Sakamoto et al. 2017), and centimeter wavelengths (Norris 1988; Condon et al. 1990, 1991; Barcos-Muñoz et al. 2015). The compact nuclei gen-

erate the bulk of the vast infrared luminosities of the individual galaxies: it has been suggested by the high brightness temperature of the submillimeter dust emission, modeling of the spectral energy distribution (Soifer et al. 1999; Dwek & Arendt 2020), and that of far-IR spectroscopy (González-Alfonso et al. 2012).

Compact starburst and active galactic nucleus (AGN) have been the most plausible luminosity sources of the nuclei (see Baan et al. 1982; Soifer et al. 1984; Rieke et al. 1985; Roche et al. 1986; Rowan-Robinson & Crawford 1989, for early proposals). Vigorous star formation is evident by now in all three nuclei through groups of supernovae, supernova remnants, and super-star clusters seen as compact radio sources (Smith et al. 1998; Varenius et al. 2014, 2019). In contrast, AGNs in these extinguished nuclei have been difficult to detect and more so to quantify. For example, Veilleux et al. (2009) used six mid-IR diagnostics for the fractional AGN contribution to the bolometric luminosity in nearby ULIRGs and quasars. The AGN fraction ranges between 0 and <37% with a mean of <18% for Arp 220, while it is >50% in two of the diagnostics applied to NGC 4418 (Veilleux et al. 2009, 2013; Rosenberg et al. 2015). Meanwhile, the two galaxies are starburst templates in another infrared diagnostic of AGN (Fadda & Rodighiero 2014). We conservatively view AGNs in the three nuclei as likely but unproven possibilities. In any case, the nuclei of NGC 4418 and Arp 220 are our local prototypes of either the most extreme starbursts, most heavily obscured AGN that are still in dusty cocoons and hence young, or possible sites of starburst-AGN coevolution.

High-resolution imaging spectroscopy of these nuclei at millimeter and submillimeter wavelengths have proven useful to study their properties and evolution. It required sub-arcsec resolution CO images to find twin compact ($\lesssim 100$ pc) peaks of molecular gas at the two radio nuclei of Arp 220 (Scoville et al. 1997; Downes & Solomon 1998). A $0''.5$ resolution spectro-imaging was necessary to find them to be counter-rotating nuclear disks (Sakamoto et al. 1999). Molecular outflows from both nuclei were found from blueshifted absorption lines (below the continuum level) in each nucleus at $0''.3$ resolution (Sakamoto et al. 2009). The outflow from Arp 220W was estimated to be in the polar direction of the nucleus disk on the basis of a small spatial offset of SiO absorption (Tunnard et al. 2015). This configuration is consistent with the one based on a 150 MHz image of the nucleus (Varenius et al. 2016). The bipolar shape of this outflow has been imaged in the 3 mm continuum (Sakamoto et al. 2017) and molecular lines (Barcos-Muñoz et al. 2018; Wheeler et al. 2020). NGC 4418 also has a massive central reservoir of molec-

ular gas strongly concentrated to the central $\lesssim 100$ pc (Kawara et al. 1990; Imanishi et al. 2004; Sakamoto et al. 2013). A kpc scale polar outflow has been found in dust extinction while the molecular line profiles toward the nucleus were found skewed to suggest redshifted absorption (Sakamoto et al. 2013), which is also seen in infrared lines (González-Alfonso et al. 2012; Veilleux et al. 2013; Rosenberg et al. 2015). The detection of vibrationally-excited HCN toward the nucleus of NGC 4418 (Sakamoto et al. 2010, 2013) and the two nuclei of Arp 220 (Aalto et al. 2015; Martín et al. 2016) suggested hot dust and strong mid-IR radiation inside these nuclei for excitation to the levels ~ 1000 K above the ground.

The presence and properties of warm gas in the nuclei of NGC 4418 and Arp 220 have been also traced in far-IR and submillimeter lines using space-borne telescopes (e.g., González-Alfonso et al. 2004, 2012; Rangwala et al. 2011; Rosenberg et al. 2015). These observations with large apertures do not resolve the nuclei but recover some spatial information by the modeling of high-excitation molecular and atomic lines detected in a wide bandwidth, typically spanning ~ 0.5 dex. For example, radial gas motions are seen in Doppler-shifted absorption in NGC 4418 and Arp 220. The high-resolution imaging spectroscopy with ground-based radio interferometers is complementary to the far-infrared spectroscopy from space. The former would be more powerful if it has bandwidth as wide as in the latter.

We set out for high-resolution and wide-band imaging spectroscopy of NGC 4418 and Arp 220 using the Atacama Millimeter-Submillimeter Array (ALMA). In the observations reported here, we used ten frequency tunings to cover major lines and continuum emission in ALMA Bands 6, 7, and 9, sampling 67 GHz from the rest-frequency range of 215–697 GHz ($\lambda_{\text{rest}}=1.4\text{--}0.43$ mm) with a target resolution of $0''.2$. With the high angular resolution, about 30 and 80 pc at each galaxy, we can not only separately observe the two nuclei of Arp 220 and isolate the circumnuclear gas from the gas far out in the galaxy disks but also start to resolve the structures inside the three nuclei. Sakamoto et al. (2021, hereafter Paper I) reported in detail our ALMA observations, data reduction, and analysis of continuum emission of the three nuclei. The continuum emission is strongly concentrated in all three nuclei, and each nucleus needs a few concentric Gaussians to fit the intensity profile. Their core components are found to be as small as $\sim 0''.05$ (8–20 pc) and as bright as 200–500 K in deconvolved peak brightness temperature. Each nucleus also has an oval feature that is several times larger than the core and has its major axis aligned to the known gas velocity gradient in the nucleus; we iden-

tified it with the nuclear disk. We also detected extended features around the nuclei in dust emission at 0.4 mm. The most notable was a faint bipolar feature nearly perpendicular to the nuclear disk of Arp 220W. We identified it with the known bipolar outflow from the nucleus. Our continuum analysis also provided the dust opacities and through which the column densities in each nucleus. The nuclei of NGC 4418 and Arp 220W were estimated to be opaque at 1 mm. Their 1 mm dust opacities, between the center and the surface, are on the order of 1, which translates to $N_{\text{H}} \sim 10^{26} \text{ cm}^{-2}$ for the dust-opacity law we adopted. Arp 220E was found to be several times less opaque.

This paper presents line observations from our spectral scan toward the three deeply buried nuclei in NGC 4418 and Arp 220. It follows up our interferometric spectral scans on these galaxies at lower resolution (Costagliola et al. 2015; Martín et al. 2011) and our high-resolution sub/millimeter studies of these nuclei (Sakamoto et al. 2008; Costagliola et al. 2013; Aalto et al. 2015; Martín et al. 2016; Sakamoto et al. 2017, and those already mentioned). There is also a companion ALMA spectral scan of Arp 220 at $\sim 0''.6$ in Bands 6 and 7; a part of it is in Martín et al. (2016), and full results will be reported elsewhere. Our high spatial resolution allows a systematic line census in the immediate vicinities of the individual luminous nuclei, and our wide bandwidth helps line identification using multiple transitions of individual species. Features (e.g., outflow signatures) that are seen in multiple lines are more credible, and trends across many lines inform us about the gas conditions in the nuclei. With the combination of NGC 4418 and Arp 220, we expect that NGC 4418 having narrower lines than Arp 220 guide us to de-blend the broad lines in Arp 220. We also anticipate the comparison of the three nuclei to be informative. Beyond our initial line identification, we analyze such basic properties of the nuclei as their gas kinematics, nuclear disk and outflow structures, and relative configurations between the Arp 220 nuclei and between the nucleus and the main disk of NGC 4418. Some earlier observations based on limited frequency coverage are also reevaluated.

The outline of this paper is as follows. Section 2 recapitulates our observations and data reduction reported in Paper I. Section 3 describes our choice of fiducial (systemic) velocities for the nuclei and our initial line identification in the data. Section 4 presents continuum-subtracted images of the brightest lines, and describes the most noticeable features and properties of the three nuclei. They include the size-excitation relation among lines, velocity structure around each nucleus, outflows

from the nuclei, and vibrationally excited lines. Section 5 revisits some previous observations in which line-blending adversely affected the interpretation. Section 6 is for a summary of our findings and concluding remarks.

2. ALMA OBSERVATIONS AND DATA REDUCTION

Table 1 is a summary of our ALMA observations; see Paper I for a full description. We scanned 67 GHz from within $f_{\text{rest}}=215\text{--}697$ GHz in ALMA Bands 6, 7, and 9. Table 2 has the exact frequency coverages. The coverages on NGC 4418 and Arp 220 match in Band 7 and have minor differences in Band 6 and 9 mainly to help continuum measurements. We observed a single position in each galaxy. The full width at half maximum (FWHM) of our primary beam ranges between $24''$ to $8''$ in our observing frequencies. Our target resolution was $0''.2$ and the achieved resolution ranged between $0''.14$ and $0''.28$ while the largest beam major-axis was $0''.35$. The data were recorded at the frequency resolution of 0.98 MHz so that they can be flexibly binned later for individual purposes. The data sensitivity for a 50 km s^{-1} resolution is typically 0.3–0.6 K at the native resolution (of $0''.14\text{--}0''.28$) and 0.1–0.2 K in the data smoothed to $0''.35$ resolution.

We calibrated the data of ten tunings for each galaxy with special emphasis on consistency. We aligned astrometry through self-calibration using common models and aligned flux scaling through flux self-calibration (i.e., adjustment of flux scales of adjacent tunings using small overlaps between them.) We constructed continuum models using measurements at rare gaps in the line forest and subtracted the models from our data for consistent continuum subtraction. Details of these calibrations are in Paper I.

3. SYSTEMIC VELOCITIES AND LINE IDENTIFICATION

The first step toward line identification is to determine the systemic velocities of the targets. The observed spectra are then presented in the rest frequency and compared with simulated spectra for line identification.

3.1. Systemic Velocities

We adopt fiducial systemic velocities of 2100 km s^{-1} for NGC 4418, 5400 km s^{-1} for Arp 220E, and 5300 km s^{-1} for Arp 220W. They are in the LSRK frame and the radio convention, i.e., $v = (\nu_{\text{obs}} - \nu_{\text{rest}})/\nu_{\text{rest}}$. We decided these velocities by averaging the spectra of several brighter lines to minimize the biases due to blended lines and skewed line profiles caused by, e.g., self-absorption. Figure 1 shows the continuum-subtracted spectra of the

lines toward the three nuclei, plotted against the LSRK velocities and normalized with the peak intensities. The line names are in the figure legend. The spectra of NGC 4418 are from our 0'35 data sampled in a 1''-diameter aperture. The line profiles of Arp 220 were taken from our companion spectral scan reduced in the same way since it covers a wider frequency range and contains more lines though at lower angular resolution. It is evident in the figure that line shapes vary much among the lines for each nucleus, reflecting at least the blending of nearby lines and variation of absorption and excitation conditions. We therefore averaged the normalized spectra for each nucleus to reduce the line-shape distortion. The mean line profiles are also shown in Fig. 1 with black lines. We measured, for each nucleus, the central velocity of the mean line profile at 20, 30, 40, and 50 % of its peak. The measured central velocities are shown as vertical line segments in Fig. 1. These intermediate levels help avoid the self-absorption evident at higher levels toward the Arp 220 nuclei. In addition, the mean profiles at these levels should be less affected by adjacent lines and asymmetric line wings, if any, than at lower levels. The central velocities agree well among the four levels, and therefore, the fiducial velocities decided from them through averaging and rounding should be precise to about 10 km s^{-1} . A systemic error is possible if a nucleus has a lopsided distribution of gas or gas properties, although we used larger apertures than our data resolution allows to reduce the effect of any small-scale asymmetries. For better systemic velocities, one needs to properly de-blend lines and model any intrinsic asymmetries and radial motion of the molecular gas around the individual nuclei.¹

For comparison, Sakamoto et al. (2013) estimated for NGC 4418 the central velocity of 2100 km s^{-1} with CO and 2088 km s^{-1} with several other dense gas tracers, noting that the latter may be closer to the true systemic velocity of the nucleus. Martín et al. (2016) estimated the systemic velocities of the eastern and western nuclei of Arp 220 to be 5454 and 5342 km s^{-1} , respectively, from $\text{HCO}^+(3-2)$ line profiles toward the nuclei. Both are about 50 km s^{-1} larger than what we adopt here. We excluded HCO^+ in our velocity analysis above because it blends with bright $\text{HCN}(v_2 = 1, l = 1f)$

on the redshifted side and has deep absorption on the blueshifted side.

3.2. Initial Line Identification

We identified lines through a comparison between the observed and synthesized spectra. Rather than individually identifying lines with their frequencies alone, we modeled all transitions of each species together to add the lines to our model. Their relative line intensities were calculated with assumptions of the local thermodynamic equilibrium (LTE) and that all lines originate from the same slab of isothermal gas. We employed for this analysis the MADCUBA/SLIM software (Martín et al. 2019) that allows iterative line identification and spectral fitting through the successive generation of synthetic spectra using all identified and fitted species. We used our NGC 4418 spectrum at 0'35 resolution from Bands 6 and 7 because this nucleus has a much narrower linewidth than the Arp 220 nuclei and hence suffers less from line-blending. The Band 9 spectrum was not used for simultaneous fitting because it has less accurate flux calibration, a small number of lines, and more continuum absorption. Acknowledging that the isothermal slab is not a good model for our target nuclei, we still show our line identifications hoping it to be an instructive starting point. Appendix A lists lines and species in our initial model for NGC 4418 and compares the observed and model spectra.

Figures 2, 3, and 4 show our continuum-subtracted spectra with labels for major identified lines as well as some lines of interest. Many lines are observed with similar relative strengths among the three nuclei, though some show notable differences. As we intended in our target selection, NGC 4418 serves as a good reference to disentangle the heavily blended lines in Arp 220. For comparison, the previous interferometric spectral scans at lower resolution by Costagliola et al. (2015) for NGC 4418 and Martín et al. (2011) for Arp 220 also provided line identifications. Comparing their spectra and ours, as well as our 0'2 and 0'35 spectra in Band 7 (Fig. 3), it is evident that relative line strengths depend on spatial resolution. So does the degree of self-absorption and continuum absorption. This resolution dependence indicates a radial variation of ISM conditions in these nuclei, and we will see it again in Section 4.2.1.

4. SPECTRAL LINE ANALYSIS

We made spectral line images using the visibility data from which our continuum models constructed in Paper I had been subtracted. Figures 5 through 10 show the channel maps of major lines in our data for a 50 km s^{-1}

¹ It would be rather complex. For example, Arp 220W has double-peaked profiles in many lines but the brighter peak is the redshifted one in CO and the blueshifted one in HCN and CS while HNC shows single-peaked profiles. Such a nucleus requires a model more complicated than having an $m = 2$ symmetry of a single gas parameter.

resolution and `robust` = 0 for the imaging. Table 3 has their parameters, including the peak brightness temperatures (peak T_b) and information on major nearby lines that may be blended. The tabulated peak T_b may be biased low because of the continuum subtraction; we explain it in Section 4.1. These peak T_b measured in the image domain suffer from beam dilution, unlike the continuum peak T_b from visibility fitting.

Figures 11 and 12 show integrated intensity images of NGC 4418 and Arp 220, respectively. For NGC 4418, we integrated channels from 1900 to 2300 km s^{−1} for a total $\Delta V = 450$ km s^{−1}, except for the two lines noted in the caption. For Arp 220, we integrated channels from 4850 to 5850 km s^{−1} for a total $\Delta V = 1050$ km s^{−1}. Figure 13 also shows the CO(2–1) and (3–2) integrated-intensity images of the two galaxies in larger areas. Figures 14 and 15 show the mean velocity images of selected lines.² We describe below our observations in these data.

4.1. Cautions about Continuum Subtraction and Line Blending

We start from cautions about continuum subtraction and line blending. These have become acute issues in extragalactic spectral scans with the angular resolution and sensitivity of ALMA.

While we subtracted our modeled continuum emission from our line data, the necessity for the subtraction itself is a complex issue. The continuum subtraction is undoubtedly necessary for any channels where the continuum nucleus and line-emitting gas have no overlap on the sky. The necessity is not evident for the channels where the continuum nucleus is covered by a foreground line-emitting gas whose line emission is optically thick. In this situation, the source has its line photosphere outside its continuum photosphere. If the continuum emission from outside the line photosphere is negligible, then we only detect line photons (i.e., those from molecules) and detect no continuum photons that need subtraction. There are also intermediate situations, e.g., partial cov-

erage of the continuum source and optically thin line emission on top of optically thin dust-continuum emission from the same interstellar cloud. For simplicity, we subtracted the continuum from all the channels using our Gaussian source models with power-law spectra (Paper I). The continuum models have no correction for an occultation of the continuum emission by line-emitting gas. Therefore, a line-emitting gas that completely covers the continuum source would have zero (or a negative) intensity if the line is optically thick and has the same (or a lower) brightness temperature compared to the background continuum. Therefore, the lack of positive emission toward a continuum nucleus in our continuum-subtracted line image does not necessarily mean a lack of line emission (and molecular gas) on the sightline to the nucleus. For analytic expressions of this issue, see Wilson et al. (2009, §13.4.1) and Martín et al. (2019).

Lines are blended not only in our spectra (Figs. 3 and 4) but also in our channel and integrated-intensity maps. The line-blending is more severe in Arp 220 than in NGC 4418 because the lines are broader in the former. For example, H¹³CN(4–3) is evident in the CO(3–2) channel maps in Fig. 6(g). Much of the emission within 0''.5 of the western nucleus in the 5700 km s^{−1} channel (and adjacent channels) must be H¹³CN(4–3). Indeed, that CO velocity corresponds to 5311 km s^{−1} for H¹³CN(4–3). Moreover, the emission shape around the W nucleus agrees very well with those in the 5300–5350 km s^{−1} channels of other dense gas tracers such as HCN(4–3) and CS(7–6) in Figs. 6(d) and (h). What is worse, CO(3–2) probably has a minor but non-zero contribution to the (circum)nuclear emission at 5700 km s^{−1} (and in adjacent channels) around the western nucleus judging from CO(2–1) channel maps in Fig. 7(a). Thus CO(3–2) and H¹³CN(4–3) must coexist around this location in the observed position-position-frequency space. Therefore, we cannot separate the two by simply applying a three-dimensional mask made from the CO(2–1) information. Major cases of line-blending are listed in Table 3, and the line list in the Appendix suggests more. As we see below multiple times, consideration for line blending is often crucial for data interpretation at the level of line density in our data.

4.2. Spatial Distribution around the Nuclei — Multi-line Comparison

We find that the size of the emitting region varies among lines with certain trends. This finding has implications on the radial structure in the nuclei, the analysis of multi-line data, and our choice of lines to probe these nuclei.

4.2.1. Size variation of line-emitting regions

² We define the mean velocity at each position as

$$\langle v \rangle = \frac{\sum_i |I_i| v_i}{\sum_i |I_i|}, \quad (1)$$

where I_i is the intensity in the i -th channel at velocity v_i . We use the absolute value of intensity here because both emission and absorption are in our continuum-subtracted image cubes. The summations are over channels with significant detection of either emission or absorption. The detection criterion was that the absolute value of intensity is above a threshold in the reference data cube that was made by smoothing the original data cube to about 1.5 to 2 times the original spatial resolution. We used the masking threshold of 2.5σ , where σ is the rms noise in each original cube.

Molecular line emission in our images tends to be sharply peaking toward the three continuum nuclei, with some lines showing decrement or absorption on the continuum peaks. The size of the line emitting region varies among the lines. In both galaxies, the line-detection areas are by far the largest for CO. It is consistent with our SMA analysis that CO emission is more extended than other lines in these galaxies (Sakamoto et al. 2009, 2013). Among the non-CO lines, the emission lines from vibrationally excited molecules, such as $\text{HCN}(v_2=1)$, have much more compact distributions than the other ordinary lines (i.e., transitions within the vibrational ground state). In NGC 4418, the compactness of the vibrationally-excited line emission is seen in both the channel maps and the integrated intensity images. In Arp 220, the compactness of $\text{HCN}(v_2=1)$ emission is better seen in the channel maps at $V \gtrsim 5300 \text{ km s}^{-1}$, where the line is not blended with the adjacent $\text{HCO}^+(v=0)$ line. In short, the size of the line-emitting area has the following apparent trend: $\text{CO} > \text{other lines without vibrational excitation} > \text{lines from vibrationally excited states}$.

Figure 16 plots the extent of the emitting regions in FWHM for major lines in the nuclei of NGC 4418 and Arp 220. The deconvolved source sizes are plotted against the upper-state energies of the lines. We use the FWHM to characterize source size to avoid the bias that a faint source appears smaller than a bright source of the same size and shape if evaluated at the same absolute intensity (e.g., at the 3σ contours). Even the weaker lines in the plot have high signal-to-noise ratios; $S/N = 47, 66, 97, 110$, and 115 respectively for $\text{SiO}(8-7)$, $\text{HN}^{13}\text{C}(4-3)$, $\text{HCN}(v_2=1,4-3)$, $\text{C}^{18}\text{O}(2-1)$, and $\text{H}^{13}\text{CO}^+(4-3)$ in the integrated intensity maps of NGC 4418. Hence their FWHM have only small errors due to thermal noise. The formal errors of the plotted FWHM are at most the size of the plotting symbols. We measured the source FWHM in two ways for NGC 4418 and found them generally consistent. For Fig. 16a, we used Gaussian fitting of the continuum-subtracted integrated intensity images (Fig. 11). For Fig. 16b, we used visibility fitting with a Gaussian source model for the line+continuum data within 100 km s^{-1} of the systemic velocity; we already fitted our entire spectral scan in visibilities in Paper I. We used the latter method for the nuclei of Arp 220 in Fig. 16c and d. It mitigates the effect of line-blending by only using channels close to V_{sys} and avoids absorption and ring-like structure by not subtracting continuum.

Figure 16 confirms our visual observation that emission from vibrationally excited molecules is compact. It also reveals two general trends. First, the line-emitting regions are smaller for lines whose upper-level energies

are higher; lines from vibrationally excited levels are extreme cases in this trend. Second, the line-emitting regions are also smaller for lines of less abundant molecules for similar upper-level energies; rarer isotopologues and ^{12}CO lines are at the opposite ends of this trend. All three nuclei show these trends, except that the lines of rare isotopologues in Arp 220 are too heavily blended with nearby brighter lines to be reliably measured for their emitting regions.

The two trends in the size of the line-emitting regions must be because the excitation conditions for the transitions from higher energies and for less abundant species are achieved only at locations (or on sight-lines passing) closer to the center of each nucleus. The bright continuum emission sharply peaking toward the center of each nucleus also suggests such radial variation in physical conditions (Sakamoto et al. 2017, 2021). Parameters that are very likely to have radial variations include the following; gas density, gas temperature, and radiation field for radiative excitation (both through a vibrationally-excited state by IR radiation and within the vibrational ground level by millimeter-submillimeter radiation). The latter two are most likely to be higher toward the center (e.g., González-Alfonso et al. 2012; Scoville et al. 2015; González-Alfonso & Sakamoto 2019; Wheeler et al. 2020). Radial variations are also expected in chemical abundance (Harada et al. 2010).

4.2.2. Lines to Probe the Nuclei

Our observations on the size variation of line-emitting regions tell us about the choice of lines and line combinations to better probe galaxy nuclei similar to our three targets. The size of the line-emitting areas approaches from above (i.e., decreases) to the size of the continuum emission as the upper-energy level increases or the molecular abundance decreases. This tendency makes lines from very high energy levels and rare isotopologues better probes of the innermost structure of the nucleus, down to the radius at which either the continuum or line emission becomes optically thick. In particular, the lines from vibrationally excited molecules, having the highest upper-level energies in our data, should be the most suitable of lines to probe the warm compact nuclei. We will discuss their usage in §4.5.

The size variation of the line-emitting regions also cautions that line ratios require careful interpretation for these galactic nuclei. The simplest one-zone modeling has problems in the following assumptions, 1) that the compared lines are from the same volume and hence have the same beam-filling factors, and 2) that the physical conditions are uniform across each nucleus. This complexity is a major obstacle to spectral modeling and

line identification. It is the reason why we regard our line identification in this paper as an initial attempt.

4.3. Velocity Structures around the Nuclei

The channel maps and the mean velocity maps show rich velocity structures in and around the nuclei. The most notable are the following.

4.3.1. NGC 4418 — Counter-rotating nuclear disk and turbulent gas around it

A general velocity structure in the nucleus of NGC 4418, seen in the channel maps of, for example, $\text{HCO}^+(4-3)$, $\text{HCN}(4-3)$, $\text{CO}(3-2)$, and $\text{CS}(7-6)$, is a southwest-northeast velocity gradient in the nucleus. The brightest line emission is offset (by $\lesssim 0''.3$) from the continuum position to the southwest in the low-velocity channels up to 2100 km s^{-1} and the northeast at higher velocities. The offset is smaller or not visible in the channels furthest from the systemic velocity. This velocity structure becomes less visible at lower angular resolution ($\gtrsim 0''.25$) and in lines with smaller spatial extents. The velocity gradient is in the direction of the elongation of the integrated intensity for the same lines. It is confined to the central 100 pc (i.e., $r \lesssim 50 \text{ pc}$) of the nucleus, as seen in the channel maps and the mean velocity image of $\text{HCN}(4-3)$ in Fig. 14.

The circumnuclear velocity gradient was first reported in Sakamoto et al. (2013) and was attributed to gas rotation around the nucleus. They inferred a rotation curve in the nuclear gas disk to rise toward smaller radii from the observation that lines with higher critical densities having larger line widths. Although that alone can also be explained by the combination of higher velocity dispersion and higher gas densities toward the center, our new observation of larger spatial offsets closer to the systemic velocity supports the rising rotation curve toward the center. The rotation curve at the very center should be better studied in the lines that most strongly peak toward the center, such as lines from vibrationally excited molecules. The non-detection of velocity offsets in these lines in our current channel maps is probably because the line-emitting regions are too small compared to our angular resolution and presumably also because of high continuum opacity toward the nucleus.

Although the observed southwest-northeast velocity gradient in the close vicinity of the nucleus is roughly parallel to the major axis of the galaxy (position angle = 60° ; Jarrett et al. 2000), the direction of velocity gradient is opposite to that of the stars and atomic gas in the disk of the galaxy. The galactic disk rotates in such a way that its northeast side is blueshifted and the southwest side redshifted (Ohyama et al. 2019). By confirming the nuclear velocity gradient of molecular gas in

Sakamoto et al. (2013), our new data strengthen the surprising finding of Ohyama et al. (2019) that the kpc-scale galactic disk and the nuclear gas disk counterrotate with each other.

The velocity field of molecular gas outside the nuclear disk is highly disturbed without a regular butterfly pattern of a rotating disk in Figs. 6l, 7f, and the CO mean velocity maps in Fig. 14. The kpc-scale bipolar outflow from the galactic center (Sakamoto et al. 2013; Varenius et al. 2017; Ohyama et al. 2019) is a likely source of this disturbance, but a simple bipolar pattern of high-velocity emission is not evident in our CO images. An outflow has also been inferred from $\text{CO}(2-1)$ and $(1-0)$ line wings in the central $\sim 5'' - 1''.4$ (Fluetsch et al. 2019; Lutz et al. 2020). While the CO wing emission is not evident in our spectral decomposition of the central $0''.35$ (Fig. 27 in the Appendix), dense gas tracers such as HCN , HCO^+ , HNC , and CCH show some broad emission in the residual spectrum, consistent with their larger line widths than CO noticed in SMA observations (Sakamoto et al. 2013). The large gas velocities can be due to an outflow, turbulence, or rotation near the nucleus. If it is due to an outflow, its current extent in these dense-gas tracers must be small since no extended outflow is visible in our channel maps. Other likely sources for the disturbed velocity field at 0.1–1 kpc scale are possible gas infall from a companion galaxy (Varenius et al. 2017) and gas supply from the outer disk of NGC 4418 through tidal torquing by the passing companion galaxy (Boettcher et al. 2020). We will note in §4.4.1 signs of radial gas motion toward the nucleus. Combining all these observations, NGC 4418 has surprisingly disturbed kinematics of molecular gas in its central kpc despite its undisturbed optical appearance at first sight.

4.3.2. Arp 220 — Two nuclear disks and a prominent bipolar outflow from the western nucleus

In the channel maps of Arp 220, we see a gradual spatial shift with velocity in line emission around each nucleus. The shift from lower to higher velocities is from southwest to northeast around Arp 220E, while it is from east to west around Arp 220W. The mean velocity maps in Fig. 15 also show the velocity gradients across the individual nuclei in CO and HCN. This velocity structure has been attributed to two rotating nuclear disks in the individual galactic nuclei with misaligned rotational axes and apparent counter-rotation (Sakamoto et al. 1999; Scoville et al. 2017). The velocity structure around the western nucleus appears to be also present in the vibrationally excited HCN lines in their redshifted halves, while their blueshifted halves are severely contaminated by the blending HCO^+ .

The western nucleus also shows emission elongated to the south (north) at the velocities about 200–450 km s⁻¹ lower (higher) from the systemic velocity of 5300 km s⁻¹. For example, see the channel maps of HCN(4–3) and CO(2–1). This feature corresponds to the bipolar outflow from the western nuclear disk imaged at 0''.1 resolution in both 3 mm continuum and line emission by Sakamoto et al. (2017) and Barcos-Muñoz et al. (2018), at 0''.2 in CO(3–2) by Wheeler et al. (2020), and at 0''.5 in 150 MHz continuum emission by Varenus et al. (2016). Figure 17 presents this outflow by plotting high-velocity emission in HCN(4–3) and CO(2–1), (3–2), and (6–5). The extent of the outflow in these maps is about 0''.5 (200 pc) on the sky in each direction. The HCN plot is for a lower velocity offset from the systemic, and it shows a mixture of the nuclear disk component with the east–west velocity gradient and the outflow component with the north–south velocity gradient. The CO(3–2) and (6–5) data are plotted only for the blueshifted emission because the redshifted emission is contaminated by H¹³CN. These high-velocity emissions are aligned to the outflow axis that we measured to be p.a. = –15° in the $\lambda = 3$ and 0.45 mm continuum emission (Paper I). The outflow is warm and dense enough to be visible in HCN(4–3) and CO(6–5). This outflow also appears as the diamond shapes of molecular emission around the western nucleus in most of the integrated intensity maps in Fig. 12.

We leave our discussion on the molecular outflow from the eastern nucleus to Section 4.4.3. Although the outflows from the eastern and western nuclei were found using the same technique, i.e., blueshifted absorption in HCO⁺ (Sakamoto et al. 2009), the one from the eastern nucleus is not as evident in line emission as the one from the western nucleus.

Around the two nuclei is a larger-scale structure shown in Fig. 13 and referred to as the outer disk. The CO mean velocity maps in Fig. 15 show that while the outer disk has an overall velocity gradient in the northeast–southwest direction, its velocity field is disturbed. This disturbance must be partly due to the nuclear disks and the molecular outflows. In addition, the outer disk itself is expected to be disturbed in the merging galaxy.

4.4. Absorption Lines and Skewed Line Profiles

The three nuclei have many absorption features that tell us about the gas along the sightlines to the nuclei. Most notably, asymmetric absorption in frequency (i.e., in the spectral line profiles) and space (i.e., absorption offset from the central continuum peak) indicates gas motion that is otherwise hard to detect. As noted in Section 4.1, the continuum we subtracted from our line data

has simple power-law spectra and constant shapes over wide frequency ranges. They do not artificially cause frequency-dependent features that vary within a single line.

4.4.1. NGC 4418 — Skewed Line Profiles and Absorption toward the Nucleus

Figure 18 provides an updated view of the skewed line profile in the center of NGC 4418 reported in Sakamoto et al. (2013). At the top and in black is the normalized-and-stacked line profile in the central 1''. It is the profile that we used to estimate the systemic velocity. It is symmetric about the adopted V_{sys} of 2100 km s⁻¹. The normalized line profiles below (and in color) are from individual lines and smaller apertures. They are skewed more in lower profiles. The second from the top is ¹³CO(2–1). Although the profile is nearly symmetric about V_{sys} , it peaks at a slightly lower velocity and has a longer tail in higher velocities. The CO(2–1), (3–2), and (6–5) profiles below are progressively more skewed in the same manner. The HCN(4–3) and HCO⁺(4–3) profiles below have their peaks at ~ 2000 km s⁻¹. The former is flat between 2100 and 2200 km s⁻¹. The latter shows an absorption-like minimum at around 2150 km s⁻¹. This HCO⁺(4–3) profile reminds us that its continuum absorption is the deepest among the absorption features toward Arp 220E and W in Bands 6 and 7 (Figs. 3, 4). At the bottom of Fig. 18 is the very deep CN(6–5) absorption near $f_{\text{rest}} = 680$ GHz.³ Similar to the case of HCO⁺(4–3), the deepest absorption is between 2100 and 2150 km s⁻¹ and is hence slightly redshifted from V_{sys} . This spectrum is normalized by the continuum intensity, and as much as 60% of the continuum emission is absorbed. The CN optical depth would be 0.9 for a foreground absorber having a covering factor of unity. The CN absorption is broad, covering both sides of V_{sys} over at least 250 km s⁻¹, although this is partly because this CN feature consists of twelve transitions spanning 126 km s⁻¹. Our Band 9 data on Arp 220 do not cover CN(6–5), but deep CN absorption has been observed toward both nuclei in N=3–2 and 1–0 (Scoville et al. 2015; Sakamoto et al. 2017).

We attribute, as in Sakamoto et al. (2013), the skewed line profiles to absorption. It is probably a combination of self-absorption of the lines and line absorption of the background continuum. The near-symmetric ¹³CO line

³ It is a blended feature of N=6–5 doublet of $J = \frac{11}{2} - \frac{9}{2}$ and $\frac{13}{2} - \frac{11}{2}$, each of which contains six hyperfine features, spanning 126 km s⁻¹ in total. We used for our velocity labeling the weighted-mean frequency of the twelve transitions using $g_u A$ for the weighting, where g_u is the statistical weights of the upper state and A is the Einstein A coefficient.

profile strengthens this interpretation. Our observations do not favor an alternative model for the skewed CO(2–1) profile to introduce two emission components at different velocities (Costagliola et al. 2013). The profiles of other lines should be similar to CO(2–1) if there were two emission components and no absorption. In addition, the redshifted CN absorption has negative intensities in the continuum-subtracted spectra. They cannot be explained either by two gas velocities without absorption or by line self-absorption only. The redshifted absorption is also in O I, OH, and H I toward NGC 4418 (González-Alfonso et al. 2012; Costagliola et al. 2013).

The redshifted absorption is most easily interpreted as an inward gas motion toward the nucleus along our sightline (González-Alfonso et al. 2012; Sakamoto et al. 2013). It does not necessarily mean a net gas inflow to the nucleus since the circumnuclear gas may have outward motions in directions other than our sightline. We point out in §4.4.3 that the redshifted absorption can also be due to an outflow when the background continuum is not a point source but a disk.

We also detected, for the first time for NGC 4418, SiO absorption around the systemic velocity. The continuum-subtracted SiO(8–7) intensity goes below zero at the center of the nucleus at $\lesssim 0''.2$ resolution in Figs. 6j and 3. SiO(16–15) also shows sub-continuum absorption. It has a broad wing in blueshifted velocities (Figs. 2 and 5). The minima of the SiO spectra are around the fiducial systemic velocity or slightly blueshifted from it in the two transitions. The absorption velocities may be, however, affected by the nearby H^{13}CO^+ lines in redshifted velocities. The large width of more than 100 km s^{-1} in the SiO(16–15) absorption is consistent with the broad CN(6–5) absorption. Judging from the large width and the need for high excitation, it is more likely that the absorbing gas is inside the nucleus rather than a gas that happens to be on our sightline to the nucleus but is far from it. The SiO(16–15) absorptions in NGC 4418 and Arp 220 are discussed in Section 4.4.4.

4.4.2. Arp 220 — Absorption-line Systems toward the Nuclei

Figure 19 presents absorption features in the continuum-subtracted line profiles of the two Arp 220 nuclei. We selected lines showing significant absorption of the continuum (i.e., negative intensities in the continuum-subtracted data) toward at least one nucleus and supplemented them in panel (d) with spectra of some $\sim 3 \text{ mm}$ lines from Sakamoto et al. (2017). Both nuclei show sub-continuum absorption in blueshifted velocities, confirming our first report (Sakamoto et al. 2009) and companion ALMA observations (Martín et

al. 2016). It is evident in, e.g., CO(6–5), $\text{HCO}^+(4-3)$, and HCN(4–3). The blueshifted absorption has also been seen toward both nuclei in molecular lines at $\lambda \sim 1 \text{ cm}$ (Zschaechner et al. 2016).

Arp 220W:—On closer inspection of the new high-quality spectra, we see toward Arp 220W absorption features of distinct properties at two velocities. One is a narrow absorption feature seen in CO at around 5330 km s^{-1} . It is most evident in the CO(3–2) spectra in panel (a). As in this example, we denote an absorption feature with the velocity of its minima, V_{\min} . We caution that V_{\min} , in general, differs from the central velocity of the absorber, V_{abs} . For the latter, one needs to decompose an observed spectrum to emission and absorption features, e.g., by assuming a Gaussian profile for each component (Martín et al. 2016).⁴ However, this 5330 km s^{-1} feature is so narrow that the velocity-shifting effect by other spectral components must be small, hence $V_{\min} \sim V_{\text{abs}} \sim 5330 \text{ km s}^{-1}$. Therefore, this feature is close to but about 30 km s^{-1} redshifted from our fiducial velocity of the western nucleus. This feature has negative intensities (i.e., continuum absorption) in our CO(6–5) and $0''.2$ CO(3–2) data. This feature is also discernible as narrow troughs in our $0''.35$ CO(3–2) spectrum and CO(2–1) and (1–0) profiles, although the minimum intensities are still positive. Given the agreement in V_{\min} and similar widths, we regard these to be the same ‘ 5330 km s^{-1} absorption feature’ toward Arp 220W. We note that the apparent absorption depth depends not only on the line opacity but also on the angular resolution and observing frequency. It is because deep absorption against a compact continuum source can be filled with off-nuclear emission when both are in the same beam and also because the continuum brightness and source size vary with frequency. The effect of the angular resolution is evident when comparing the $0''.2$ and $0''.35$ spectra of CO(3–2) in panel (a). This 5330 km s^{-1} absorption feature is not evident in other species, except possibly in $\text{HCO}^+(3-2)$ and CN(1–0, 3/2–1/2).

Another absorption feature toward Arp 220W is the broad absorption having $V_{\min} \sim 5200\text{--}5250 \text{ km s}^{-1}$, most clearly seen in $\text{HCO}^+(4-3)$ in panel (b). We call it the 5230 km s^{-1} feature for brevity. This feature is unambiguously blueshifted compared with the W nucleus by

⁴ If a line profile is the sum of a Gaussian emission centered at the systemic velocity and a Gaussian absorption feature, then the absorption minimum in the observed line profile is further from the systemic velocity than the central velocity of the absorbing gas; $|V_{\min} - V_{\text{sys}}| \geq |V_{\text{abs}} - V_{\text{sys}}|$. It is because the emission component acts like a non-flat spectral baseline to the absorption line profile.

about 130 km s^{-1} and is much broader than the $\sim 5330 \text{ km s}^{-1}$ feature. The 5230 km s^{-1} feature shows negative intensities (i.e., continuum absorption) in Fig. 19 in CO(6–5), H^{13}CN , HCO^+ , $\text{HCN}(4-3)$, SiO, CS, H_2CO , and CN. Note in particular the $\text{H}^{13}\text{CN}(8-7)$ and $(4-3)$ absorption lines. They have $V_{\min} \sim V_{\text{sys}}(\text{W}) - 100 \text{ km s}^{-1}$ as other 5330 km s^{-1} features do, and hence the absorption features are not due to redshifted CO at $V_{\min} \sim V_{\text{sys}} + 300 \text{ km s}^{-1}$. The 5230 km s^{-1} feature is also visible as troughs at positive intensities in CO(3–2) at $0''.2$, HNC, and $\text{HCN}(3-2)$. As noted above, the positive intensities must be partly due to the data resolution. Indeed, the HNC(4–3) channel maps in Fig. 9(a) show negative intensity on the W nucleus in the 5200 km s^{-1} channel. The 5230 km s^{-1} absorption feature has an apparent FWHM of $\sim 200 \text{ km s}^{-1}$ in $\text{HCO}^+(4-3)$ in panel (b). Because of that, a part of this feature extends to the redshifted velocities of the W nucleus. The same is seen at least in $\text{H}^{13}\text{CN}(8-7)$, HCO^+ , $\text{HCN}(4-3)$, SiO, CS, and CN(1–0).

The western nucleus, therefore, has an absorption line system of two components. One is the narrow feature at $V_{\min} \sim 5230 \text{ km s}^{-1}$ seen in CO. The other is the broad feature at $V_{\min} \sim 5330 \text{ km s}^{-1}$ seen in CO and many other lines. Although at a much lower signal-to-noise ratio, we already recognized both absorption features in our SMA observations (Sakamoto et al. 2009). The only feature we do not confirm is their 4890 km s^{-1} feature. In our new ALMA observations with much higher data quality and wider frequency coverage, the relative strength of the two absorption features significantly varies with molecular species, line transitions, observing frequencies, and angular resolution.

Arp 220E:—The eastern nucleus of Arp 220 has a broad feature of negative intensity with minima at $V_{\min} \sim 5350 (\pm 50) \text{ km s}^{-1}$ in CO(6–5), HCO^+ , $\text{HCN}(4-3)$, and CN in Fig. 19. In addition, troughs of positive intensities are seen at similar V_{\min} and have comparable widths in such lines as CO(3–2) and (2–1), HNC, and $\text{HCN}(3-2)$. The presence of absorption is unambiguous in the former group of lines. Therefore, it is more sensible to attribute the troughs of positive intensities in the latter group of lines to absorption (line self-absorption and or continuum absorption) than to uneven distribution of gas parameters such as lower gas temperature in blueshifted velocities. Consequently, we regard these features as the ‘ $V_{\min} \sim 5350 \text{ km s}^{-1}$ absorption’ toward Arp 220E. This absorption was also first found with the SMA (Sakamoto et al. 2009).

The V_{\min} of all sub-continuum absorptions are lower than the V_{sys} of the nucleus, indicating $V_{\text{abs}} < V_{\text{sys}}$. The line profiles having troughs of positive intensities

at $\sim 5350 (\pm 50) \text{ km s}^{-1}$ are generally asymmetric in the sense that they have significantly higher peaks in redshifted velocities (i.e., $V > V_{\text{sys}}$) than in blueshifted velocities, also implying a blueshift of the absorption. The width of the $\sim 5350 \text{ km s}^{-1}$ absorption feature is comparable to that of the ‘broad’ 5230 km s^{-1} feature toward the western nucleus. As in the case of the $\sim 5230 \text{ km s}^{-1}$ feature toward the W nucleus, negative intensities of the broad $\sim 5350 \text{ km s}^{-1}$ absorption feature toward the E nucleus are partly in redshifted velocities, e.g., in the CN spectra in Fig. 19. A redshifted wing of absorption profile can also be inferred by decomposing some line profiles (e.g., CO, HCN) into a Gaussian emission and a Gaussian absorption.

Similar to our observations toward Arp 220W, there might be an additional narrow absorption feature in the CO line profiles at a slightly more redshifted velocity than the broader component and the systemic velocity of the nucleus. It may be why the nominal minimum in the trough of the CO(1–0) profile is slightly redshifted compared to the systemic velocity of the nucleus.

Therefore, the eastern nucleus has an absorption line system of at least one and maybe two components. This system is similar in many ways to that toward the W nucleus. A notable difference is the lack of deep sub-continuum absorption in SiO and H_2CO toward the E nucleus.

Two outflows:—Both nuclei have a broad absorption feature that is blueshifted relative to the nucleus; $V_{\min}(\text{W}) \sim 5230 \text{ km s}^{-1} \sim V_{\text{sys}}(\text{W}) - 70 \text{ km s}^{-1}$ and $V_{\min}(\text{E}) \sim 5350 \text{ km s}^{-1} \sim V_{\text{sys}}(\text{E}) - 50 \text{ km s}^{-1}$. These blueshifted absorptions have been attributed to molecular outflows from the individual nuclei (Sakamoto et al. 2009). Our ALMA observations support this interpretation in three ways. First, the absorbing gas must have different line-of-sight velocities (V_{abs}) toward the two nuclei after correcting their apparent V_{\min} . It is because for $V_{\min} < V_{\text{sys}}$ the corrected V_{abs} will be at $V_{\min} < V_{\text{abs}} < V_{\text{sys}}$, and hence one obtains $V_{\min}(\text{W}) < V_{\text{abs}}(\text{W}) < V_{\text{sys}}(\text{W}) < V_{\min}(\text{E}) < V_{\text{abs}}(\text{E}) < V_{\text{sys}}(\text{E})$ for Arp 220. Second, the two broad-line absorbers have distinctively different degrees of absorption between the two sightlines in CS(7–6), SiO(8–7), and o- H_2CO transitions. Third, the absorbing gas must be close to each nucleus rather than in a common envelope of the two nuclei. For these broad absorptions to occur, the absorbing gas must have a high enough excitation yielding a significant population of the lower levels of the observed absorption features, such as $J=3$ for $\text{HCN}(4-3)$ absorption. We saw that such high excitation was limited to the immediate vicinity of each nucleus for species other than ^{12}CO (Section 4.2.1). For these reasons, we

maintain that these blueshifted, broad-line absorption features are due to two molecular outflows, one from each nucleus.

Narrow absorption:—The narrow-line absorption feature toward Arp 220W, as well as the possible one toward Arp 220E, may well be due to gas that is farther out from each nucleus than the broad-line absorbers. Their small velocity widths (i.e., less turbulence) and lower excitation implied by their detection mostly in CO are consistent with this interpretation. The gas causing the narrow line absorption can be either in the outskirts of the individual nuclear disks or outside the nuclear disks and in a large gas structure in the merger, such as the outer disk to encompass the two nuclei. In either case, the small offset of the narrow features from V_{sys} of each nucleus may only represent disturbed gas motion (e.g., in the outskirts of the nuclear disks) and not necessarily a coherent motion of gas on large scales.

4.4.3. Outflow-Disk Configurations through Spatially Lopsided Line-absorption

If a disk is the continuum source and the absorbing gas is due to a bipolar outflow, then the spatial distribution of the line absorption tells us about the outflow-disk configuration. In the top row of Figure 20, a bipolar outflow of molecular gas is perpendicular to a continuum-emitting nuclear disk. The outflow should cause line absorption preferentially around the far-side semi-minor axis of the disk in blueshifted velocities. The outflow may also be visible in emission further from the center around the minor axis, either on the near-side of the disk in redshifted velocities or on the far-side in blueshifted velocities. Thus, it is possible to use a spatially-lopsided system of absorption and emission around the center to detect a bipolar outflow normal to a bright and opaque nuclear disk. This method is parallel to detecting an outflow through a P-Cygni line profile, i.e., an anti-symmetric system of absorption and emission in the velocity space. Figure 20 also shows in the bottom row that a slanted bipolar outflow that is not perpendicular to the nuclear disk can have lopsided and redshifted absorption. The absorption occurs on the far side of the disk but not necessarily on the minor axis of the disk. From a spatially-lopsided intensity profile and the velocity information of the line absorption, one can tell the direction of the bipolar outflow and near and far sides

of the inclined disk and constrain whether the outflow is normal to the disk.⁵

NGC 4418:—This nucleus has redshifted absorption in many lines (Section 4.4.1). Figure 21(a) shows intensity profiles of three lines along the east–west axis across the continuum peak. The profiles are from the channel maps at $V_{\text{sys}} + 50 \text{ km s}^{-1}$, where the redshifted absorption is most significant. The profiles show that redshifted absorption is slightly shifted to the west (p.a. = -90°) relative to the continuum peak. (We adopted the E–W slicing based on the offset seen in the $\text{HCO}^+(4-3)$ channel map.) If this offset is due to an outflow, then the far-side of the nuclear disk, whose major axis is at p.a. $\approx 47^\circ$, is in the northwest, which is also the far-side of the large-scale galactic disk (and hence the two disks are nearly coplanar). In this outflow model, the redshifted velocity of the absorption means that the outflow direction is oblique to the nuclear disk, similar to the lower row in Fig. 20. Such slanted configurations are often found in AGN-driven outflows, e.g., in NGC 1068 (García-Burillo et al. 2014). The slanted outflow is not immediately visible in emission, except that the $\text{HCN}(4-3)$ mean velocity map in Fig. 14 shows a blueshifted component about $0''.2$ east of the nucleus. We present this slanted mini outflow as a possible model for the redshifted absorption in NGC 4418. This model still needs verification because the spatial offset of the absorption is small (since the continuum nucleus is compact) and because the lopsidedness in Fig. 21(a) may be due to line emission in the nuclear disk. Another model for the redshifted absorption is the inward-moving gas along our sightline, explained in Section 4.4.1. We add that the $\text{SiO}(16-15)$ absorption at the systemic velocity is at the continuum peak position without an offset. A possible reason for the lack of lopsided absorption and circumnuclear emission is that the SiO excitation to $J \sim 15$ owes much to sub/millimeter continuum radiation from the nucleus (see Section 4.4.4).

Arp 220W:—The blueshifted absorption toward Arp 220W was first found spatially lopsided by Tunnard et al. (2015), who linked it to a lopsided occultation of the nuclear disk by the outflow. The absorption offset has been confirmed in subsequent observations (Rangwala et al. 2015; Martín et al. 2016; Wheeler et al. 2020), and it is also in earlier SMA observations (Sakamoto et al. 2008, 2009) as a small offset between the peak of

⁵ We consider a collimated *inflow* toward a nuclear disk much less likely and disregard it without new evidence, although it could also explain the spatially-lopsided absorption in blue- and redshifted velocities.

continuum emission and that of CO integrated intensity. This lopsidedness is very clear in many of our channel maps. Specifically, the line emission around the continuum peak of the nucleus is stronger to the north and weaker to the south in velocities around 5300 km s^{-1} ; see HNC(4–3), $\text{HCO}^+(4-3)$ and (3–2), HCN(4–3) and (3–2), $\text{C}_2\text{H}(4-3)$, SiO(8–7), and CS(7–6) in Figs. 9 and 10. Notable exceptions, SiO(16–15) and $\text{H}_2\text{CO}(9_{1,8}-8_{1,7})$ in Band 9, are addressed in Section 4.4.4. Figure 21(b) shows the lopsidedness in HCN(4–3) using the intensity profiles along the outflow axis of p.a. = -15° that is within 10° from the minor axis of the nuclear disk (Paper I). The lopsided absorption is evident, with the absorption slightly shifted to the south of the continuum nucleus. We attribute this spatial lopsidedness to the absorption of the photons from the background nuclear disk. Then, the absorbing gas must cover more of the southern side of the western nuclear disk. Therefore, the southern side of the nuclear disk must be the far side of the disk, whether the outflow is normal to the nuclear disk or not.

The direction of the outflow can be determined from gas velocities. In Arp 220W, blueshift is evident in the broad absorption (Section 4.4.2). Moreover, the blueshifted absorption is slightly shifted to the south from the centroid of the continuum nucleus in Fig. 21(b); i.e., the spatial lopsidedness is clearer in blueshifted velocities. Furthermore, blueshifted gas is seen in emission south of the nuclear disk in the channel maps at velocities $\lesssim 5000 \text{ km s}^{-1}$. There is also redshifted emission elongated to the north of the nucleus at $V \gtrsim 5600 \text{ km s}^{-1}$ (Section 4.3.2 and Fig. 17). Therefore, the outflow is bipolar. Its southern side is approaching us, and the northern side is receding from us. Figure 22 illustrates this outflow configuration.

The configuration of the nuclear disk and the orientation of the bipolar outflow determined above are consistent with the outflow axis agreeing (to a few 10 degrees in the three-dimensional space) with the rotational axis of the nuclear disk. While it is also possible that the two axes overlap only in their sky-plane projection, our observations disfavor some large angles between them, e.g., the outflow to the far-side of the nuclear disk cannot be receding. There remains a puzzle (Tunnard et al. 2015; Sakamoto et al. 2017) that the configuration of the nuclear disk (i.e., the southern side being the far side) is opposite to what was suggested by the near-IR light distribution (Scoville et al. 1998). A likely key to this puzzle is that the nuclear disk may well be warped, flared, or non-axisymmetric given the tidal interaction with the eastern nucleus and the high luminosity activities inside.

The overall outflow-nuclear disk configuration of Arp 220W is summarized in Figure 22. The major axis of the western nuclear disk was measured to be at p.a. $\approx 83^\circ$ in our fitting of 3 and 0.4 mm continuum emission and the distribution of supernovae (Paper I). It is consistent with the well-known east-west velocity gradient in molecular lines, seen abundantly in our data. The bipolar outflow at p.a. $\approx -15^\circ$, seen in both continuum and line emission, is almost along the minor axis of the nuclear disk. The continuum analysis in Paper I also found the minor-to-major axis ratio of 0.47 for the western nuclear disk. Thus the disk inclination must be $\gtrsim 60^\circ$; that is, $\sim 60^\circ$ for a thin disk and edge-on for an oblate spheroid whose diameter is twice its full height. The presence of spatially-lopsided line absorption disfavors a completely edge-on configuration. The blue- and red-shifted lobes of line emission from the bipolar outflow also disfavor the edge-on nuclear disk if the outflow is perpendicular to it.

Arp 220E:—We found the blueshifted absorption toward the eastern nucleus to be spatially lopsided too. The absorption is slightly shifted from the continuum peak in the channel maps of HCN and HCO^+ lines in both the (4–3) and (3–2) transitions. At and below the fiducial systemic velocity of this nucleus, 5400 km s^{-1} , the lines show absorption northwest of the continuum peak and emission in the southwest. Figure 21(c) shows this shift using HCN(4–3) intensity profiles along the minor axis of the nuclear disk, whose major axis was measured to be at p.a. $\approx 51^\circ$ in our 3 and 0.4 mm continuum analysis and the distribution of supernovae (Paper I).

The anti-symmetric intensity pattern around the continuum nucleus suggests that an out-of-plane gas is in front of the eastern nuclear disk to the northwest of its center. The bulk of this foreground gas must be moving toward us since the anti-symmetric pattern is clearer in blueshifted velocities. This configuration is consistent with a polar outflow from the eastern nuclear disk, whose northwest side is the far side. We can, however, less stringently constrain the angle between the outflow and the nuclear disk than for the W nucleus. By analogy with many galactic outflows, we assume the outflow to be bipolar, having an undetected redshifted lobe in the southeast direction.

Figure 22 contains our current best estimate of the disk and outflow configuration in the E nucleus. Our data suggest that the disk is inclined by around 70° and that the E outflow is smaller than the W outflow. The minor-to-major axial ratio of the eastern nuclear disk is 0.45 in the continuum analysis in Paper I, suggesting the disk inclination to be $\gtrsim 63^\circ$. A nearly edge-on configuration is disfavored from the presence of the lopsided

absorption unless the outflow axis forms a large angle with the axis of disk rotation. Under the simplest assumptions that both E and W nuclear disks are oblate spheroids and have similar axial ratios (or disks having similar thickness-to-radius ratios), they should have similar inclinations. If we further assume that both outflows are in the polar direction of the nuclear disks, then the outflow from the eastern nucleus should be of a smaller scale (e.g., in mass, velocity, and extent) than the outflow from the western nucleus. It is because, unlike the W nucleus, the E nucleus does not show symmetric line emission along the minor axis at large blue- and redshift velocities. This scale difference can be because the E outflow is slower, has a smaller extent, or is closer to pole-on than the W outflow. The non-detection of this E outflow in continuum emission at 3 mm (Sakamoto et al. 2017) and 0.4 mm (Paper I) also implies it to have less emissivity (e.g., less massive) or a smaller extent on the sky.

The configuration we estimated above for the outflow from Arp 220E does not match some previous studies. Varenus et al. (2016) found in the 150 MHz continuum that Arp 220E shows a north-south elongation possibly due to a plasma outflow. This position angle does not agree with that of the spatially-lopsided line absorption. Wheeler et al. (2020) claimed CO(3–2) detection of the Arp 220E outflow in a different disk configuration. Our comment on it is in Section 5.1.

Counter-rotating nuclear disks:—Finally, we note that the two nuclear disks of Arp 220 in their updated configuration (see Fig. 22) are still counter-rotating with each other as proposed in Sakamoto et al. (1999). This counter-rotation is despite the revision of the near and far sides of the western nuclear disk to the ones opposite from those previously adopted from Scoville et al. (1998), who used the pattern of near-IR extinction to decide the disk orientation. Using the coordinate system where the x -axis is to the east, the y -axis is to the north, and the z -axis is along our sightline directed from us to the target, the direction vector of the angular momentum of a rotating disk is

$$\mathbf{n} = \begin{pmatrix} \cos \theta \sin i \\ -\sin \theta \sin i \\ \cos i \end{pmatrix}, \quad (2)$$

where i is the disk inclination that is the angle between the angular momentum vector and the positive direction of the z -axis and θ is the position angle of the receding major axis of the disk measured from the north to east on the sky plane. Using $\theta_E = 51^\circ$ and $\theta_W = 263^\circ$ from Paper I and assuming $i_E = i_W = 70^\circ$, the angle between

the two rotation vectors is $\cos^{-1}(\mathbf{n}_E \cdot \mathbf{n}_W) = 129^\circ$. (This angle is 150° for $i_W = 110^\circ$, i.e., the previous choice of near and far sides of the western nuclear disk.) An angle larger than 90° , i.e., $\mathbf{n}_E \cdot \mathbf{n}_W < 0$, means counter-rotation. Using conservative errors of $\pm 5^\circ$ for θ_E and θ_W and $\pm 10^\circ$ for i_E and i_W , we obtained $128^\circ \pm 11^\circ$ from 10^3 simulations. Therefore, the counter-rotation of the two nuclear disks in Arp 220 is a robust conclusion.

It is worth noting that the western nuclear disk also counter-rotates with the kpc-scale gas structure around the two nuclei of Arp 220, referred to as the outer disk in Sakamoto et al. (2009). The gas in the western nuclear disk can efficiently lose angular momentum by interacting with the outer disk. Interestingly, the nuclear disk of NGC 4418 also counter-rotates with the gas and stars in the surrounding environment, i.e., the kpc-scale galactic disk. It is plausible that the counter-rotation of the nuclear disks of Arp 220W and NGC 4418 relative to their surroundings helped the two nuclei to have extreme central gas concentrations of $N_H \sim 10^{26} \text{ cm}^{-2}$ and their luminous nuclear activities.

4.4.4. Other Absorption-related Issues

SiO:—We have seen a striking variation of SiO in its absorption and emission among transitions and the three nuclei (see Figs. 3, 2, 8, and 9). SiO(8–7) is detected in absorption toward all three nuclei; the absorption is deepest in Arp 220W, next in NGC 4418, and least in Arp 220E. The contrast between the two nuclei of Arp 220 is consistent with previous SiO observations (Tunnard et al. 2015; Rangwala et al. 2015; Wheeler et al. 2020). SiO(8–7) is also detected in emission around the compact absorption in the three nuclei. In contrast, SiO(16–15) is detected only toward NGC 4418 and Arp 220W and only (or mostly) in absorption. The emission in redshifted velocities in the SiO(16–15) channel maps of NGC 4418 (Fig. 5b) is probably $\text{H}^{13}\text{CO}^+(8-7)$, judging from the line frequency. Similarly, the faint circumnuclear emission in the SiO(16–15) channel maps of Arp 220 is probably the same line blending because it is only in redshifted velocities. The SiO(16–15) absorption is compact and, unlike the SiO(8–7) absorption, has its centroid on the continuum peak in both NGC 4418 and Arp 220W.

Tunnard et al. (2015) deduced that the two nuclei of Arp 220 are chemically distinct from a striking difference in SiO(6–5) absorption. On the other hand, the overall pattern of emission seen in the remaining majority of lines in our spectra does not appear drastically different between the two nuclei. Therefore, it may be that the drastic difference in SiO may be partly due to this particular species. For example, the more promi-

ment molecular outflow in Arp 220W may have caused the difference (Tunnard et al. 2015; Wheeler et al. 2020) because the SiO abundance can be enhanced by shocks in an outflow (Martin-Pintado et al. 1992). The same explanation may apply to the difference of Arp 220W and NGC 4418 in their SiO(8–7) absorption.

Another possible reason for the variation of SiO absorption is the different degrees of luminosity concentration and SiO excitation by radiation. Arp 220W and NGC 4418 are comparably bright, and the two are brighter than Arp 220E, in the 200–700 GHz continuum (Paper I). In addition, the former two are more highly obscured than the latter (Paper I). These differences will result in different SiO excitation by both IR radiation (through vibrational SiO excitation) and submillimeter radiation. The larger column densities of Arp 220W and NGC 4418, on the order of $N_{\text{H}} \sim 10^{26} \text{ cm}^{-2}$ (Paper I), are more favorable for vibrational SiO excitation by $8.1 \mu\text{m}$ IR radiation. It is because the trapping of continuum photons works more to increase the inner temperature of the nuclei through the greenhouse effect (González-Alfonso & Sakamoto 2019). The possibility of IR pumping of SiO was raised for Arp 220W by Rangwala et al. (2015). Unfortunately, we did not detect lines from vibrationally excited SiO, such as SiO($v = 1, J = 8-7$) at 344.916 GHz in our frequency coverages of both Arp 220 and NGC 4418, but a weak feature could be lost in blending (e.g., with adjacent H^{13}CN). At least in HC_3N , vibrational excitation appears more significant in Arp 220W than in Arp 220E (Section 4.5.1).

The radiative SiO excitation through the sub/millimeter continuum explains the variation of SiO absorption among the three nuclei and the localized SiO excitation to $J \sim 15$ in each nucleus. That we detected SiO(16–15) only in absorption and toward NGC 4418 and Arp 220W implies that SiO excitation to the $J=15$ (16) level, at 250 (283) K above the ground, is limited to the hottest or brightest nuclei. Both nuclei have peak continuum brightness temperatures of ~ 500 K, while Arp 220E has $\lesssim 200$ K at 200–700 GHz (Paper I). It is consistent with the SiO(16–15) absorption detected only toward Arp 220W and NGC 4418. If this radiative excitation dominates the SiO excitation to $J \sim 15$, it would be the reason why the SiO(16–15) absorption coincides with the continuum peaks (Section 4.4.3).

Isotopologues:—There are absorption features of rarer isotopologues toward Arp 220W. Among them are $\text{H}^{13}\text{CO}^+(4-3)$, $\text{H}^{13}\text{CN}(4-3)$, and $^{13}\text{CS}(15-14)$ in this work (Figs. 3, 19), $\text{C}^{34}\text{S}(2-1)$ in Sakamoto et al. (2017), and $^{13}\text{CO}(4-3)$ absorption in Wheeler et al. (2020). While the absorption line of $\text{H}^{13}\text{CO}^+(4-3)$ is in Fig. 19(c) at around 5530 km s^{-1} in the SiO(8–7)

spectrum, we identify this feature to a blueshifted absorption of $\text{H}^{13}\text{CO}^+(4-3)$ rather than a redshifted absorption of SiO(8–7). The minimum of this feature is then at about 50 km s^{-1} blueshifted from the systemic velocity of the nucleus. The blueshift is consistent with that of the deepest absorption of other lines, including HCO^+ , H^{13}CN , and SiO. Both Arp 220E and NGC 4418 also show signs of weak $\text{H}^{13}\text{CN}(4-3)$ absorption in Fig. 24(a) and (d). The absorption of these rarer isotopologues reflects the large gas column density toward these nuclei. It is because they are less prone to self-absorption than the primary isotopologues and also because the dust in the background needs to be opaque enough to emit bright from behind these molecules.

4.5. Vibrationally Excited Lines

Rotational lines from vibrationally excited molecules have been explored as promising probes of deeply buried galactic nuclei since their first extragalactic detection for HC_3N (Costagliola & Aalto 2010) and HCN (Sakamoto et al. 2010). For short, we refer to these as HCN-vib, HC_3N -vib, and vib-lines. Our new data added the following to the information on vib-lines and their usage.

4.5.1. Individual Species

HC_3N :—Our $0''2$ data in Fig. 3 have rotational lines of HC_3N in both vibrationally ground and excited states. Their $J=40-39$ transitions are at $f_{\text{rest}} \sim 364-365 \text{ GHz}$. We note that the $\text{HC}_3\text{N } v_7=1$ doublet, which is resolved in NGC 4418 but blended in the Arp 220 nuclei, is brighter than the $\text{HC}_3\text{N } v=0$ line toward all three nuclei. The former $v=0$ line has upper-state energy of 358 K while the latter $v_7=1$ lines have $E_u = 680 \text{ K}$. They have the same statistical weights in their upper levels and virtually the same Einstein A coefficients. If their vibrational and rotational excitation temperatures are the same in the LTE condition in a uniform gas cloud, the $v=0$ line should be stronger than or as strong as the $v_7=1$ lines. Therefore, the observed line ratio suggests the gas in these nuclei to be non-uniform or not in LTE or both. A plausible situation is a radial temperature gradient with a higher temperature inside. The ratio of the mean integrated intensity of the $v_7=1$ doublet to that of the $v=0$ line is higher in Arp 220W than in Arp 220E and NGC 4418. Specifically, the ratio for $J=40-39$ is 2.42 ± 0.04 , 1.50 ± 0.04 , and 1.14 ± 0.01 , respectively for Arp 220W, Arp 220E, and NGC 4418 in the $0''2$ scale, where the integration of each line is over a velocity width of 500 km s^{-1} for the Arp 220 nuclei and 300 km s^{-1} for NGC 4418. The ratios imply that Arp 220W has the steepest temperature gradient or infrared radiation, or both.

HCO⁺: —Detection of HCO⁺-vib is possible but not yet certain toward the three nuclei. The NGC 4418 spectra in Figs. 3 and 4 have peaks at the frequencies of HCO⁺($v_2=1$, $J=4-3$, $l=1e$) and HCO⁺($v_2=1$, $J=3-2$, $l=1e$). However, much of these features must be artifacts caused by the blueshifted absorption of the adjacent HCO⁺(4–3) and (3–2) lines. Indeed, our spectrum does not have isolated peaks at the frequencies of the other transitions of the $v_2=1$ doublets ($l=1f$). The intensities there are 2–5 times lower than at the $l=1e$ transitions. Our initial LTE modeling of the spectrum in Fig. 23 gives an idea of the possible contribution of the vibrationally-excited HCO⁺ lines to the observed spectrum. Better line de-blending and emission+absorption modeling are necessary for firmly constraining the line strengths. In the nuclei of Arp 220, the line blending is much worse than in NGC 4418. Although the spectra show peaks at the HCO⁺($v_2=1$, $l=1e$) frequencies, intensities are again much lower at the frequencies of HCO⁺($v_2=1$, $l=1f$) transitions.

HNC: —Costagliola et al. (2013) detected HNC($v_2=1$, $J=3-2$, $l=1f$) toward the nucleus of NGC 4418, but we only have the HNC($v_2=1$, $J=4-3$) doublet in our spectral coverage. We did not firmly detect the HNC($v_2=1$, $J=4-3$, $l=1f$) line because it is heavily blended with another line. Unfortunately, HNC($v_2=1$, $J-J-1$, $l=1f$) lines always have HC₃N($v_7=1$, $10J-10J-1$, $l=1f$) nearby because their rotational constants have a ratio close to an integer, 10.⁶ With their separations of 39, 82, and 113 km s^{−1} for $J=4$, 3, and 2, respectively, they tend to blend in extragalactic observations and most severely so for $J=4$ among those easily accessible transitions. In our NGC 4418 spectrum in Figure 3, the HC₃N($v_7=1$, $J=4-3$) doublet lines, $l=1e$ and $1f$, have about the same peak intensities as they should (because they have the same statistical weights and virtually the same Einstein A coefficients.) The $l=1f$ peak is only slightly higher. While this slight excess could be due to the HNC($v_2=1$, $J=4-3$, $l=1f$) line, a firm conclusion waits for de-blending of lines to exclude the possible contribution from any other low-level lines. In the Arp 220 nuclei, the same vibrationally-excited HNC line (if any) is too heavily blended with the HC₃N($v_7=1$, $l=1f$) line for detection. The other half of the HNC($v_2=1$) doublet, $l=1e$ lines, should be only 63 km s^{−1} offset from the vibrationally-ground HNC lines.

⁶ The rotational constant is 45.484 GHz for HNC($v_2=1$, $l=1f$) (Thorwirth et al. 2000) and 4.5635 GHz for HC₃N($v_7=1$, $l=1f$) (Bizzocchi et al. 2017).

Therefore, both of the HNC($v_2=1$) doublet lines are not immediately visible in our data.

Comparison with HCN: —In the three galactic nuclei, rotational lines from vibrationally excited states are comparably strong in HCN and HC₃N and much weaker in HCO⁺ and HNC. Indeed, the HCN-to-HCO⁺ ratio in their $v_2=1$ lines is 3.5 in both $J=4-3$ and $3-2$ in our spectral fit for NGC 4418. In our Galaxy, hot molecular cores heated by young massive stars inside also show rotational lines from vibrationally excited HCN but not HCO⁺; it has been attributed to abundance enhancement of HCN (but not HCO⁺) in the high-temperature environment (Rolfs et al. 2011). HCN enhancement in such an environment is also expected in the context of galactic nuclei (Harada et al. 2010). An elevated abundance of HCN has been suggested, from its 14 μ m absorption line, in deeply obscured nuclei of infrared galaxies (Lahuis et al. 2007; González-Alfonso et al. 2012).

4.5.2. Vib-lines as a Group

We saw in Section 4.2 that the line-emitting regions tend to be smaller for vibrationally-excited lines than for vibrationally-ground lines. We also found in NGC 4418 that the line-emitting areas are smaller for transitions having higher upper-state energies even within each vibrational state. The emitting regions of the vib-lines are found comparable in size and shape with continuum emission. This similarity is reasonable considering that the vib-lines are most likely due to radiative excitation by mid-IR continuum photons from warm dust. These observations have the following implications. One of them is that the vib-lines are suited for selectively studying the inner regions of the warm buried nuclei, as was proposed in our detection report of HCN-vib lines in NGC 4418 (Sakamoto et al. 2010). Another is that VIB lines tend to be more beam-diluted than lines in the vibrational ground state when observed with a large beam. Another is that beam dilution is larger for vib-lines than for the vibrationally ground lines in an observing beam larger than both line-emitting regions. Therefore, the ratio of vibrationally-excited-to-vibrationally-ground lines is biased (underestimated) in observations at a low angular resolution. This bias lowers the vibrational excitation temperature T_{vib} estimated from the observed ratio unless correcting for the different beam-filling factors. This difficulty also applies to the vibrational excitation analysis of multiple vibrationally-excited lines at different vibrational levels, such as the one using v_6 , v_7 , and v_4 states in HC₃N.

While the beam-filling factors can be matched with a high enough spatial resolution to resolve the emitting areas of the vibrationally-excited lines, there is another

difficulty in the line-ratio analysis with such observations. The vibrational-ground lines are often in absorption when the vibrationally-excited lines are in emission. Their line ratios would be then negative numbers, and hence their logarithms do not give vibrational-excitation temperatures. For a vibrational excitation temperature, one needs formal radiative-transfer modeling (e.g., González-Alfonso & Sakamoto 2019) or ratio(s) between emission lines from different vibrationally excited states. An example of the latter could use lines from the v_6 and v_7 states of HC_3N if both are optically thin. On the other hand, if the vib-lines are optically thick, their observed brightness temperatures can set a lower limit to both the rotational and vibrational excitation temperatures.

Another implication of the absorption of rotational lines within the vibrationally-ground state is that this absorption tends to mask the effect of IR radiative pumping to the rotational excitation within the vibrational ground state for the inner nucleus. This masked area is where the IR pumping should have the maximum effect on the rotational level population. The absorption of the $v = 0$ lines there means that this effect should appear reduced in low-resolution data integrating the entire nucleus. This effect, IR radiative pumping, has been a concern in the usage of HCN as a tracer of dense gas in luminous galactic nuclei under the assumption of HCN excitation through collision with H_2 (Aalto et al. 1995; Graciá-Carpio et al. 2006). The virtual masking of the innermost region reduces the error due to the omission of IR radiative excitation. Without correcting for the masking effect, the results of such excitation analysis will reflect the properties of the circumnuclear region rather than the innermost regions.

5. FOLLOW-UP ON PREVIOUS REPORTS

Our wide-band, high-resolution, and sensitive ALMA data allow us to verify some of the earlier observations.

5.1. Arp 220E — Outflow Emission in CO(3–2)?

Wheeler et al. (2020) suggested a collimated outflow from Arp 220E on the basis of emission features at $V - V_{\text{sys}} \approx \pm 500 \text{ km s}^{-1}$ in their CO(3–2) data. The same features are also in our data (Fig. 24a). However, their model has the opposite orientations of ours for the outflow and the eastern nuclear disk. While we both adopt a bipolar outflow normal to the nuclear disk, their model has the outflow redshifted (receding) to the northwest and the near side of the eastern nuclear disk also to the northwest. Both are the opposite of our model in Fig. 22. Their disk and outflow configuration would produce continuum absorption to the southeast of the nucleus while we detected it to the northwest.

This discrepancy must be because much of the putative outflow emission is not CO(3–2) at high velocities but blended lines. The first sign of this misidentification is that these features have peaks at around $\pm 500 \text{ km s}^{-1}$ of CO(3–2) rather than smoothly declining at a larger offset from the CO line center. The second, stronger indication is the absence of the $\pm 500 \text{ km s}^{-1}$ features in CO(2–1) and (6–5), as shown in Fig. 24b. Thirdly, the blended lines have identifications, $\text{H}^{13}\text{CN}(4-3)$ on the redshifted side and three $J=38-37$ transitions of vibrationally excited HC_3N on the blueshifted side. We will explain how these lines form the $\pm 500 \text{ km s}^{-1}$ features in the CO(3–2) spectrum. Lastly, the $\pm 500 \text{ km s}^{-1}$ features are also in the spectrum of the western nucleus, as expected in the case of blended lines (Fig. 24a and c). These constitute strong evidence that the $\pm 500 \text{ km s}^{-1}$ features in the CO(3–2) spectrum toward Arp 220E are due to line blending rather than high-velocity CO emission.

The $\text{H}^{13}\text{CN}(4-3)$ transition is on the redshifted side of CO(3–2) at $+390 \text{ km s}^{-1}$ in the CO velocity. The known blueshifted absorption toward each nucleus makes the actual $\text{H}^{13}\text{CN}(4-3)$ line asymmetric and shifts its emission peak to a higher velocity in the CO(3–2) velocity. As a reference, HCN(4–3) toward the E nucleus has its peak about 150 km s^{-1} redshifted from the systemic velocity. Therefore, it is reasonable that $\text{H}^{13}\text{CN}(4-3)$ has an intensity peak at $v \approx +550 \text{ km s}^{-1}$ in the CO(3–2) spectrum toward the W nucleus. The $\text{H}^{13}\text{CN}(4-3)$ identification toward the W nucleus is also based on its circumnuclear distribution and convincing (Section 4.1). The line intensity on the E nucleus at the expected $\text{H}^{13}\text{CN}(4-3)$ peak frequency is consistent with the $\text{H}^{13}\text{CN}(4-3)$ intensity on W and the E-to-W ratio of other emissions (i.e., a factor 2–3 weaker toward E than toward W as in $\text{C}^{18}\text{O}(2-1)$ and 1.3–0.85 mm continuum), supporting our $\text{H}^{13}\text{CN}(4-3)$ identification. We add that $\text{HC}_3\text{N}(38-37)$, a transition within the vibrational ground state, must also be blended with CO(3–2) at $+160 \text{ km s}^{-1}$ though hardly discernible in our Arp 220 data.

On the blueshifted side of CO(3–2) around -500 km s^{-1} are three $J=38-37$ transitions of vibrationally excited HC_3N , namely $\text{HC}_3\text{N}(v_7=1, l=1e)$, $\text{HC}_3\text{N}(v_6=1, l=1f)$, and $\text{HC}_3\text{N}(v_6=1, l=1e)$. The $v_7=1$ line should be brighter because the upper states for $v_7=1$ and $v_6=1$ are 646 K and 1042 K above the ground, respectively. The three lines should be, respectively, at about -562 , -554 , and -322 km s^{-1} in the CO(3–2) spectrum. They are detected in NGC 4418 as two peaks with the first two transitions merged and being brighter than the third one (Fig. 24d). In Arp 220 toward both nuclei, all three lines

are blended and detected as a single peak at $f_{\text{rest}} \approx 355.4$ GHz for J=39–38 and 264.4 GHz for J=29–28 in Figs. 3 and 4. From their information, the blended feature for J=38–37 is expected to be at $v \approx -500$ km s $^{-1}$ in the CO(3–2) spectrum, having a ~ 3 K excess at 0''.2. It is consistent with our observations and, therefore, explains the -500 km s $^{-1}$ feature.

As we have seen, line-blending complicates the outflow search through broad line wings unless the wing emission overwhelms adjacent lines. Therefore, it is sensible to verify possible molecular outflow features using multiple lines, the spatial distribution of the emission, line de-blending, and careful baseline subtraction. The outflow from the western nucleus passed these tests, even though its ± 500 km s $^{-1}$ features in CO(3–2) in the central few tenths of arcsec must be mostly due to blended lines (Fig. 24c). In contrast, the molecular outflow from Arp 220E has been seen only through absorption lines and not yet in emission. In all likelihood, this outflow also has emissions in CO and other lines, and their imaging would constrain the outflow parameters more.

5.2. HNC maser

Aalto et al. (2009) reported SMA observations of a bright (39 K at 0''.4 resolution), narrow (60 km s $^{-1}$) emission feature of HNC(3–2) from the western nucleus of Arp 220. This spike feature is on top of a broader spectral component, which may be from the rotating western nuclear disk. The spike is at $V(\text{radio, LSR}) = 5358$ km s $^{-1}$ near the center of the broad component and has about three times higher peak intensity than the broad component. It was argued that the narrow feature might be a weak, possibly transient maser emission. We observed HNC(4–3) at twice higher angular and spectral resolutions and more than ten times higher sensitivity in brightness temperature. Figure 3 (red line for Arp 220W) contains HNC(4–3) at $f_{\text{rest}} = 362.6$ GHz in the spectra sampled with 0''.20 and 0''.35 beams. Neither spectra show the narrow emission spike reported in HNC(3–2). Instead, they show a broader peak with peak brightness temperatures of about 47 and 30 K respectively at 0''.20 and 0''.35, as well as the blueshifted absorption feature (or intensity decrement) that we attributed to an outflow. The bright emission spike is not seen either in the 0''.65 resolution HNC(3–2) spectrum from our companion spectral scan in Figure 25 and the 0''.75 resolution spectrum of HNC(2–1) in König et al. (2017). The HNC(3–2) line profiles are similar to our HNC(4–3) profiles, showing signs of blueshifted decrement toward both nuclei. They also have narrow dips near the systemic velocities of the individual nuclei; the one toward Arp 220W has $V_{\text{min}} \approx 5340$ km s $^{-1}$. They are

similar to the narrow CO absorption that we described in Section 4.4.2. Since the spike emission of HNC(3–2) is not confirmed in ALMA data, the putative maser feature must be either transient or an artifact. Our three galactic nuclei do not show spike-like emission features in any line in our dataset.

5.3. H₃O⁺ detection

Van der Tak et al. (2008) reported detection of the H₃O⁺(3₂⁺–2₂[–]) line ($f_{\text{rest}} = 364.797$ GHz) in emission toward Arp 220 using the James Clark Maxwell Telescope (JCMT). They deduced from the line velocity that the line, tracing ionization of hot ($\gtrsim 100$ K) gas, was from the western nucleus. However, this association needs caution because the two nuclei of Arp 220 have line widths of ~ 500 km s $^{-1}$ in FWHM and are only 100 km s $^{-1}$ different in their systemic velocities (see Fig. 1). The lines from the two nuclei should overlap for the most part in the single-dish spectrum. In addition, the reported line velocity of $V(\text{helio, radio}) = 5473 \pm 8$ km s $^{-1}$ corresponds to $V(\text{LSR, radio}) = 5488 \pm 8$ km s $^{-1}$ and is closer to the velocity of the eastern nucleus.

Our observations covered the frequency of the H₃O⁺ line, as shown in Figure 3. The Arp 220 data reveal a broad, ~ 1 GHz-wide, emission feature around the frequency of the H₃O⁺ transition. It is seen toward both nuclei in a similar shape, with its peak being a few tenths of GHz offset from the H₃O⁺ frequency. We did not confirm the 113 km s $^{-1}$ (0.14 GHz)-wide line at the H₃O⁺ frequency in the JCMT observations, whose bandwidth was 1 GHz. Referencing our spectrum of NGC 4418, whose narrower lines suffer less blending, we see bright lines of vibrationally excited HC₃N ($J_{\text{up}}=40$; $v_6=1$ and $v_7=1$ lines) around the H₃O⁺ frequency. One must be careful about possible blending with these HC₃N-vib lines when searching for H₃O⁺(3₂⁺–2₂[–]) in galaxies. In the Arp 220 nuclei, two lower rotational groups of the vibrationally excited HC₃N lines are detected at lower intensities than the $J_{\text{up}}=40$ group. It is plausible that the H₃O⁺(3₂⁺–2₂[–]) line (or any other nearby lines) contributes to the broad feature at $f_{\text{rest}} \sim 365$ GHz. Its confirmation and line fluxes need precise line de-blending.

Our NGC 4418 data also suggest excess emission around the H₃O⁺ frequency. Comparing the channel maps of the HC₃N(J=40–39, $v_7=1$) doublet in Fig. 6(a) and (b), there is excess emission around 2000 km s $^{-1}$ in the HC₃N(J=40–39, $v_7=1$, $l=1e$) maps. The H₃O⁺(3₂⁺–2₂[–]) transition is at 2001 km s $^{-1}$ there. Accordingly, our spectral modeling, a portion of which is in Figure 26, attributes the line feature at ~ 364.7 GHz to a combination of HC₃N(40–39, $v_7=1$, $l=1e$) and H₃O⁺(3₂⁺–2₂[–]), although the current model poorly fits the 364.7 GHz peak

intensity. H_3O^+ has no other transitions in our data to verify this identification. The flux of the presumed H_3O^+ line must be much less than that of $\text{HC}_3\text{N}(40-39, v_7=1, l=1e)$ judging from the comparison with the adjacent $v_7=1, l=1f$ line and the $v_7=1$ doublets in other rotational groups.

5.4. C^{18}O -to- ^{13}CO ratios

There have been reports of anomalously high C^{18}O -to- ^{13}CO line ratios of about unity in Arp 220 (Greve et al. 2009; Matsushita et al. 2009; Martín et al. 2011; Brown & Wilson 2019). Also reported is an enhancement of the $[\text{C}^{18}\text{O}/^{16}\text{O}]$ abundance ratio in Arp 220 by about a factor of 5 compared to the Galactic ones (González-Alfonso et al. 2012). The former is from millimeter-wave emission lines of the isotopologues, while the latter is from far-IR absorption lines of H_2O , OH, and their ^{18}O isotopologues. It has been argued that these unusual ratios in Arp 220 are due to the production of ^{18}O in high-mass stars and their release to the ISM (Matsushita et al. 2009; González-Alfonso et al. 2012; Brown & Wilson 2019). Our 1 mm spectra in Fig. 4 confirm the observations of Martín et al. (2011) that $\text{C}^{18}\text{O}(2-1)$ is slightly stronger than $^{13}\text{CO}(2-1)$ in Arp 220. We now see this in both nuclei. (The two nuclei were unresolved in the $8''$ resolution data of Martín et al. (2011), and their assignment of two peaks in spectra to the two nuclei was not upheld since both nuclei have much larger line widths than the velocity difference between them.) Brown & Wilson (2019) already observed the C^{18}O -to- ^{13}CO ratio in the $J=1-0$ transition to be similar in both nuclei and slightly larger than unity. The $1-0$ lines of these isotopologues are no less blended with adjacent lines (e.g., vibrationally-excited HC_3N ; Sakamoto et al. 2017) than the $2-1$ lines are. However, similar observations in the two transitions (despite their different line-blending) lend credence to the claim that the two nuclei have a similar C^{18}O -to- ^{13}CO line ratio slightly larger than unity in both transitions. The C^{18}O -to- ^{13}CO ratio of integrated intensities for the entire galaxy is 1.3 in $J=2-1$, according to the line flux measurements with deblending of contaminating lines in Martín et al. (2011). The two nuclei should therefore have about the same value.

Regarding NGC 4418, González-Alfonso et al. (2012) found its $[\text{C}^{18}\text{O}/^{16}\text{O}]$ abundance ratio to be ~ 500 (or $\gtrsim 250$), comparable to Galactic values. It is then interesting to see in Fig. 4 that $\text{C}^{18}\text{O}(2-1)$ is less bright than $^{13}\text{CO}(2-1)$ in NGC 4418, unlike in the Arp 220 nuclei. The $\text{C}^{18}\text{O}(2-1)$ -to- $^{13}\text{CO}(2-1)$ ratio is 0.730 ± 0.009 for line intensities integrated over 300 km s^{-1} and 0.507 ± 0.015 for peak intensities. (The uncertainties

do not include those due to any line blending.) The C^{18}O -to- ^{13}CO ratio is less than unity also in $J=1-0$ (Costagliola et al. 2015). It appears that the C^{18}O -to- ^{13}CO line ratio reflects the ^{18}O -to- ^{16}O abundance ratio to some extent and that the beam-averaged line fluxes reflect abundances, despite the likely saturation toward the centers of these nuclei. It remains to be answered why the ^{18}O -to- ^{16}O abundance ratio is different between NGC 4418 and the Arp 220 nuclei despite the number of properties they share. Possible reasons include the difference in star formation history, stellar initial mass function, and relative luminosity contribution between AGN and starburst in the sense that NGC 4418 has a larger AGN contribution.

6. SUMMARY AND CONCLUDING REMARKS

We have presented the line information in our ALMA imaging spectroscopy of three deeply buried nuclei in the infrared-luminous galaxies NGC 4418 and Arp 220. Our scan covers 67 GHz from within $f_{\text{rest}}=215-697$ GHz at $\sim 0''.2$ resolution. The target nuclei are characterized by their very high obscuration ($N_{\text{H}} \gtrsim 10^{25} \text{ cm}^{-2}$), high luminosity ($L_{\text{bol}} \gtrsim 10^{11} L_{\odot}$), and compactness ($\lesssim 100 \text{ pc}$).

1. The three nuclei have forests of lines in their spectra. We reached the line-confusion limit at our sensitivity of $\sigma = 0.1 \text{ K}$ for 50 km s^{-1} in our $0''.35$ spectra from $f_{\text{rest}}=215-367$ GHz (ALMA Bands 6 and 7). Our spectra from $f_{\text{rest}}=670-697$ GHz (Band 9) are about twice less sensitive but still show many lines in both emission and absorption.
2. Toward the center of each nucleus, most of the bright lines are in absorption (i.e., going below the continuum level) or at least show decrement of emission around the systemic velocity. They even include lines of rare isotopologues such as H^{13}CN , H^{13}CO^+ , and ^{13}CS . Lines of vibrationally-excited HCN and HC_3N do not show absorption at the current resolution (although they go into absorption at higher resolution.)
3. Our data show that the size of the emitting region varies among lines. It tends to be smaller for lines with higher upper-level energies (including lines at vibrationally excited states) and lines of rarer isotopologues. This trend suggests a radial gradient of excitation conditions, such as temperature, in each nucleus.
4. As our initial attempt for line identification and modeling, we fitted our $0''.35$ spectrum of NGC 4418 in Bands 6 and 7, assuming isothermal and

uniform gas and LTE. More than 200 lines from 55 species have been identified, although some of them are still tentative.

5. Lines show systematic velocity gradients approximately along the major axis of each continuum nucleus. This gas motion is consistent with the known rotation of nuclear gas disks in Arp 220. We confirmed that the velocity gradient of molecular gas in the center of NGC 4418 is opposite to that of the galactic disk rotation.
6. Many line profiles toward the nucleus of NGC 4418 are asymmetric in various degrees to indicate redshifted absorption. This redshifted absorption, consistent with previous far-IR and submillimeter observations, indicates either an inward gas motion along our sightline or a collimated outflow slanted to the nuclear disk. We found small-scale spatial lopsidedness of the absorption to favor the latter and suggest further verification. We also confirmed in the central 60 pc that lines of dense gas tracers are broader than the CO lines.
7. The molecular outflow from Arp 220W is imaged in several emission lines, most clearly in HCN(4–3) and CO(2–1). It is almost perpendicular to the major axis of the nuclear gas disk, redshifted to the north and blueshifted to the south. The end-to-end extent of the bipolar outflow is about 1'' (400 pc) in our images. Many lines show broad, blueshifted, and spatially-lopsided absorption toward Arp 220W. They are consistent with the collimated outflow.
8. The molecular outflow from Arp 220E is found visible through broad line absorption offset from the continuum peak. The offset of blueshifted absorption to the northwest suggests that the eastern nuclear disk has its far side to the northwest and that the northwestern outflow is approaching us. A recent report of CO(3–2) detection of this outflow has an outflow+disk configuration that is the opposite of ours. The detection must be due to misidentification of H^{13}CN and vibrationally excited HC_3N .
9. The nuclei of Arp 220 also have narrow absorption lines near their systemic velocities, most clearly visible in CO and also in HCN.
10. The two nuclear disks of Arp 220 remain in counter-rotation in the three-dimensional space after reevaluating their major-axis position angles, inclinations, and near-far sides using our

new ALMA data. It is the western nuclear disk that is in counter-rotation with the kpc-scale gas around the binary nucleus. The counter-rotations of Arp 220W and the nucleus of NGC 4418 relative to their surroundings may be partly responsible for their extreme central gas concentrations of $N_{\text{H}} \sim 10^{26} \text{ cm}^{-2}$ and luminous nuclear activities.

11. We verified earlier observations on HNC and H_3O^+ in Arp 220. We did not confirm a bright HNC spike in a previous report. We found that the putative $\text{H}_3\text{O}^+(3_2^+-2_2^-)$ line overlaps with bright lines of vibrationally-excited HC_3N . However, a minor contribution of the H_3O^+ line is still possible in the three nuclei of Arp 220 and NGC 4418.
12. The $\text{C}^{18}\text{O}(2-1)$ to $^{13}\text{CO}(2-1)$ flux ratio is slightly larger than unity in Arp 220 toward both nuclei while it is below unity toward the nucleus of NGC 4418.

Overall, our spectral scan has shown many similarities among the three galactic nuclei in NGC 4418 and Arp 220. Each of them has a rotating nuclear disk of molecular gas ~ 100 pc in size; the nuclear disks are also seen in dust emission in our continuum analysis in [Paper I](#). Line brightness temperatures indicate high gas temperatures of more than 100 K in the three nuclear disks. Each nucleus must be warmer toward the center, judging from the size-energy correlation among the lines, sharply peaked dust continuum intensity toward the center, and many absorption lines against the continuum peak. Vibrationally excited HCN and HC_3N are also detected among the smallest areas at the center of each nucleus. It is consistent with the greenhouse effect (i.e., continuum photon-trapping) suggested for these nuclei ([González-Alfonso & Sakamoto 2019](#)). Also common to all three nuclei is a radial motion of molecular gas around them, including the molecular outflows to the polar directions from both nuclear disks of Arp 220. NGC 4418 may also have a small-scale, collimated outflow oblique to its nuclear disk in addition to its known kpc-scale outflow perpendicular to the galactic disk.

Our data also highlighted some differences in the three nuclei. The eastern nucleus of Arp 220 is less bright in the 1 mm continuum than Arp 220W and shows less vibrational excitation in HC_3N than the western nucleus. These differences suggest that the E nucleus has less luminosity concentration or less photon trapping, or both. The two are consistent with our continuum brightness temperatures and dust opacity estimates from continuum spectral slopes ([Paper I](#)). The nuclear outflow from Arp 220W is much more prominent than those from the other two nuclei in our data.

Our spectral scan program also demonstrated the benefits of and need for wide-band observations in extragalactic studies in the ALMA era. The wide bandwidth helps to de-blend and identify overlapping lines, avoid misinterpretation in narrow-band data, and allow more reliable calibration and continuum-subtraction to facilitate accurate data analysis and interpretation. The virtue of wide-band *and* high angular resolution is evident in our findings of prevalent line absorption and systematic variations in the line-emitting areas. Both call for caution in the simple one-zone analysis of low-resolution spectral scans. Our paired study of NGC 4418 and Arp 220 also showed the effectiveness of the comparative study. The narrow and hence better-identified lines in NGC 4418 helped interpret the broad lines in the nuclei of Arp 220. Differences in their spectra also highlight the differential properties of these otherwise similar nuclei.

ACKNOWLEDGMENTS

We are grateful to the ALMA Observatory and its staff members for making the observations used here. This paper makes use of the following ALMA data: ADS/JAO.ALMA#2012.1.00377.S, ADS/JAO.ALMA#2012.1.00317.S, and ADS/JAO.ALMA#2012.1.00453.S. ALMA is a partnership of ESO (representing its member states), NSF (USA), and NINS (Japan), together with NRC (Canada), MOST and ASIAA (Taiwan), and KASI (Republic of Korea), in cooperation with the Republic of Chile. The Joint ALMA Observatory is operated by ESO, AUI/NRAO, and NAOJ. This research has made use of NASA’s Astrophysics Data System Bibliographic Services. This research has also made use of the NASA/IPAC Extragalactic Database (NED), which is operated by the Jet Propulsion Laboratory, California Institute of Technology, under contract with the National Aeronautics and Space Administration. KS is supported by grants MOST 108-2112-M-001-015 and 109-2112-M-001-020 from the Ministry of Science and Technology, Taiwan. We thank the reviewer for many constructive comments that help clarify this paper.

Facility: ALMA

Software: CASA (McMullin et al. 2007), mpfit (Moré 1977; Moré & Wright 1993; Markwardt 2009), uvmulti-fit (Martí-Vidal et al. 2014), MADCUBA (Martín et al. 2019)

REFERENCES

- Aalto, S., Booth, R. S., Black, J. H., et al. 1995, *A&A*, 300, 369
- Aalto, S., Wilner, D., Spaans, M., et al. 2009, *A&A*, 493, 481
- Aalto, S., Martín, S., Costagliola, F., et al. 2015, *A&A*, 584, A42
- Armus, L., Mazzarella, J. M., Evans, A. S., et al. 2009, *PASP*, 121, 559
- Baan, W. A., Wood, P. A. D., & Haschick, A. D. 1982, *ApJL*, 260, L49
- Barcos-Muñoz, L., Leroy, A. K., Evans, A. S., et al. 2015, *ApJ*, 799, 10
- Barcos-Muñoz, L., Aalto, S., Thompson, T. A., et al. 2018, *ApJL*, 853, L28
- Bizzocchi, L., Tamassia, F., Laas, J., et al. 2017, *ApJS*, 233, 11
- Boettcher, E., et al. 2020, *A&A*, in press
- Brown, T., & Wilson, C. D. 2019, *ApJ*, 879, 17
- Condon, J. J., Helou, G., Sanders, D. B., et al. 1990, *ApJS*, 73, 359
- Condon, J. J., Huang, Z.-P., Yin, Q. F., et al. 1991, *ApJ*, 378, 65
- Costagliola, F., & Aalto, S. 2010, *A&A*, 515, A71
- Costagliola, F., Aalto, S., Sakamoto, K., et al. 2013, *A&A*, 556, A66
- Costagliola, F., Sakamoto, K., Muller, S., et al. 2015, *A&A*, 582, A91
- Downes, D. & Solomon, P. M. 1998, *ApJ*, 507, 615
- Downes, D. & Eckart, A. 2007, *A&A*, 468, L57
- Dwek, E. & Arendt, R. G. 2020, *ApJ*, 901, 36
- Evans, A. S., Becklin, E. E., Scoville, N. Z., et al. 2003, *AJ*, 125, 2341
- Fadda, D. & Rodighiero, G. 2014, *MNRAS*, 444, L95
- Fluetsch, A., Maiolino, R., Carniani, S., et al. 2019, *MNRAS*, 483, 4586
- García-Burillo, S., Combes, F., Usero, A., et al. 2014, *A&A*, 567, A125
- 2006ApJ...640L135G Graciá-Carpio, J., García-Burillo, S., Planesas, P., et al. 2006, *ApJL*, 640, L135
- González-Alfonso, E., Smith, H. A., Fischer, J., et al. 2004, *ApJ*, 613, 247
- González-Alfonso, E., Fischer, J., Graciá-Carpio, J., et al. 2012, *A&A*, 541, A4
- González-Alfonso, E. & Sakamoto, 2019, *ApJ*, 882, 153
- Greve, T. R., Papadopoulos, P. P., Gao, Y., et al. 2009, *ApJ*, 692, 1432
- Harada, N., Herbst, E., & Wakelam, V. 2010, *ApJ*, 721, 1570
- Imanishi, M., Nakanishi, K., Kuno, N., et al. 2004, *AJ*, 128, 2037
- Jarrett, T. H., Chester, T., Cutri, R., et al. 2000, *AJ*, 119, 2498
- Kawara, K., Taniguchi, Y., Nakai, N., et al. 1990, *ApJL*, 365, L1.
- König, S., Martín, S., Muller, S., et al. 2017, *A&A*, 602, A42
- Lahuis, F., Spoon, H. W. W., Tielens, A. G. G. M., et al. 2007, *ApJ*, 659, 296
- Lutz, D., Sturm, E., Janssen, A., et al. 2020, *A&A*, 633, A134
- Markwardt, C. B. 2009, *Astronomical Data Analysis Software and Systems XVIII*, 411, 251
- Martín, S., Krips, M., Martín-Pintado, J., et al. 2011, *A&A*, 527, A36
- Martín, S., Aalto, S., Sakamoto, K., et al. 2016, *A&A*, 590, A25
- Martín, S., Martín-Pintado, J., Blanco-Sánchez, C., et al. 2019, *A&A*, 631, A159
- Martín-Pintado, J., Bachiller, R., & Fuente, A. 1992, *A&A*, 254, 315
- Martí-Vidal, I., Vlemmings, W. H. T., Muller, S., & Casey, S. 2014, *A&A*, 563, A136
- Matsushita, S., Iono, D., Petitpas, G. R., et al. 2009, *ApJ*, 693, 56
- McMullin, J. P., Waters, B., Schiebel, D., Young, W., & Golap, K. 2007, *Astronomical Data Analysis Software and Systems XVI*, 376, 127
- More, J. 1977, “The Levenberg-Marquardt Algorithm: Implementation and Theory,” in *Numerical Analysis*, vol. 630, ed. G. A. Watson (Springer-Verlag: Berlin), 105
- More, J. & Wright, S. 1993, *Optimization Software Guide*, *Frontiers in Applied Mathematics*, vol. 14, (Philadelphia, PA: SIAM)
- Norris, R. P. 1988, *MNRAS*, 230, 345
- Ohya, Y., Sakamoto, K., Aalto, S., et al. 2019, *ApJ*, 871, 191
- Pearson, T. J. 1999, *Synthesis Imaging in Radio Astronomy II*, 180, 335
- Rangwala, N., Maloney, P. R., Glenn, J., et al. 2011, *ApJ*, 743, 94
- Rangwala, N., Maloney, P. R., Wilson, C. D., et al. 2015, *ApJ*, 806, 17
- Rieke, G. H., Cutri, R. M., Black, J. H., et al. 1985, *ApJ*, 290, 116
- Roche, P. F., Aitken, D. K., Smith, C. H., & James, S. D. 1986, *MNRAS*, 218, 19P
- Rolfs, R., Schilke, P., Wyrowski, F., et al. 2011, *A&A*, 527, A68

- Rosenberg, M. J. F., van der Werf, P. P., Aalto, S., et al. 2015, *ApJ*, 801, 72
- Rowan-Robinson, M., & Crawford, J. 1989, *MNRAS*, 238, 523
- Sakamoto, K., Scoville, N. Z., Yun, M. S., et al. 1999, *ApJ*, 514, 68
- Sakamoto, K., Wang, J., Wiedner, M. C., et al. 2008, *ApJ*, 684, 957-977
- Sakamoto, K., Aalto, S., Wilner, D. J., et al. 2009, *ApJL*, 700, L104
- Sakamoto, K., Aalto, S., Evans, A. S., Wiedner, M. C., & Wilner, D. J. 2010, *ApJL*, 725, L228
- Sakamoto, K., Aalto, S., Costagliola, F., et al. 2013, *ApJ*, 764, 42
- Sakamoto, K., Aalto, S., Barcos-Muñoz, L., et al. 2017, *ApJ*, 849, 14
- Sakamoto, K., Gonzalez-Alfonso, E., Martin, S., et al. 2021, *ApJ* in press (paper I), arXiv:2109.06695
- Sanders, D. B., and Mirabel, I. F. 1996, *ARA&A*, 34, 749
- Scoville, N. Z., Yun, M. S., and Bryant, P. M. 1997, *ApJ*, 484, 702
- Scoville, N. Z., Evans, A. S., Dinshaw, N., et al. 1998, *ApJL*, 492, L107
- Scoville, N., Sheth, K., Walter, F., et al. 2015, *ApJ*, 800, 70
- Scoville, N., Murchikova, L., Walter, F., et al. 2017, *ApJ*, 836, 66
- Smith, H. E., Lonsdale, C. J., Lonsdale, C. J., & Diamond, P. J. 1998, *ApJL*, 493, L17
- Soifer, B. T., Helou, G., Lonsdale, C. J., et al. 1984, *ApJL*, 283, L1
- Soifer, B. T., Neugebauer, G., Matthews, K., et al. 1999, *ApJ*, 513, 207
- Thorwirth, S., Müller, H. S. P., Lewen, F., et al. 2000, *A&A*, 363, L37
- Tunnard, R., Greve, T. R., Garcia-Burillo, S., et al. 2015, *ApJ*, 800, 25
- Van der Tak, F. F. S., Aalto, S., & Meijerink, R. 2008, *A&A*, 477, L5
- Varenius, E., Conway, J. E., Martí-Vidal, I., et al. 2014, *A&A*, 566, A15
- Varenius, E., Conway, J. E., Martí-Vidal, I., et al. 2016, *A&A*, 593, A86
- Varenius, E., Costagliola, F., Klöckner, H.-R., et al. 2017, *A&A*, 607, A43
- Varenius, E., Conway, J. E., Batejat, F., et al. 2019, *A&A*, 623, A173
- Veilleux, S., Rupke, D. S. N., Kim, D.-C., et al. 2009, *ApJS*, 182, 628
- Veilleux, S., Meléndez, M., Sturm, E., et al. 2013, *ApJ*, 776, 27
- Wheeler, J., Glenn, J., Rangwala, N., et al. 2020, *ApJ*, 896, 43
- Wilson, C. D., Rangwala, N., Glenn, J., et al. 2014, *ApJL*, 789, L36
- Wilson, T. L., Rohlfs, K., & Hüttemeister, S. 2009, *Tools of Radio Astronomy*, by Thomas L. Wilson; Kristen Rohlfs and Susanne Hüttemeister. ISBN 978-3-540-85121-9. Published by Springer-Verlag, Berlin, Germany, 2009.
- Wynn-Williams, C. G. & Becklin, E. E. 1993, *ApJ*, 412, 535. doi:10.1086/172941
- Zschaechner, L. K., Ott, J., Walter, F., et al. 2016, *ApJ*, 833, 41

Table 1. Summary of Observations

Parameter	Value
ALMA Band	6, 7, 9
Frequency Coverage	67 GHz in $f_{\text{rest}}=215\text{--}697$ GHz
Frequency Resolution	0.98 MHz
Primary Beam Size	$24''\text{--}8''$
Angular resolution	$0''.14\text{--}0''.28$ in $(\theta_{\text{maj}}\theta_{\text{min}})^{1/2}$ $0''.35$ in $\max \theta_{\text{maj}}$
Max. Recoverable Scale	$11''\text{--}3''$
Sensitivity $\sigma_{50 \text{ km/s}}$	0.6, 1.0, 8 mJy (native beam) $^{-1}$
in Band 6, 7, 9	0.3, 0.6, 0.6 K for native beam 0.1, 0.1, 0.2 K at $0''.35$ resolution

NOTE— Angular resolution is given in the geometrical mean of the major- and minor-axis FWHM as well as in the maximum of the major-axis FWHM of the synthesized beam. Sensitivity is for typical values in Band 6, 7, and 9, respectively. The native beam is the one from imaging at `robust=0.5`. See [Paper I](#) for more information about the ALMA observations and data reduction.

Table 2. Frequency Coverage

Band	Rest frequency / GHz	
	ranges	width
(1)	(2)	(3)
NGC 4418		
9	678.309–685.206, 690.081–697.039	13.9
7	340.939–366.574	25.6
6	248.777–255.533, 264.570–271.520 215.633–222.265, 229.225–236.096	27.2
Arp 220		
9	669.675–676.606, 696.460–689.423	14.0
7	341.132–367.057	25.9
6	243.856–254.088, 263.224–270.251 218.265–221.658, 228.595–235.403	27.5

NOTE— (1) ALMA receiver band. (2) Ranges of rest frequency we observed. For the conversion to rest frequency we used $V(\text{radio, LSRK})=2100 \text{ km s}^{-1}$ and 5350 km s^{-1} for NGC 4418 and Arp 220, respectively. (3) Total frequency coverage in each band. Our total coverage is 66.7 and 67.4 GHz for NGC 4418 and Arp 220, respectively.

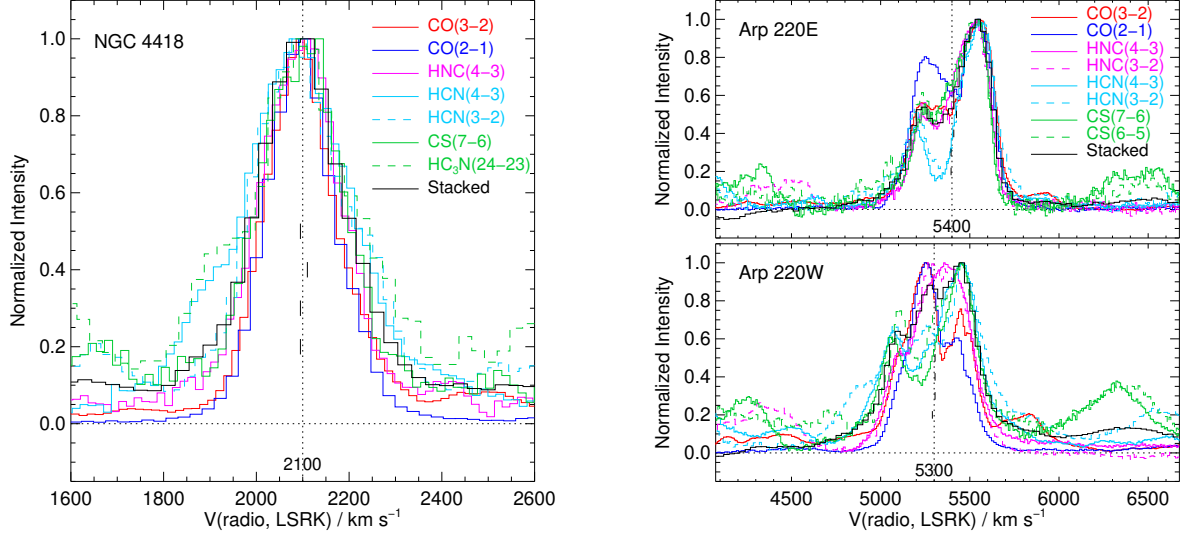


Figure 1. Continuum-subtracted line profiles of NGC 4418 (left) and Arp 220 nuclei (right) to estimate their velocities. The data of NGC 4418 are from this work and are from the $0''.35$ resolution data sampled in a $1''$ -diameter aperture. Arp 220 data are from our companion spectral scan at resolutions of $0''.65 - 0''.82$. Individual line profiles are normalized with their peak values and are averaged to produce the mean line profile whose normalized shape is shown in black. The central velocities of the mean profile at the levels of 20, 30, 40, and 50% of its peak are shown with black vertical bars. The fiducial velocities of the nuclei that we adopted are indicated with vertical dotted lines.

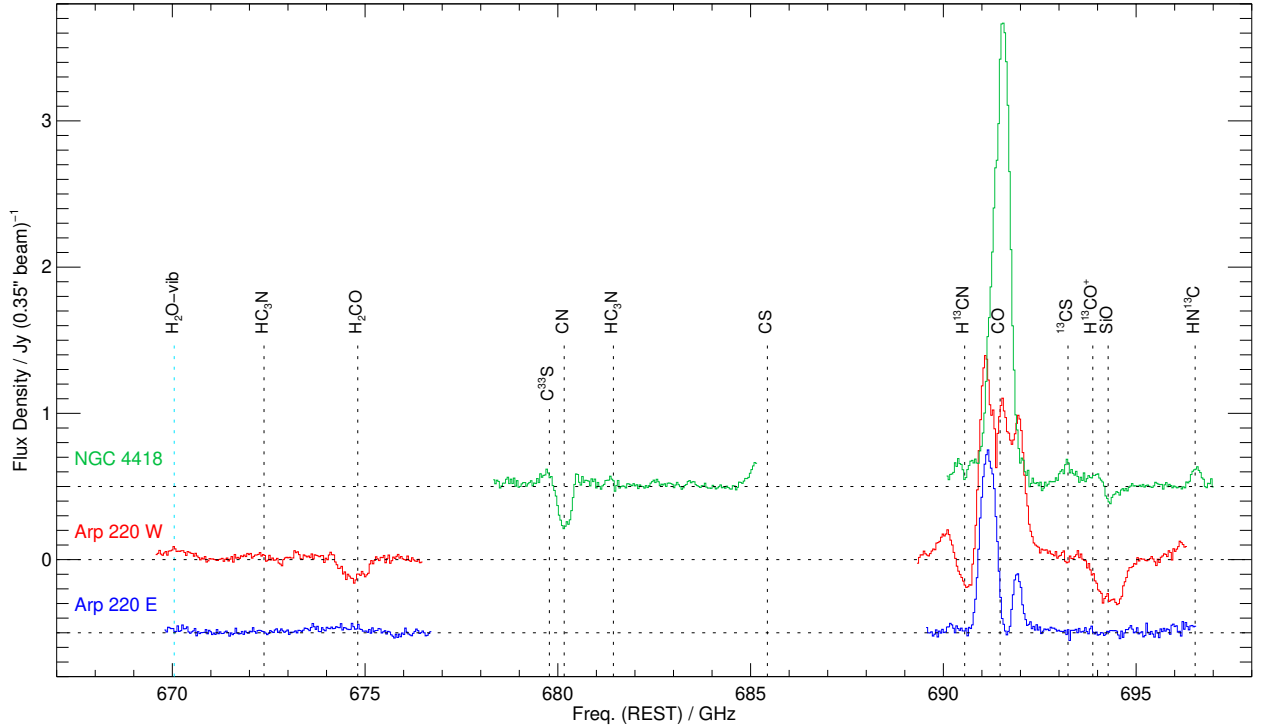
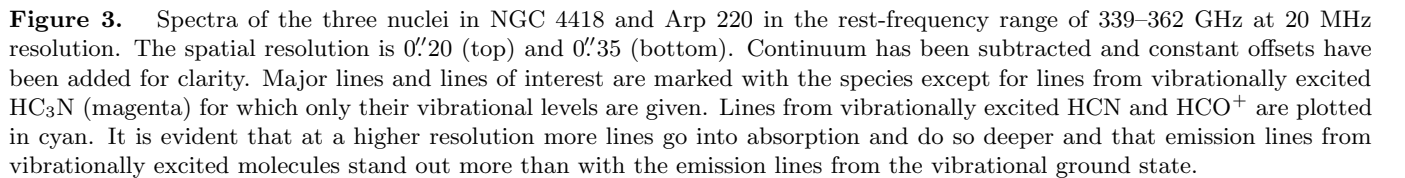


Figure 2. Spectra of the three nuclei in NGC 4418 and Arp 220 in the rest-frequency range of 670–697 GHz sampled in a $0''.35$ beam at 40 MHz resolution. Continuum has been subtracted and constant offsets are added for clarity. Major lines and lines of interest are marked with the species. Among them, HC_3N is not firmly detected unlike in lower bands and vibrationally excited H_2O is only a possible identification. CN consists of a dozen transitions spanning 0.29 GHz; it is plotted at their intensity-weighted mean frequency.



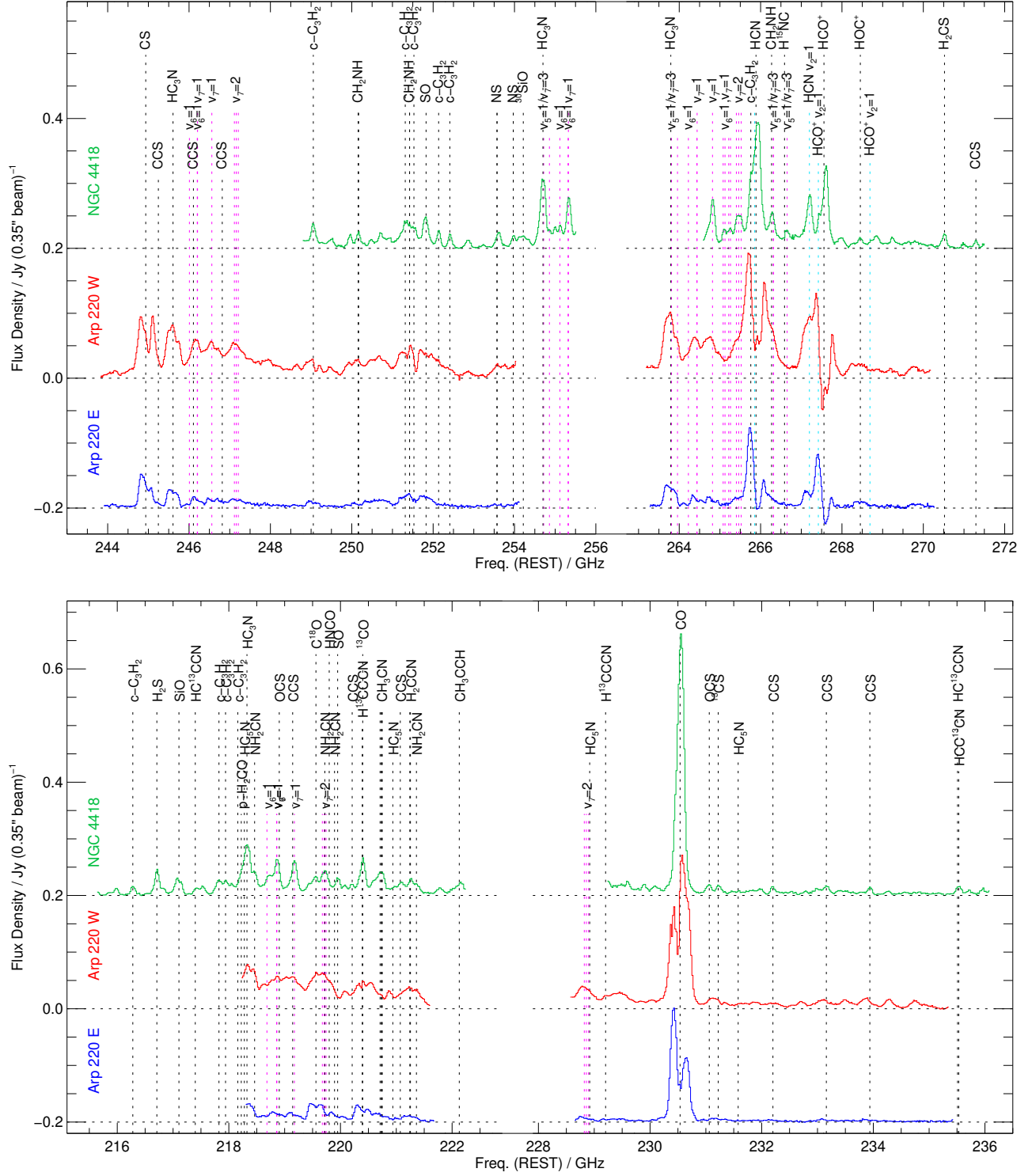


Figure 4. Spectra of the three nuclei in NGC 4418 and Arp 220 in the rest-frequency range of 244–272 GHz (top) and 215–236 GHz (bottom) sampled in a 0''.35 beam at 20 MHz resolution. Continuum has been subtracted and constant offsets are added for clarity. Major lines and lines of interest are marked with the species except for lines from vibrationally excited HC₃N (magenta) for which only their vibrational levels are given. Lines from vibrationally excited HCN and HCO⁺ are plotted in cyan.

Table 3. Parameters of the Line Channel Maps

Species	Transition	f_{rest}	$\sigma_{50 \text{ km/s}}$	$\max I_\nu $	p	Figure	Nearby Lines
		GHz	mJy beam ⁻¹	K	K		
(1)	(2)	(3)	(4)	(5)	(6)	(7)	(8)
NGC 4418							
HN ¹³ C	J=8–7	696.532	8.5	0.55	6.8	1.0	5a
SiO	J=16–15	694.275	7.3	0.45	–7.7	1.0	5b H ¹³ CO ⁺ @2271
¹³ CS	J=14–13	693.234	15.6	1.56	15.3	1.0	5c H ¹³ CO ⁺ @1824
CO	J=6–5	691.473	14.5	1.45	120.3	1.7	5d H ¹³ CN@2497
H ¹³ CN	J=8–7	690.552	15.1	1.58	20.9	1.0	5e CO@1703
CN	N=6–5 ^a	680.165	12.2	1.23	–36.0	1.5	5f C ³³ S@2268
HC ₃ N	$v_7=1$, J=40–39, $l=1f$	365.195	1.31	0.50	34.6	1.5	6a
HC ₃ N	$v_7=1$, J=40–39, $l=1e$	364.676	1.18	0.45	32.0	1.5	6b H ₃ O ⁺ @2001, HC ₃ N($v_6=1f$)@2108
HC ₃ N	J=40–39	363.785	1.18	0.56	28.9	1.5	6c
HNC	J=4–3	362.630	1.65	0.86	54.4	1.5	6d
HCO ⁺	J=4–3	356.734	1.21	0.63	38.5	1.5	6e HCN($v_2=1, l=1f$)@2499
HCN	$v_2=1$, J=4–3, $l=1f$	356.256	1.80	0.85	43.0	1.5	6f HCO ⁺ @1700
HCN	J=4–3	354.505	1.66	0.82	55.1	1.5	6g HC ₃ N(39–38)@1939, HCN($v_2=1, l=1e$)@2138
C ₂ H	N=4–3	349.365 ^b	1.06	0.54	35.9	1.5	6h
HN ¹³ C	J=4–3	348.340	1.15	0.63	28.3	1.5	6i
SiO	J=8–7	347.331	1.11	0.54	19.5	1.5	6j H ¹³ CO ⁺ @2385
H ¹³ CO ⁺	J=4–3	346.998	1.01	0.48	29.9	1.5	6k SiO@1815
CO	J=3–2	345.795	1.01	0.47	144.0	2.2	6l HC ₃ N(38–37)@2261, H ¹³ CN@2493
H ¹³ CN	J=4–3	345.340	1.05	0.51	33.0	1.5	6m CO@1707
CS	J=7–6	342.883	1.35	0.65	37.3	1.5	6n
HCO ⁺	J=3–2	267.558	0.99	0.28	26.6	1.7	7a HCN($v_2=1, l=1f$)@2499
HCN	$v_2=1$, J=3–2, $l=1f$	267.199	0.94	0.26	21.3	1.7	7b HCO ⁺ @1701
HCN	J=3–2	265.886	0.81	0.22	40.2	1.7	7c HCN($v_2=1, l=1e$)@2137
HC ₃ N	$v_7=1$, J=28–27, $l=1e$	255.325	0.58	0.24	28.9	1.7	7d HC ₃ N($v_6=1f$)@2109
HC ₃ N	J=28–27	254.700	0.47	0.19	32.4	1.7	7e
CO	J=2–1	230.538	0.63	0.24	123.9	2.2	7f
¹³ CO	J=2–1	220.399	0.54	0.22	22.7	1.7	7g
C ¹⁸ O	J=2–1	219.560	0.70	0.31	13.6	1.7	7h
HC ₃ N	$v_7=1$, J=24–23, $l=1f$	219.174	0.81	0.35	25.2	1.7	7i
HC ₃ N	J=24–23	218.325	0.80	0.32	31.7	1.7	7j
SiO	J=5–4	217.105	0.55	0.21	16.8	1.7	7k
H ₂ S	J=2 _{2,0} –2 _{1,1}	216.710	0.69	0.23	16.8	1.7	7l
Arp 220							
SiO	J=16–15	694.275	11.3	0.97	–24.4	1.4	8a H ¹³ CO ⁺ @5519, ¹³ CS@5792
CO	J=6–5	691.473	9.8	0.83	66.5	1.6	8b H ¹³ CN@5742
H ₂ CO	J=9 _{1,8} –8 _{1,7}	674.810	9.5	0.78	–13.0	1.0	8c
HNC	J=4–3	362.630	1.78	0.70	72.3	1.5	9a
HCO ⁺	J=4–3	356.734	1.28	0.52	–54.5	1.5	9b HCN($v_2=1, l=1f$)@5745
HCN	$v_2=1$, J=4–3, $l=1f$	356.256	1.37	0.56	41.6	1.5	9c HCO ⁺ @4954
HCN	J=4–3	354.505	1.36	0.61	71.3	1.5	9d HC ₃ N(39–38)@5191, HCN($v_2=1, l=1e$)@5387
C ₂ H	N=4–3	349.365 ^b	1.29	0.53	36.2	1.5	9e
SiO	J=8–7	347.331	1.04	0.43	–45.9	1.5	9f H ¹³ CO ⁺ @5632
CO	J=3–2	345.795	1.15	0.48	106.0	1.8	9g HC ₃ N(38–37)@5509, H ¹³ CN@5738
CS	J=7–6	342.883	1.26	0.56	39.0	1.5	9h
HCO ⁺	J=3–2	267.558	0.94	0.41	37.7	1.5	10a HCN($v_2=1, l=1f$)@5744
HCN	$v_2=1$, J=3–2, $l=1f$	267.199	0.89	0.38	31.4	1.5	10b HCO ⁺ @4955
HCN	J=3–2	265.886	0.89	0.36	55.4	1.7	10c HCN($v_2=1, l=1e$)@5387
CS	J=5–4	244.936	0.57	0.27	39.5	1.7	10d
CO	J=2–1	230.538	0.68	0.31	77.2	1.8	10e

NOTE— (3) Line rest frequency from Splatalogue^a. (4)–(5) Noise rms in 50 km s⁻¹ channel maps. (6) Peak Rayleigh-Jeans brightness temperature of the line in our channel maps. Brighter blending lines are excluded from the search. A negative value is listed when the deepest absorption has a larger absolute intensity than the brightest emission. (7) The power-law index used for contouring. (8) Figure and panel ID of the channel maps. (9) **Major species** whose lines **may be blended with** or close to the line in Columns (1) and (2). Not all of them are firmly detected, and we do not list all possible blending either. Numbers after @ are the velocities at which the blending lines at the reference velocity of the galaxy (2100 km s⁻¹ for NGC 4418 and 5350 km s⁻¹ for Arp 220) would appear in the data of the blended lines. For example, a transition of H₃O⁺ at 2100 km s⁻¹ should be at 2001 km s⁻¹ of HC₃N($v_7=1$, J=40–39, $l=1e$).

^a Weighted mean frequency of twelve hyper-fine transitions in CN(N=6–5, J=11/2–9/2) and CN(N=6–5, J=13/2–11/2). The weight is $g_u A$ where g_u is the statistical weights of the upper state and A is the Einstein's A coefficient.

^b The four strongest transitions in Splatalogue are in the range of $f_{\text{rest}}=349.337\text{--}349.400$ GHz and are blended in our data. We use their strength-weighted mean frequency.

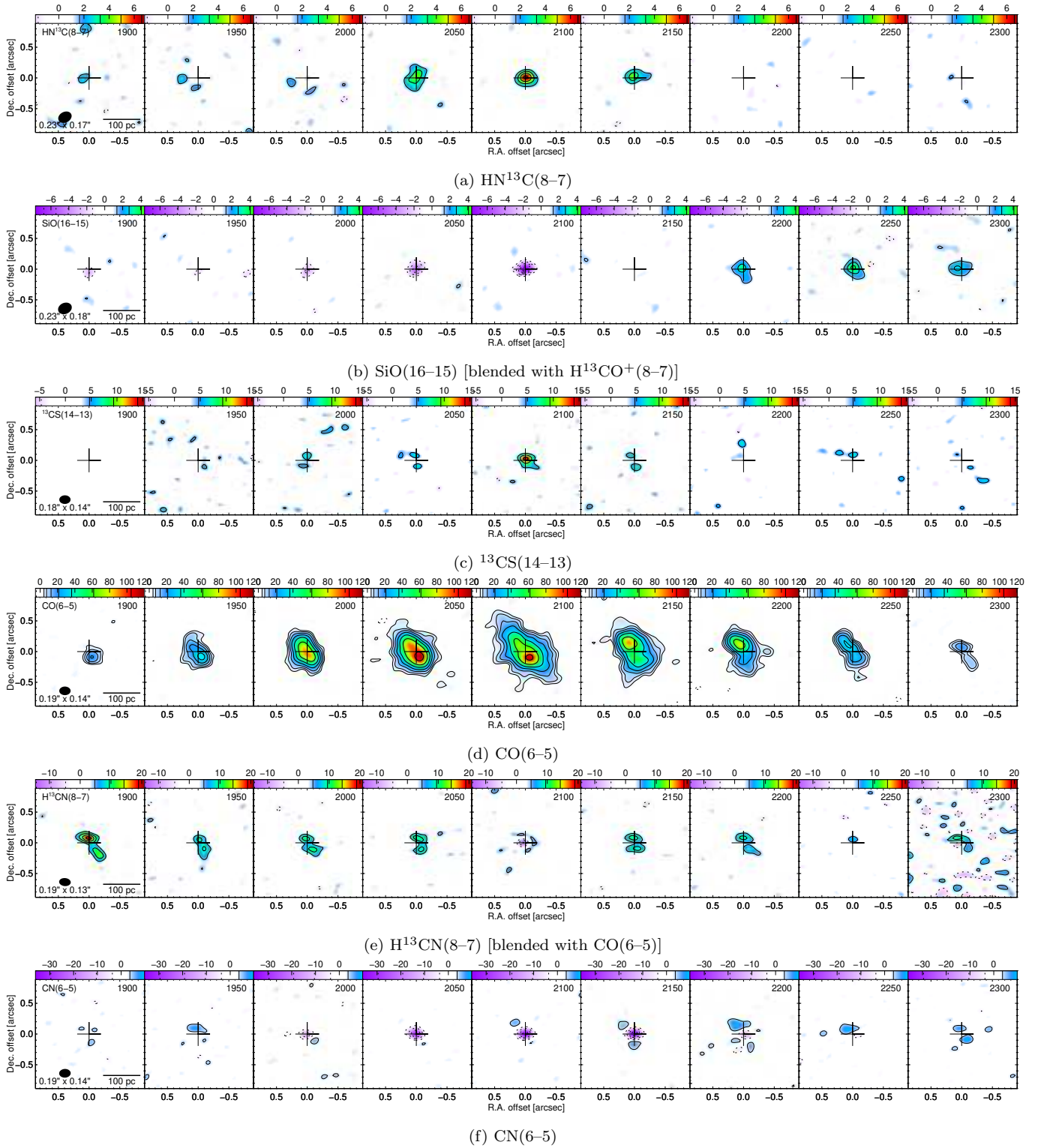


Figure 5. NGC 4418 channel maps of 50 km s^{-1} width for major lines in the ALMA Band 9. Contours are at $\pm 3n^p\sigma$ for $n = 1, 2, 3, \dots$; the index p and the rms noise per 50 km s^{-1} channel σ are in Table 3. Negative contours are dashed. Velocity (LSRK, radio) in km s^{-1} is in the upper-right corner of each channel map. The crosses are at the continuum positions of the nuclei. The synthesized beam, labeled with its FWHM, is shown in the bottom-left corner of the first channel. The intensity color wedges are labeled with brightness temperature in Kelvin.

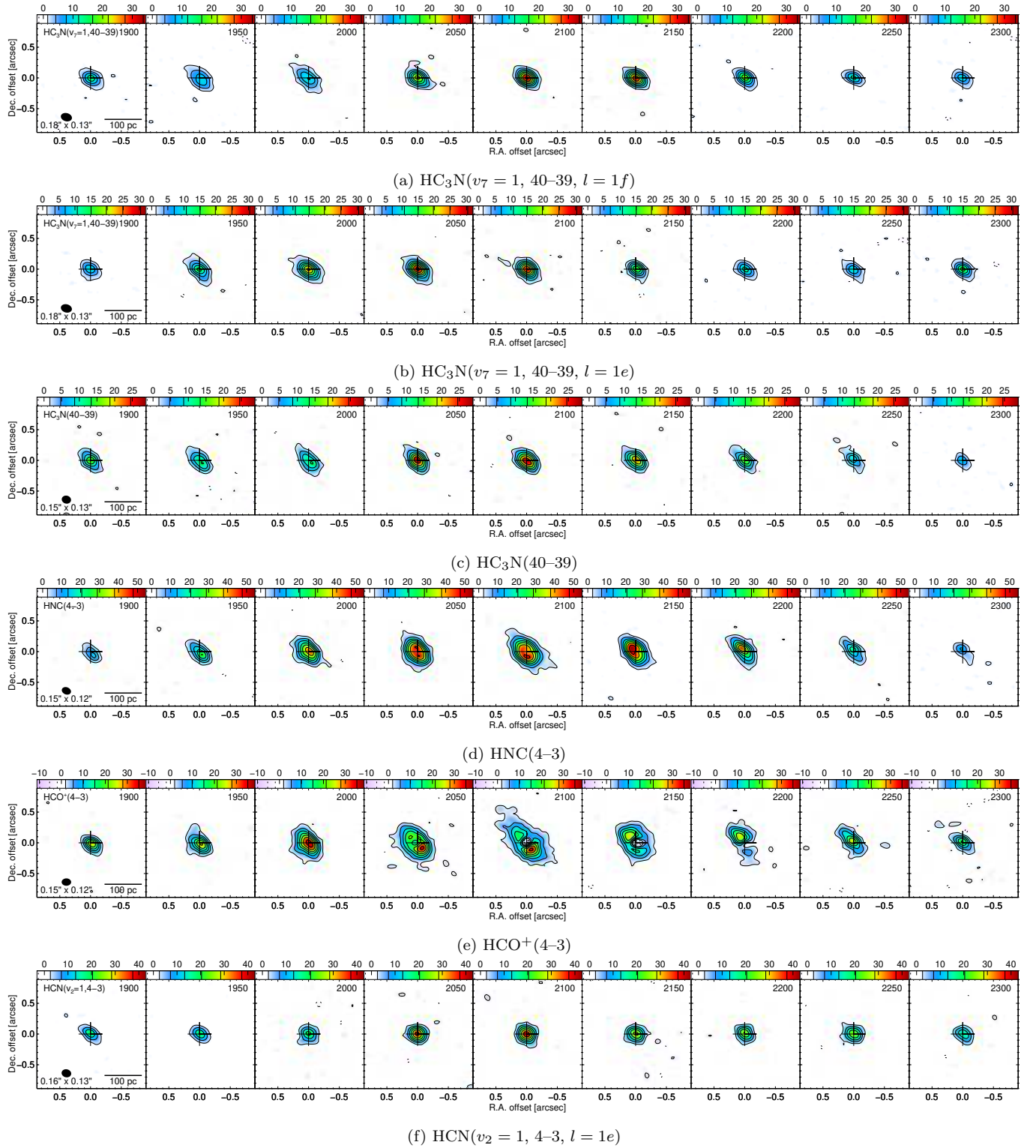


Figure 6. NGC 4418 channel maps of 50 km s^{-1} width for major lines in the ALMA Band 7. Contours are at $\pm 3n^p\sigma$ for $n = 1, 2, 3, \dots$; the index p and the rms noise per 50 km s^{-1} channel σ are in Table 3. Negative contours are dashed. Velocity (LSRK, radio) in km s^{-1} is in the upper-right corner of each channel map. The crosses are at the continuum positions of the nuclei. The synthesized beam, labeled with its FWHM, is shown in the bottom-left corner of the first channel. The intensity color wedges are labeled with brightness temperature in Kelvin.

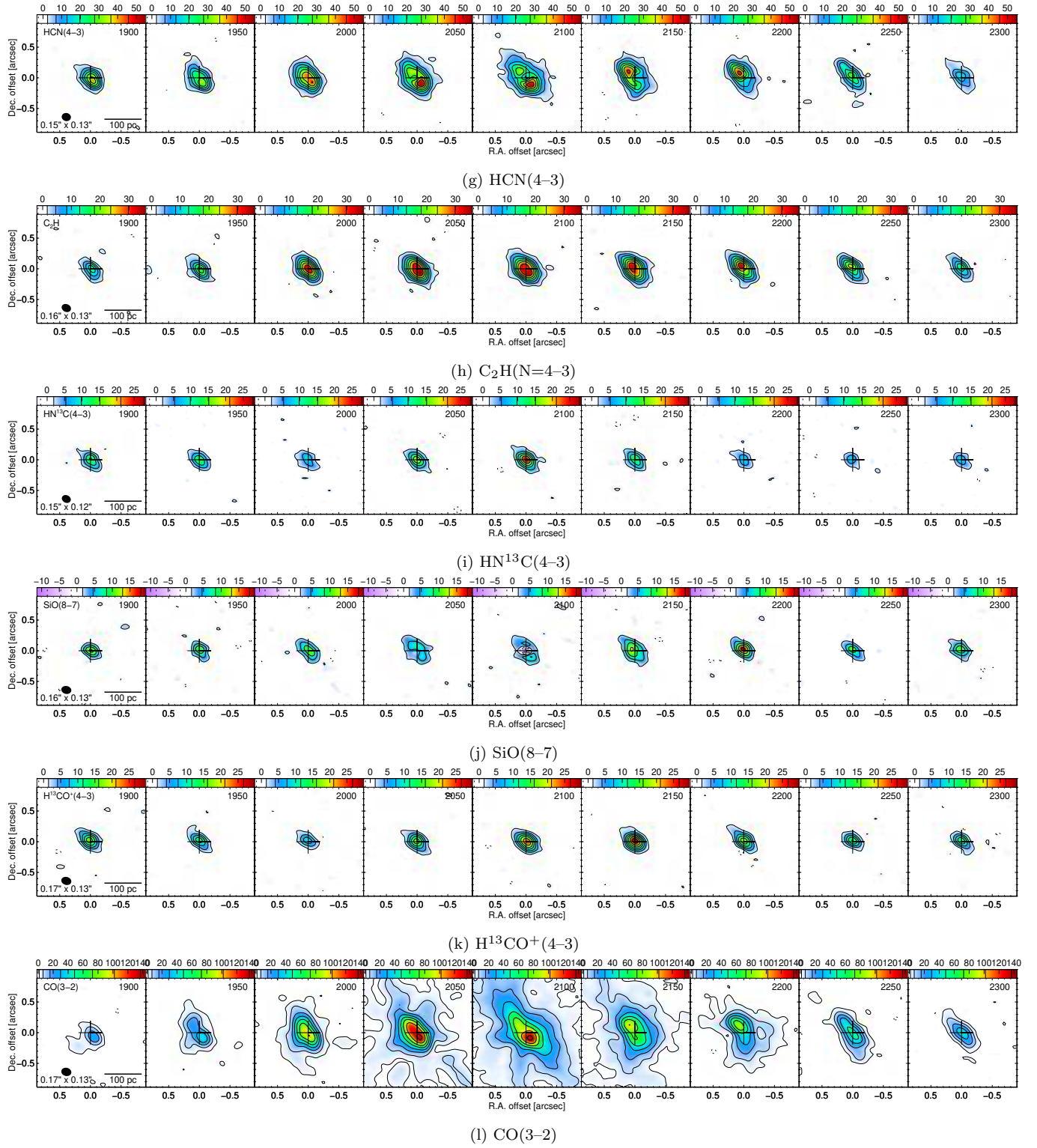


Figure 6 (continued).

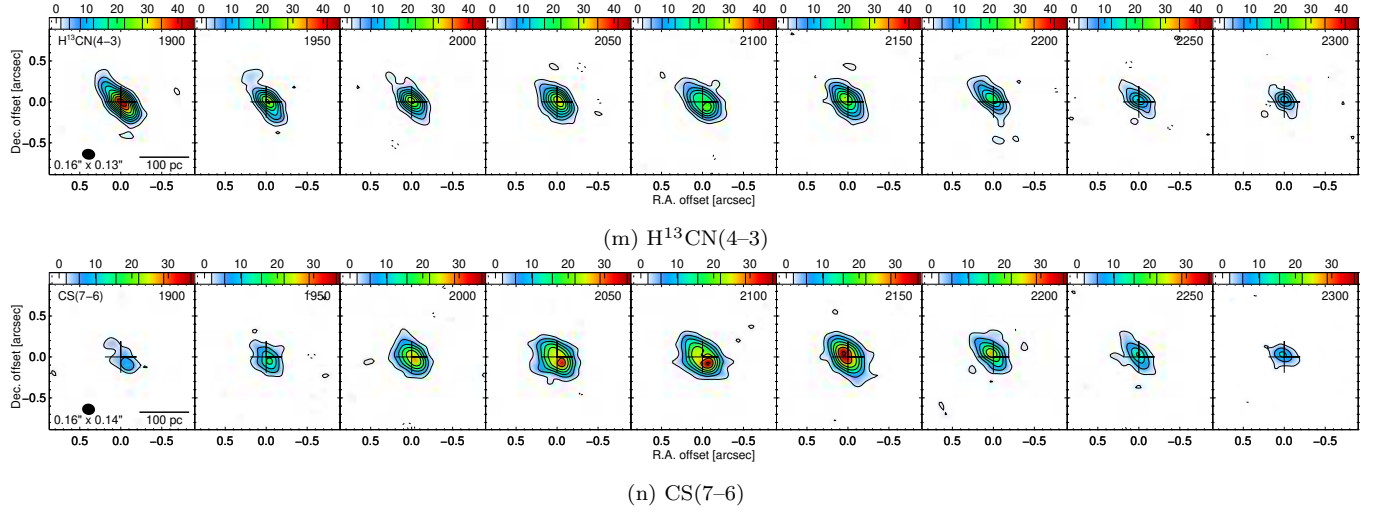


Figure 6 (continued).

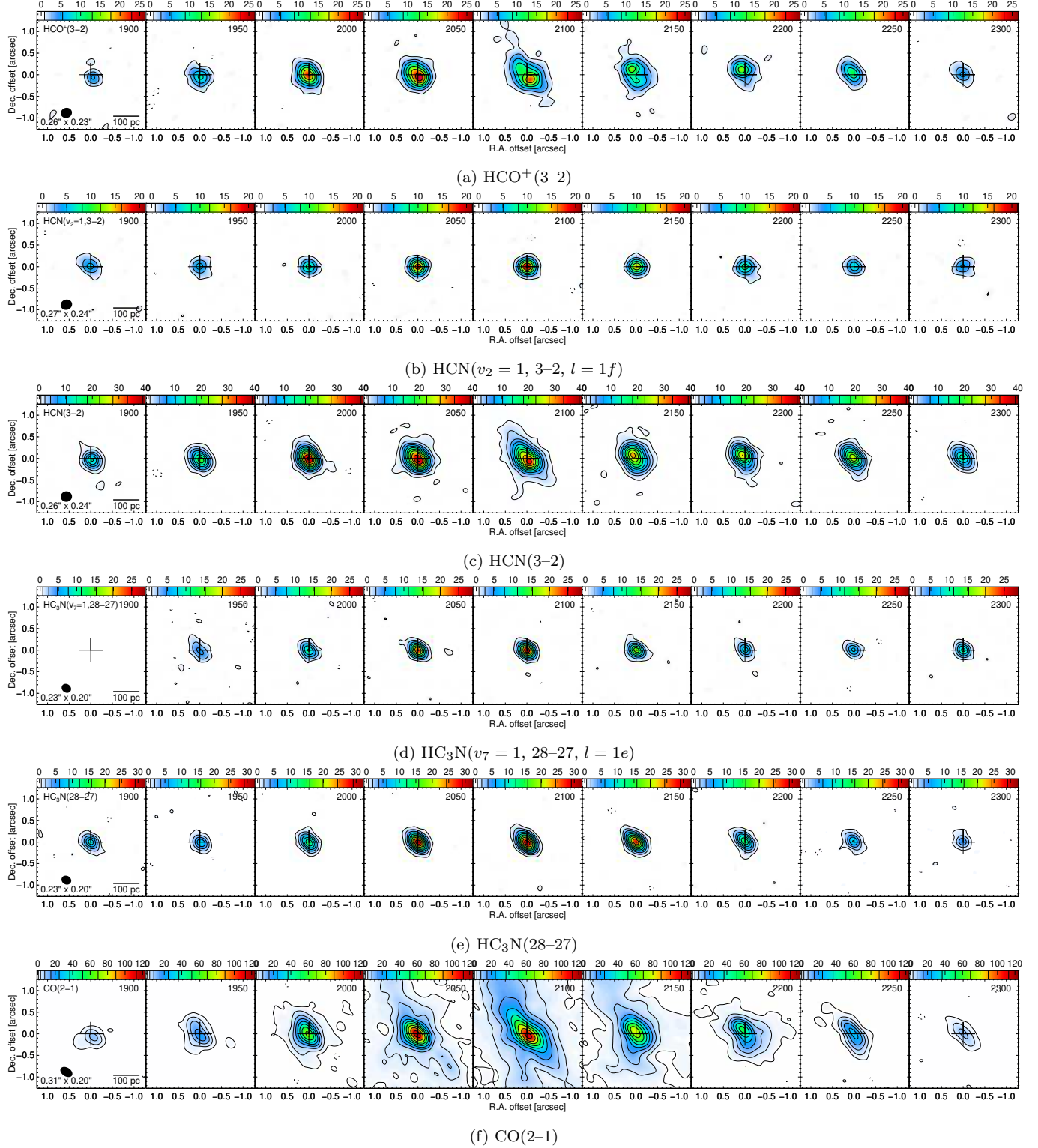


Figure 7. NGC 4418 channel maps of 50 km s^{-1} width for major lines in the ALMA Band 6. Other descriptions are the same as in Fig. 6. The first channel of panel (d) is at the edge of our bandpass and is flagged.

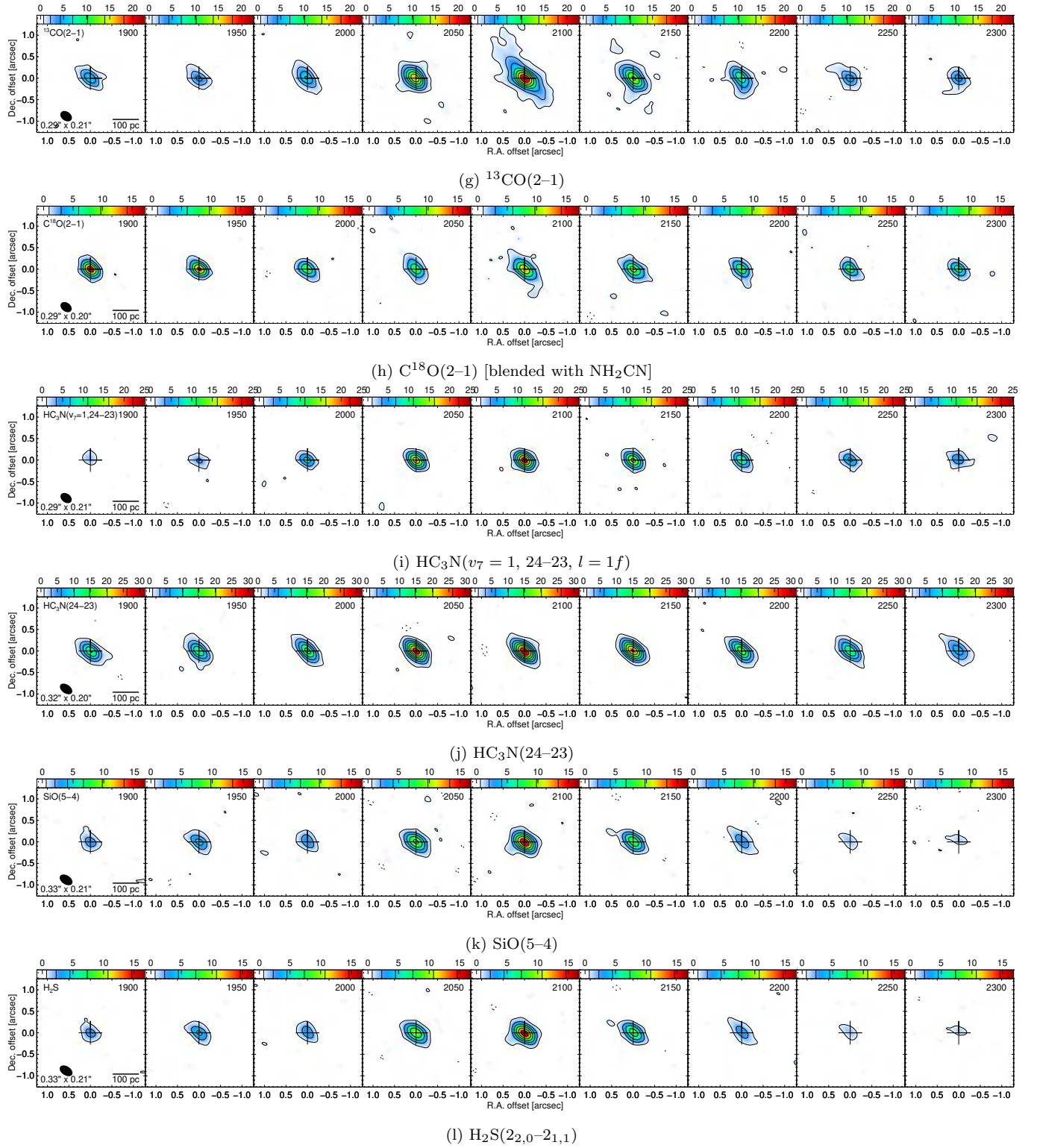


Figure 7 (continued).

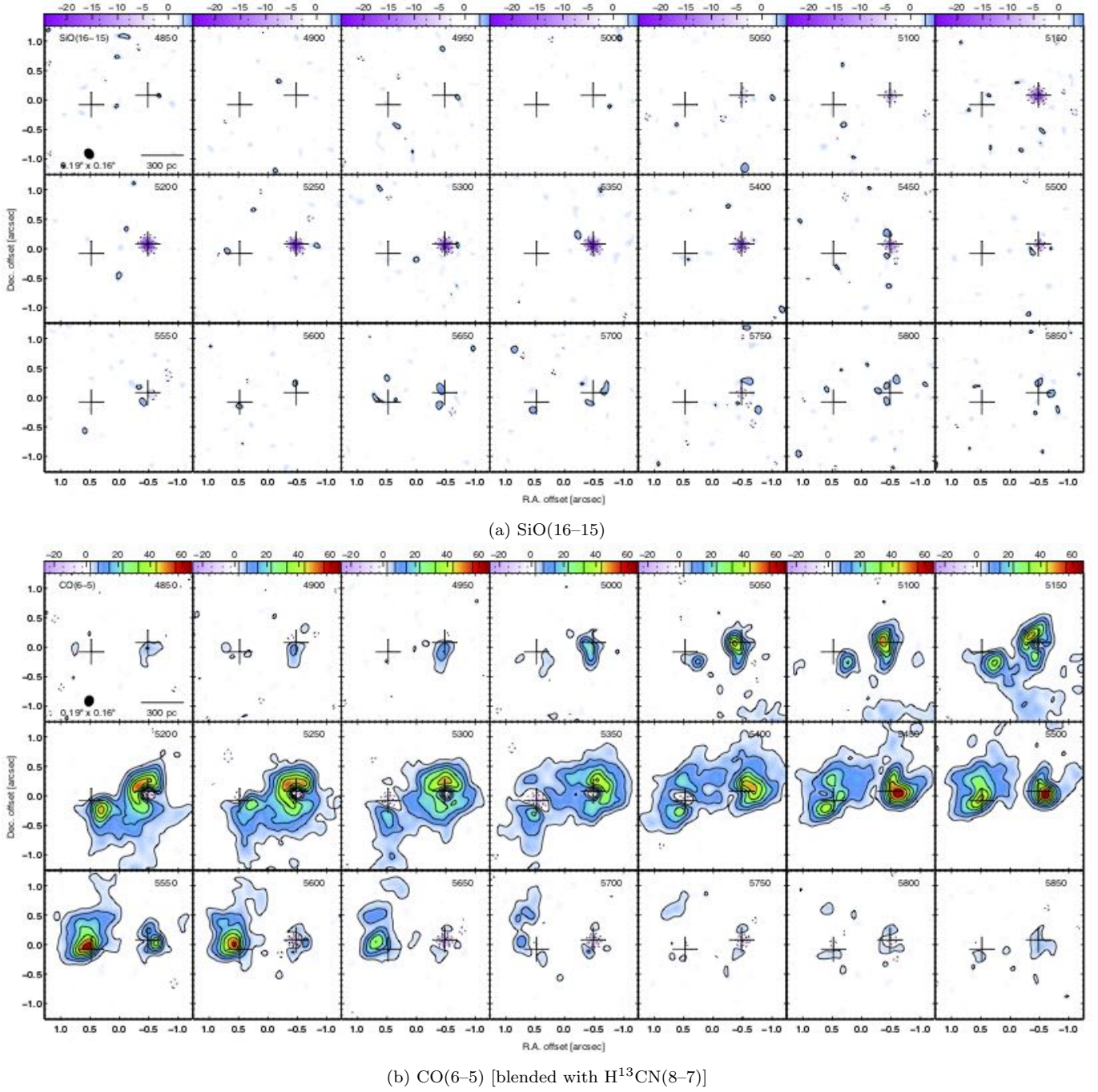


Figure 8. Arp 220 channel maps for major lines in Band 9. Contours are at $\pm 3n^p\sigma$ for $n = 1, 2, 3, \dots$, where the index p and the rms noise per 50 km s^{-1} channel σ are in Table 3. Negative contours are dashed. Velocity (LSRK, radio) in km s^{-1} is in the upper-right corner of each channel map. The crosses are at the continuum positions of the nuclei. The synthesized beam, labeled with its FWHM, is shown in the bottom-left corner of the first channel. The intensity color wedges are labeled with brightness temperature in Kelvin. Major line-blendings are indicated in sub-panel titles and more information is in Table 3.

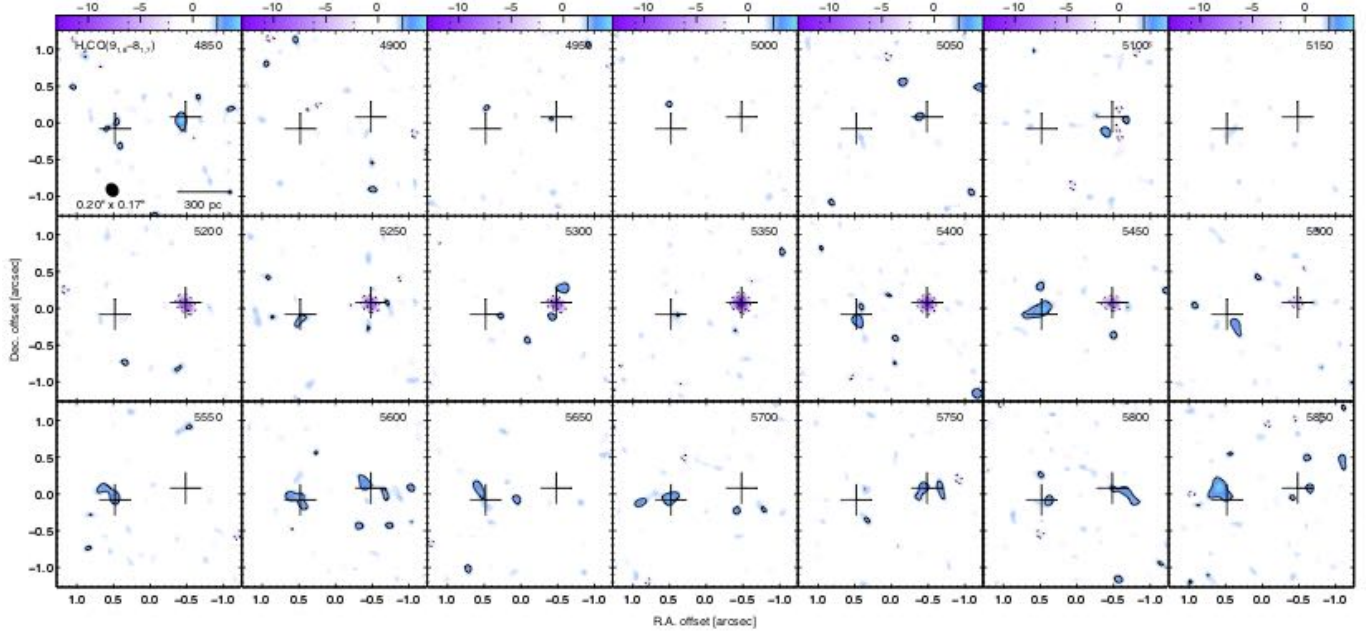


Figure 8 (continued).

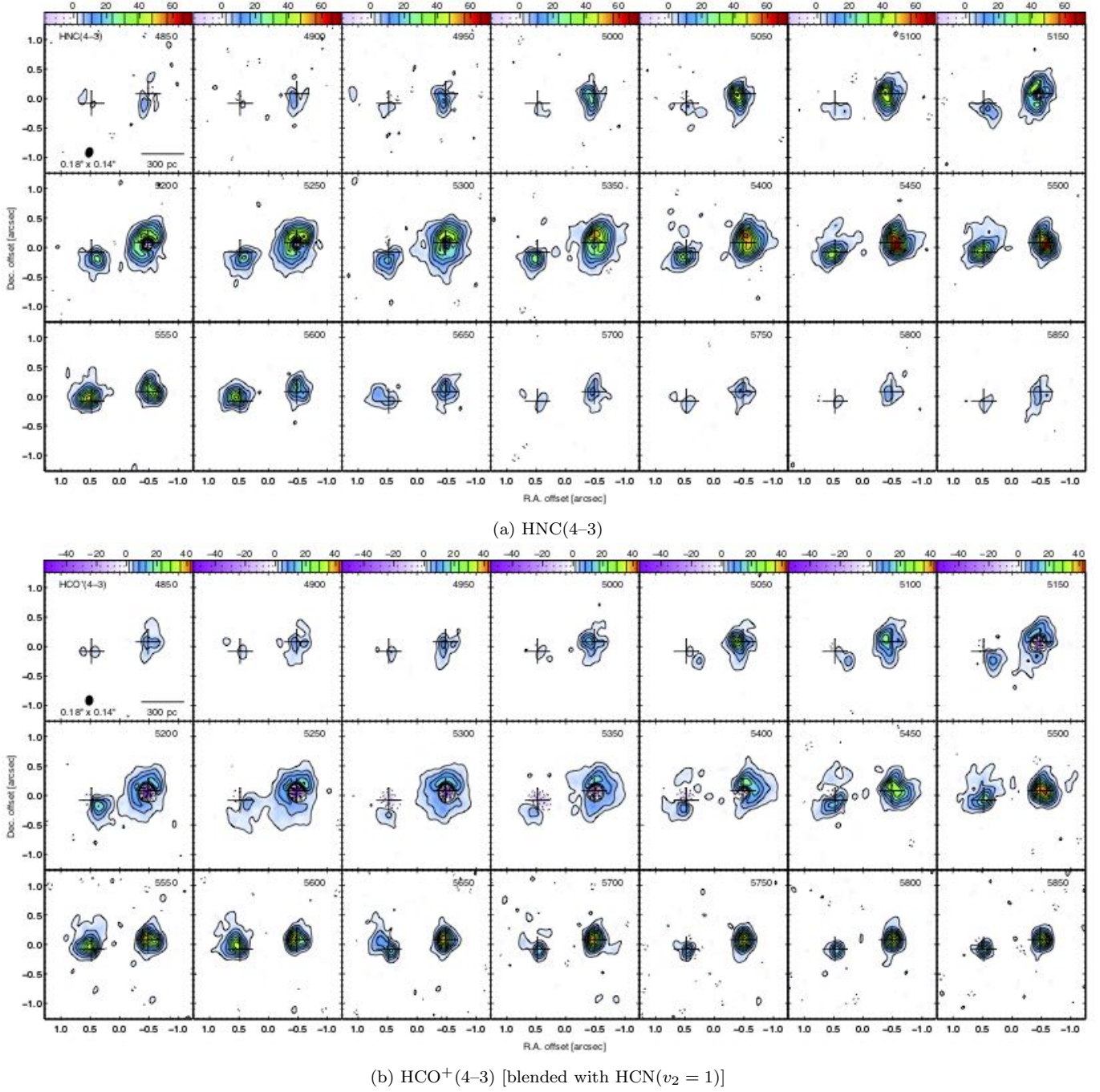
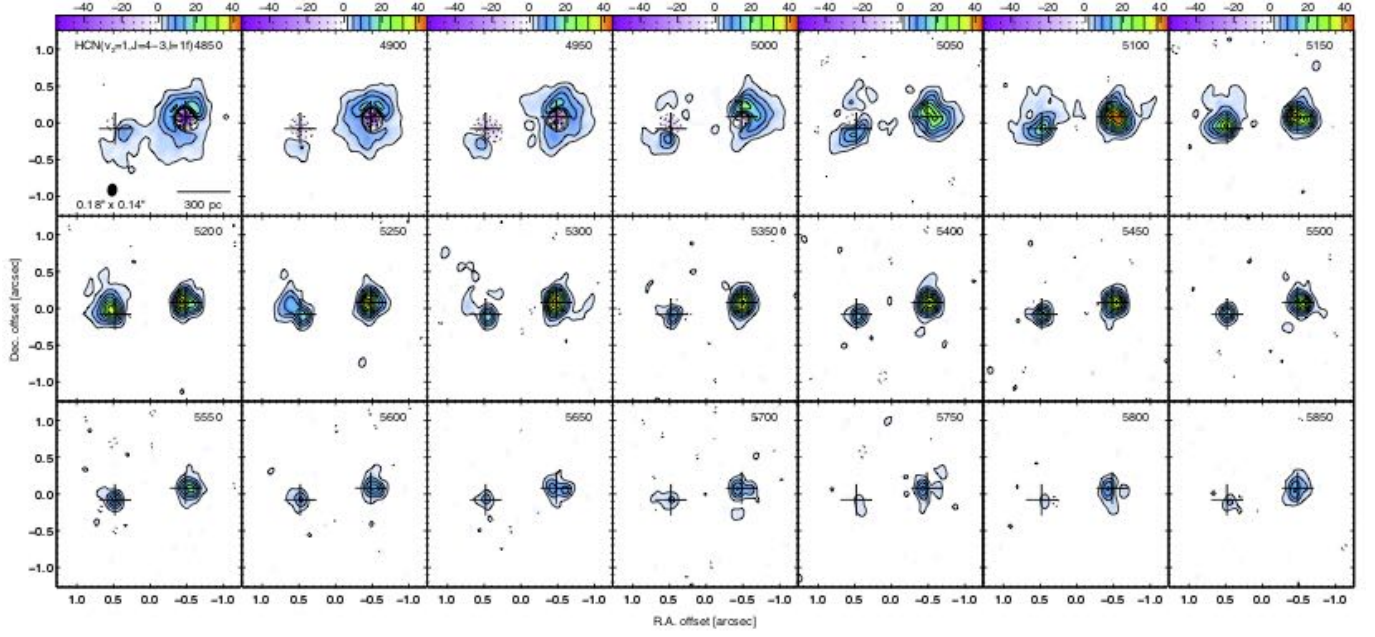
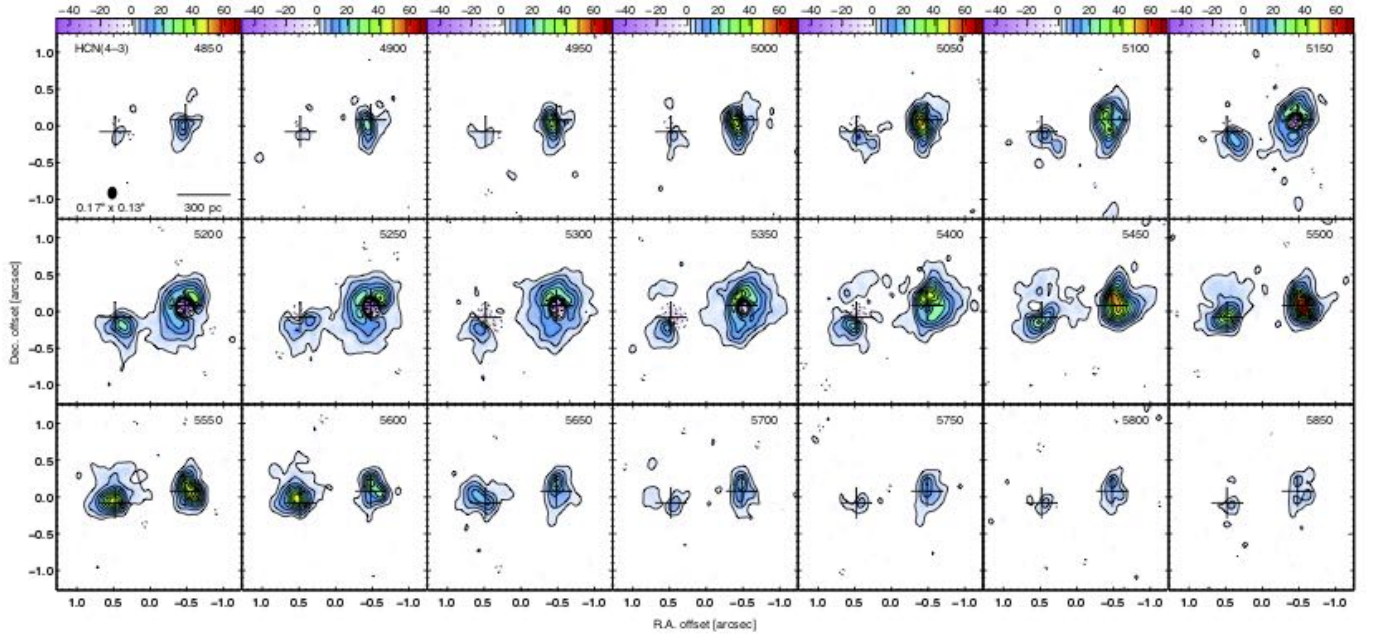
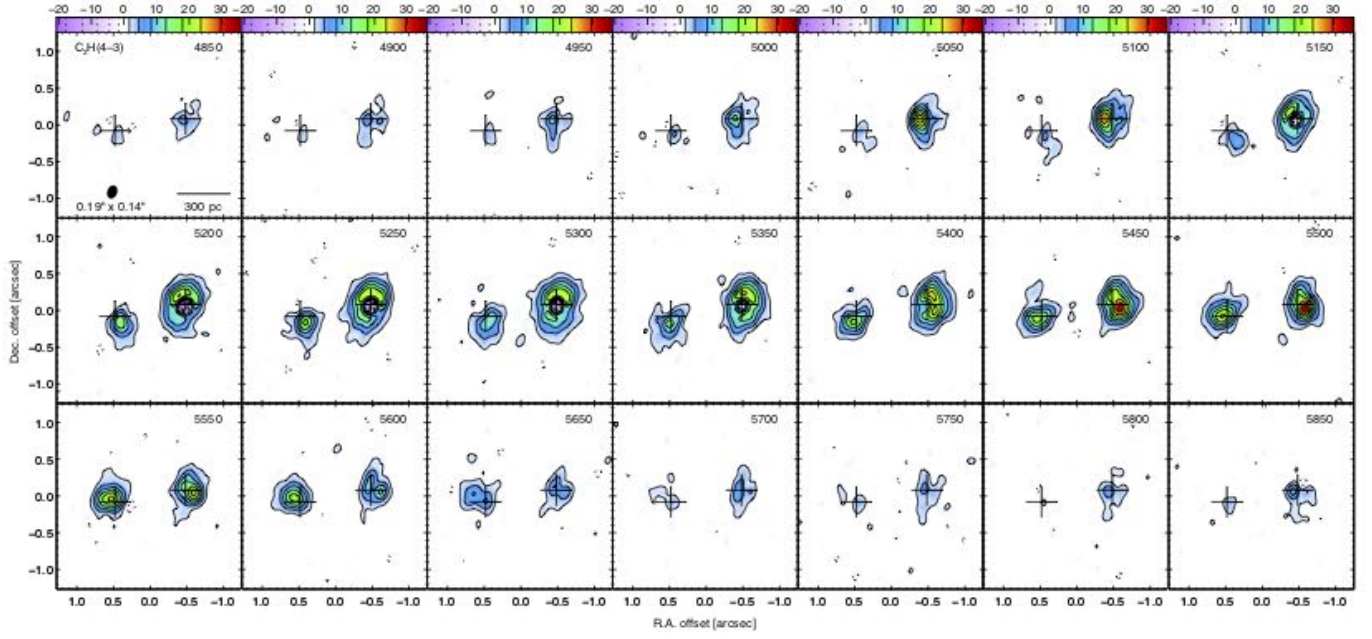
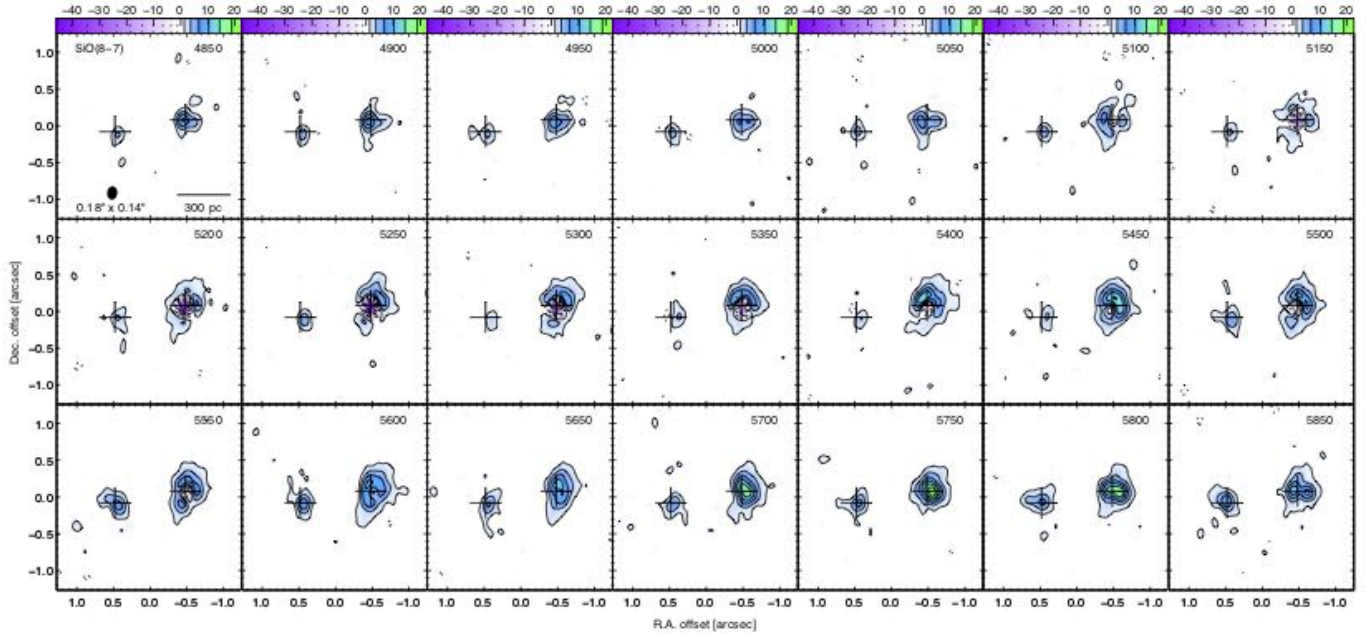


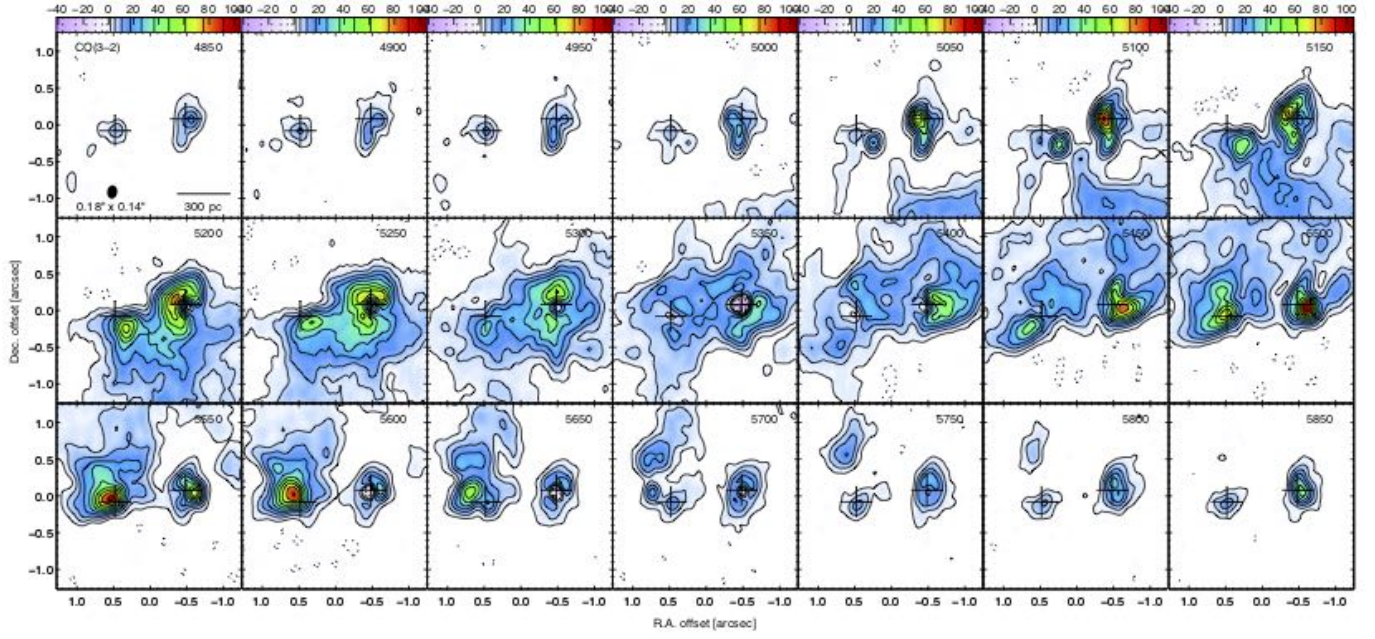
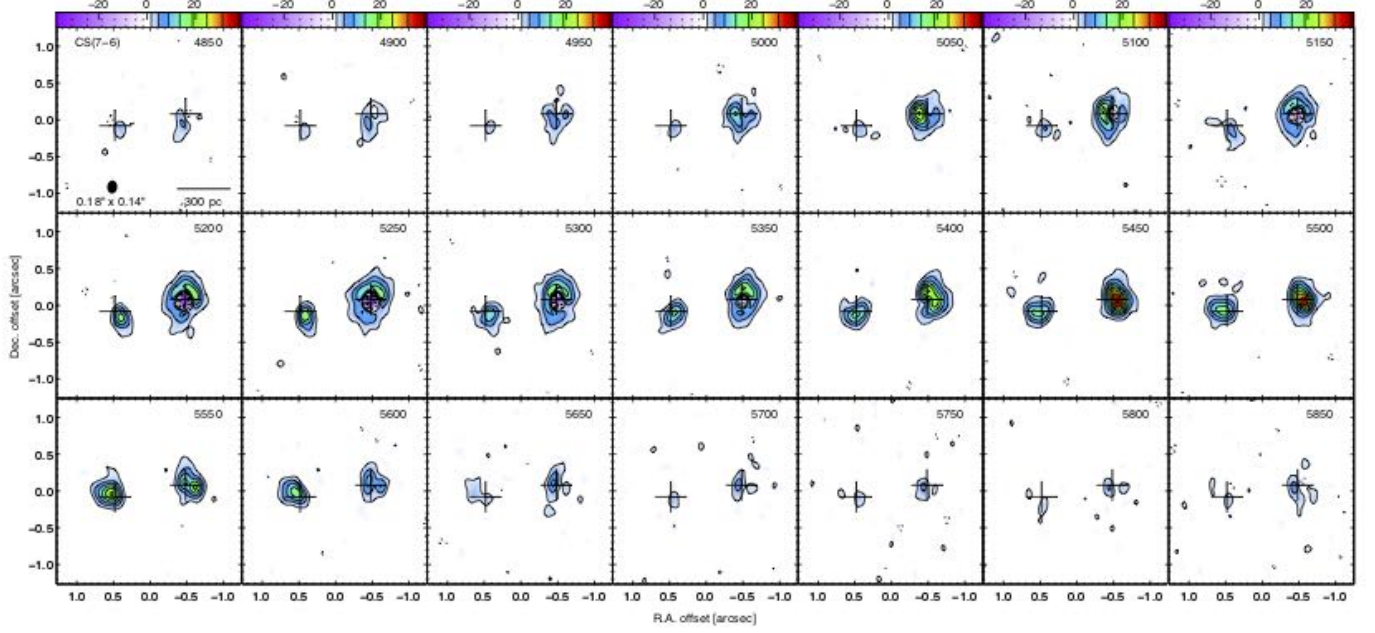
Figure 9. Arp 220 channel maps for major lines in Band 7. Contours are at $\pm 3n^p\sigma$ for $n = 1, 2, 3, \dots$, where the index p and the rms noise per 50 km s^{-1} channel σ are in Table 3. Negative contours are dashed. Velocity (LSRK, radio) in km s^{-1} is in the upper-right corner of each channel map. The crosses are at the continuum positions of the nuclei. The synthesized beam, labeled with its FWHM, is shown in the bottom-left corner of the first channel. The intensity color wedges are labeled with brightness temperature in Kelvin. Major line-blendings are indicated in sub-panel titles and more information is in Table 3.

(c) HCN($v_2 = 1, 4-3, l = 1f$) [blended with HCO⁺(4-3)]

(d) HCN(4-3)

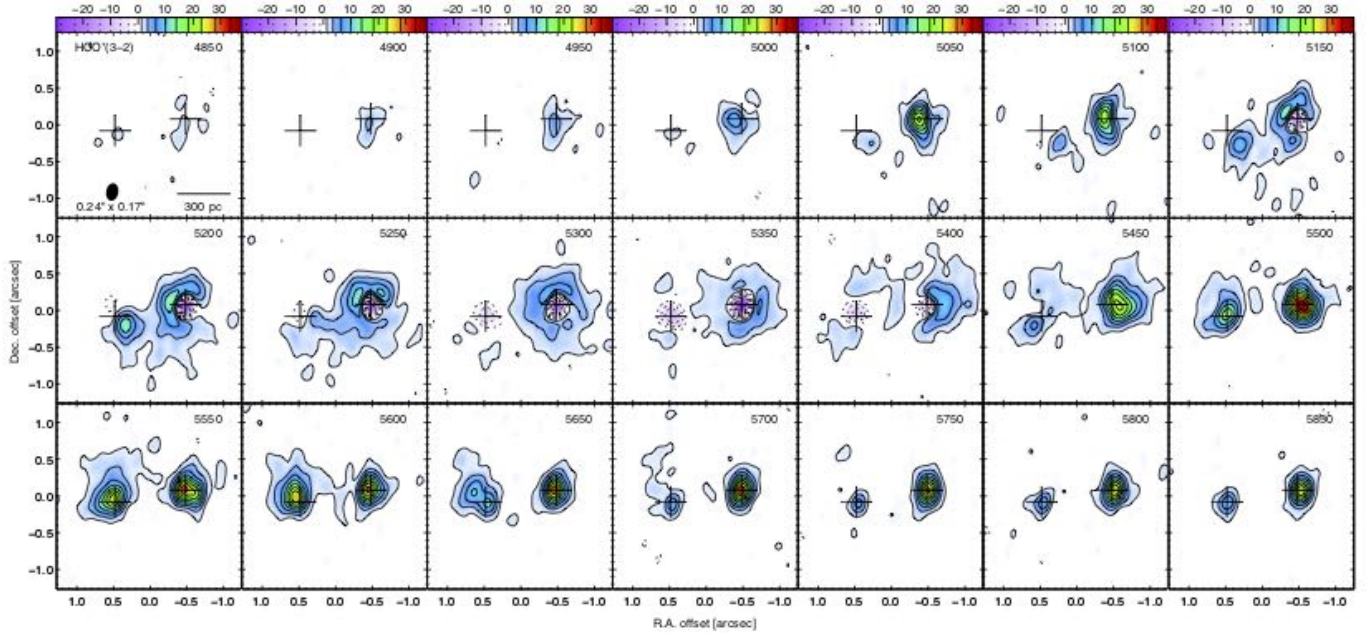
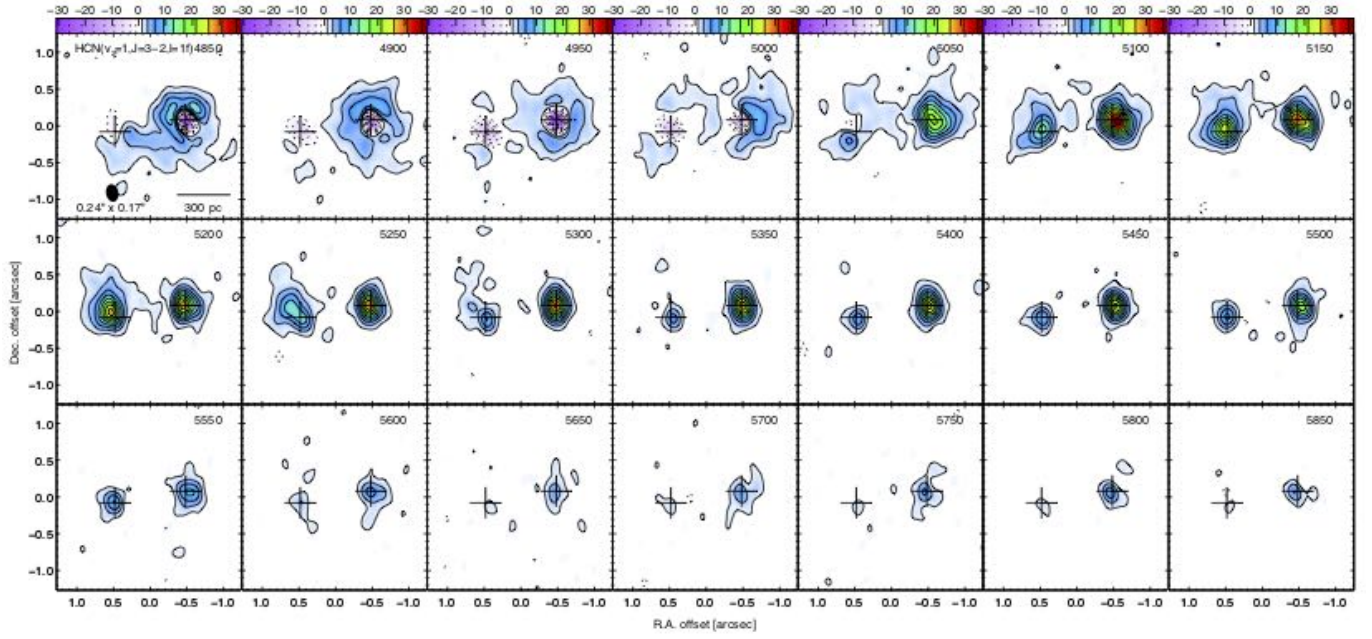
Figure 9 (continued).

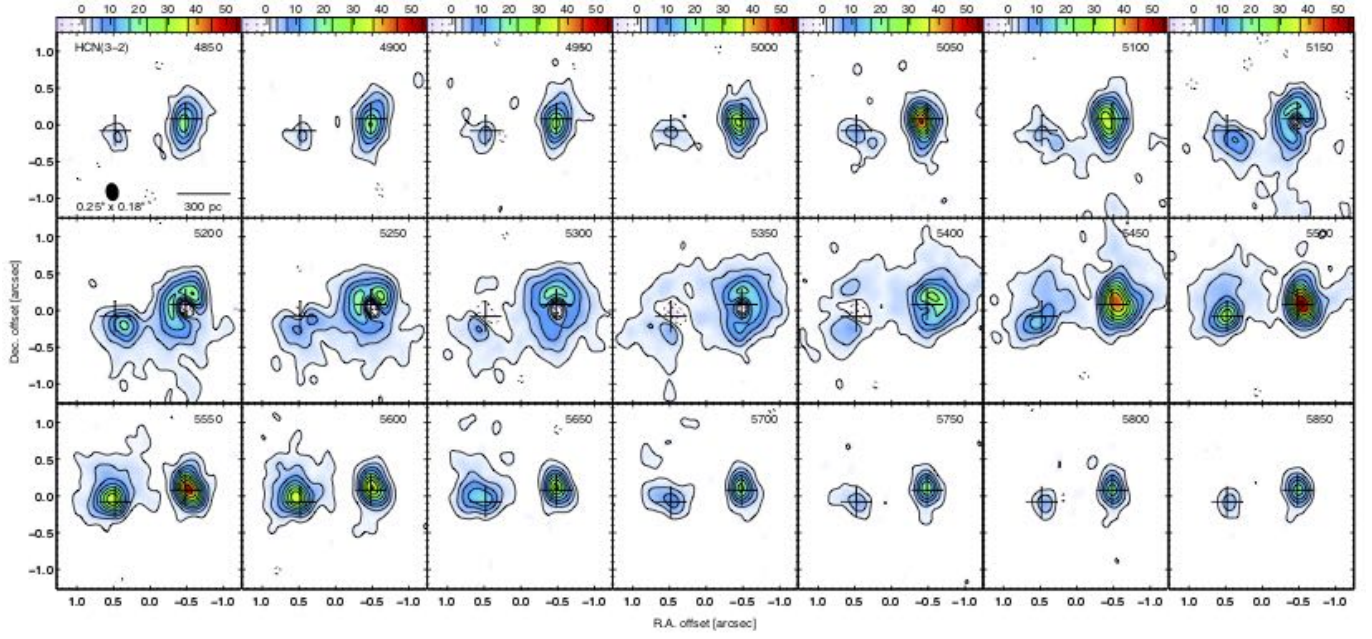
(e) $\text{C}_2\text{H}(4-3)$ (f) $\text{SiO}(8-7)$ [blended with $\text{H}^{13}\text{CO}^+(4-3)$]**Figure 9 (continued).**

(g) CO(3–2) [blended with H¹³CN(4–3)]

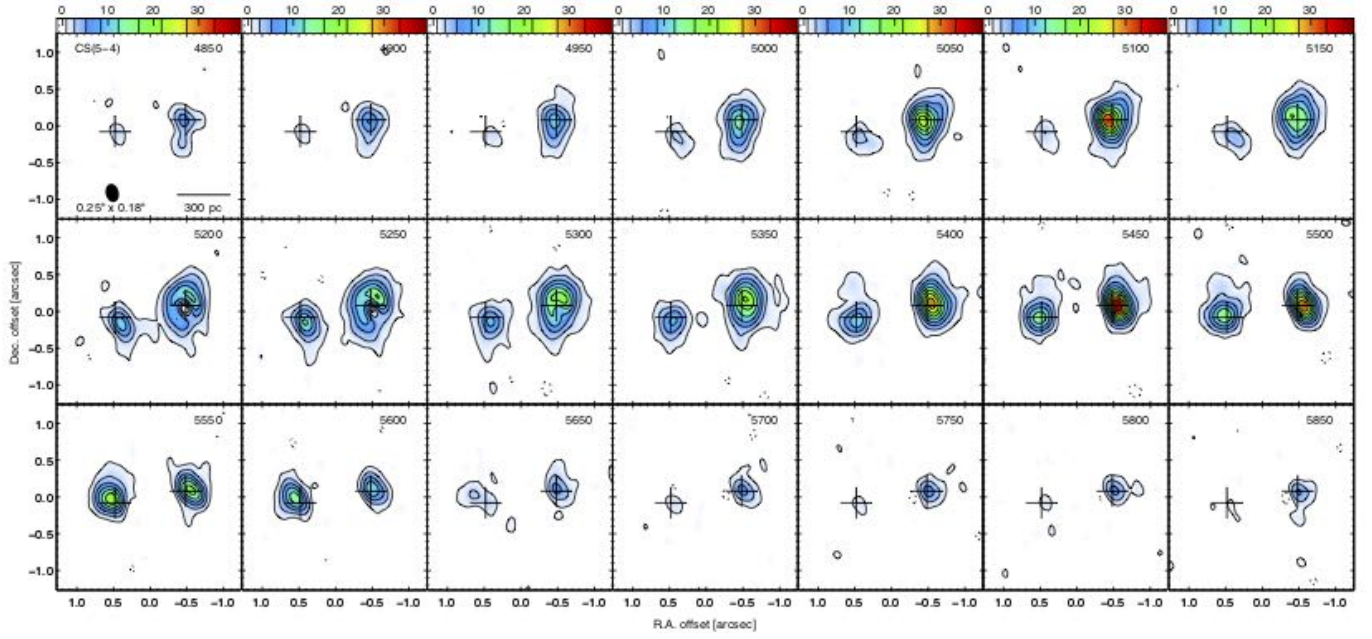
(h) CS(7–6)

Figure 9 (continued).

(a) $\text{HCO}^+(3-2)$ [blended with $\text{HCN}(v_2 = 1)$](b) $\text{HCN}(v_2 = 1, 3-2, l = 1f)$ [blended with $\text{HCO}^+(3-2)$]**Figure 10.** Arp 220 channel maps of 50 km s^{-1} width for major lines in Band 6. Other descriptions are the same as in Fig. 9.

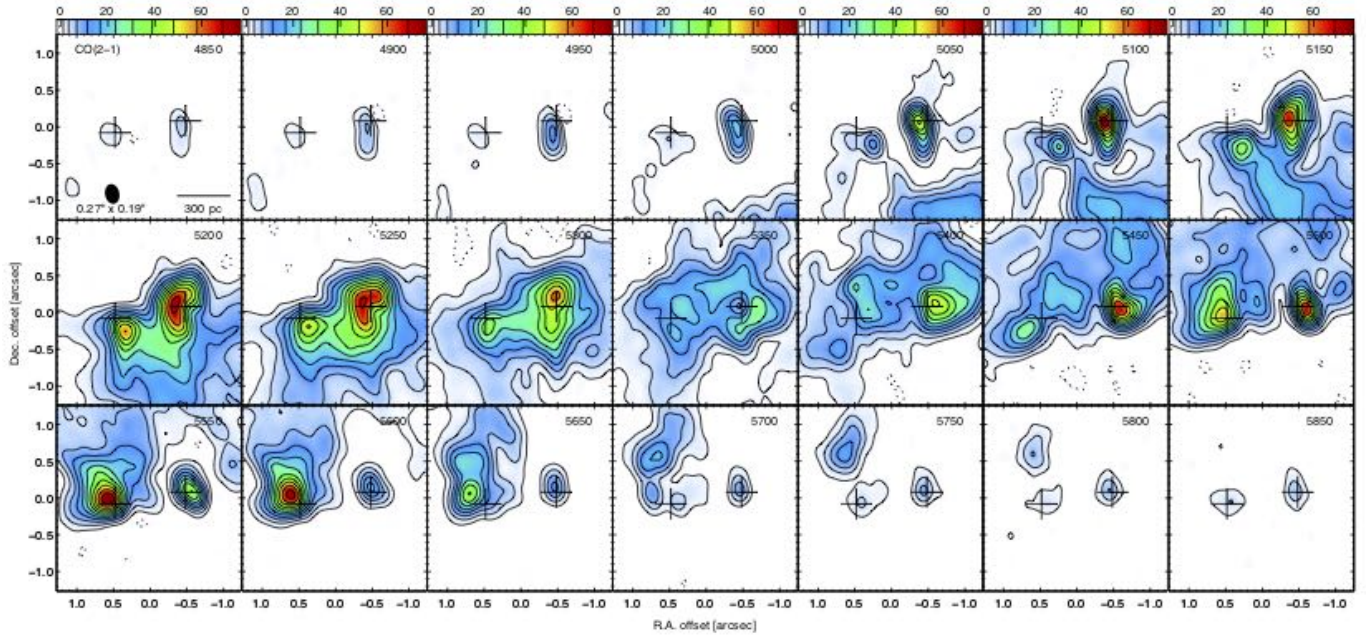


(c) HCN(3–2)



(d) CS(5–4)

Figure 10 (continued).



(e) CO(2-1)

Figure 10 (continued).

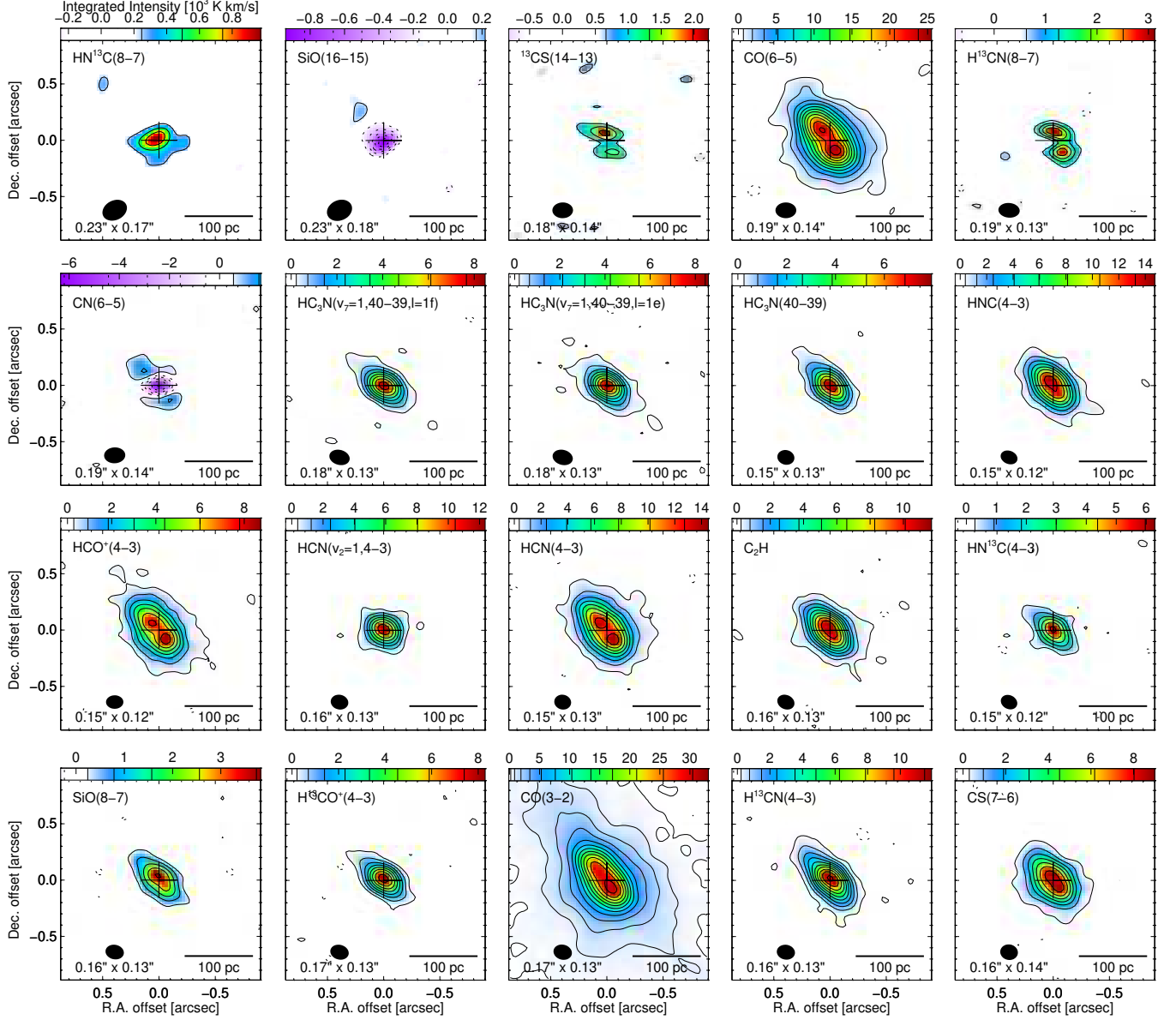


Figure 11. Integrated intensity maps of NGC 4418 for major lines in our ALMA observations. Integration is from the 1900 km s^{-1} channel to the 2300 km s^{-1} channel except the following; SiO(16–15) integration is from 1900 to 2150 km s^{-1} to reduce contamination by $\text{H}^{13}\text{CO}^+(8-7)$, $^{13}\text{CS}(14-13)$ is integrated over the 1950–2300 km s^{-1} channels, and $\text{H}^{13}\text{CN}(8-7)$ is integrated over the 1950–2250 km s^{-1} channels. Contours are at $\pm 3n^p\sigma$ for $n = 1, 2, 3, \dots$, where p is in Table 3 and σ is calculated from the noise in the channel maps in Table 3 and the number of integrated channels. Negative contours are dashed. In each panel, the cross is at the continuum position of the nucleus. The synthesized beam, labeled with its FWHM, is shown in the bottom-left corner.

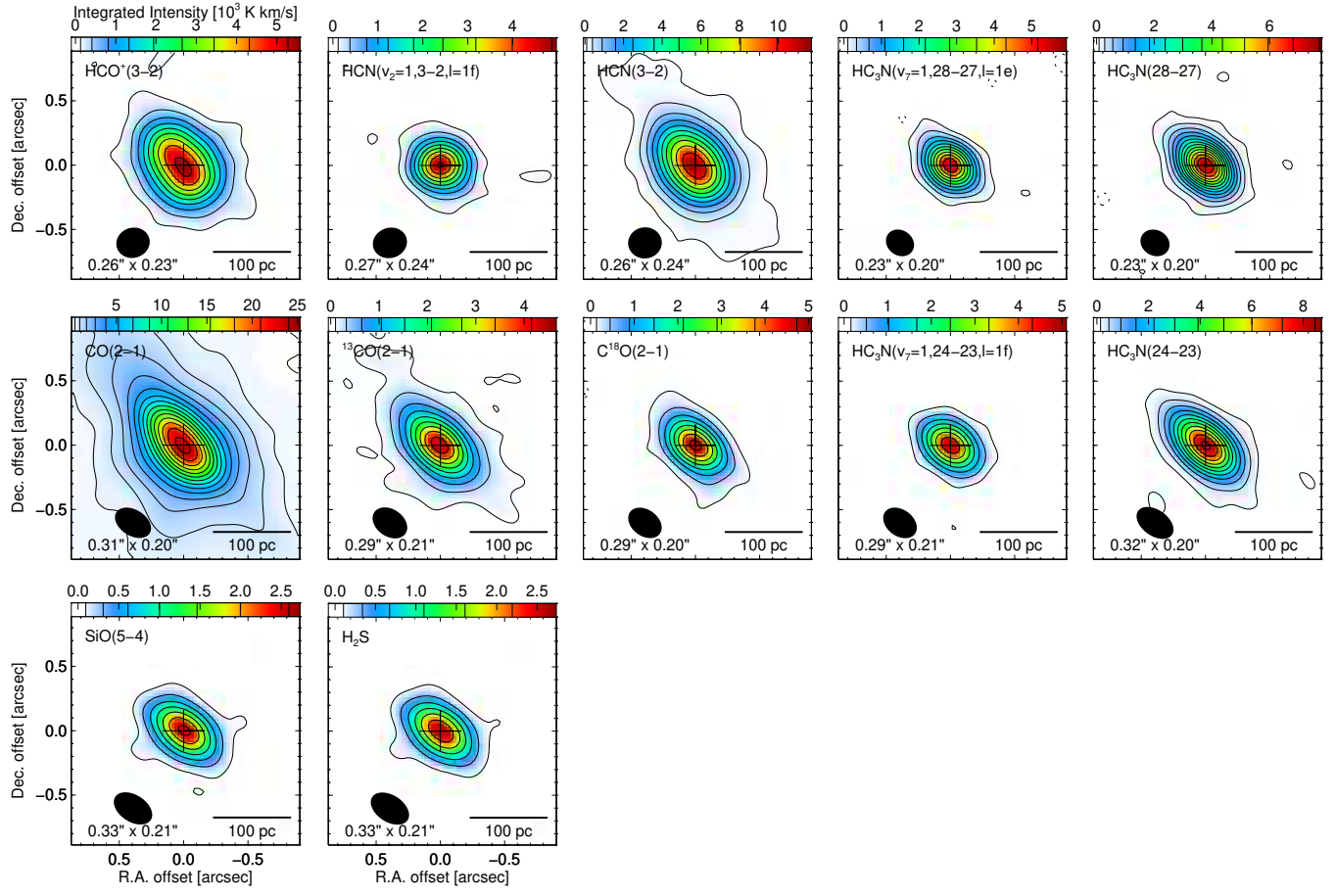


Figure 11 (continued).

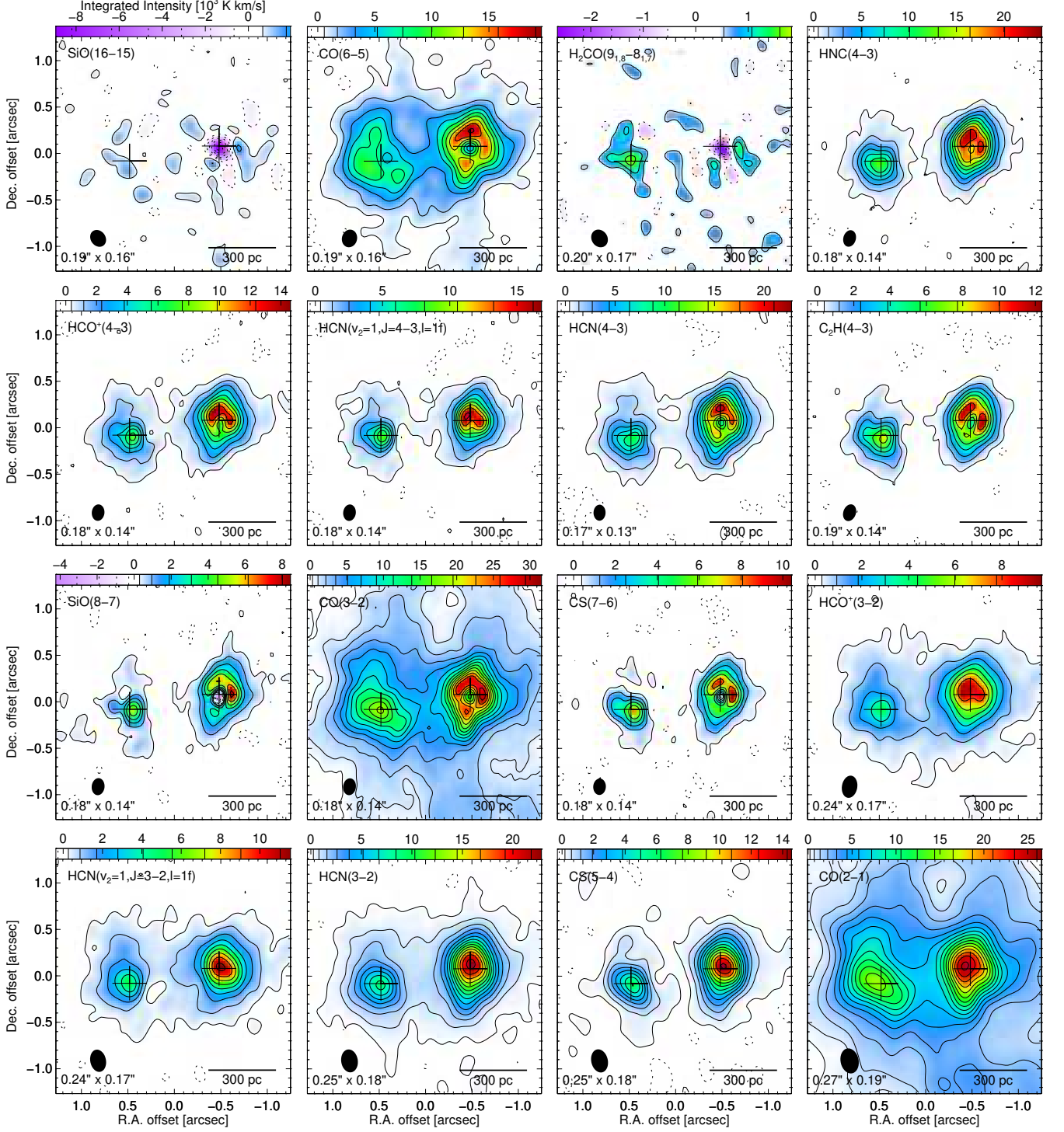


Figure 12. Integrated intensity maps of Arp 220 for major lines in our ALMA observations. Integration is over the 4850–5850 km s^{-1} channels, i.e., twenty-one 50 km s^{-1} channels. (See Table 3 for some contaminating lines in this velocity range). Contours are at $\pm 3n^p\sigma$ for $n = 1, 2, 3, \dots$, where p is in Table 3 and σ is calculated from the number of integrated channels (21) and $\sigma_{50 \text{ km/s}}$ in Table 3. Negative contours are dashed and the correction for the primary beam pattern is applied. In each panel, the crosses mark the continuum nuclei. The synthesized beam, labeled with its FWHM, is shown in the bottom-left corner.

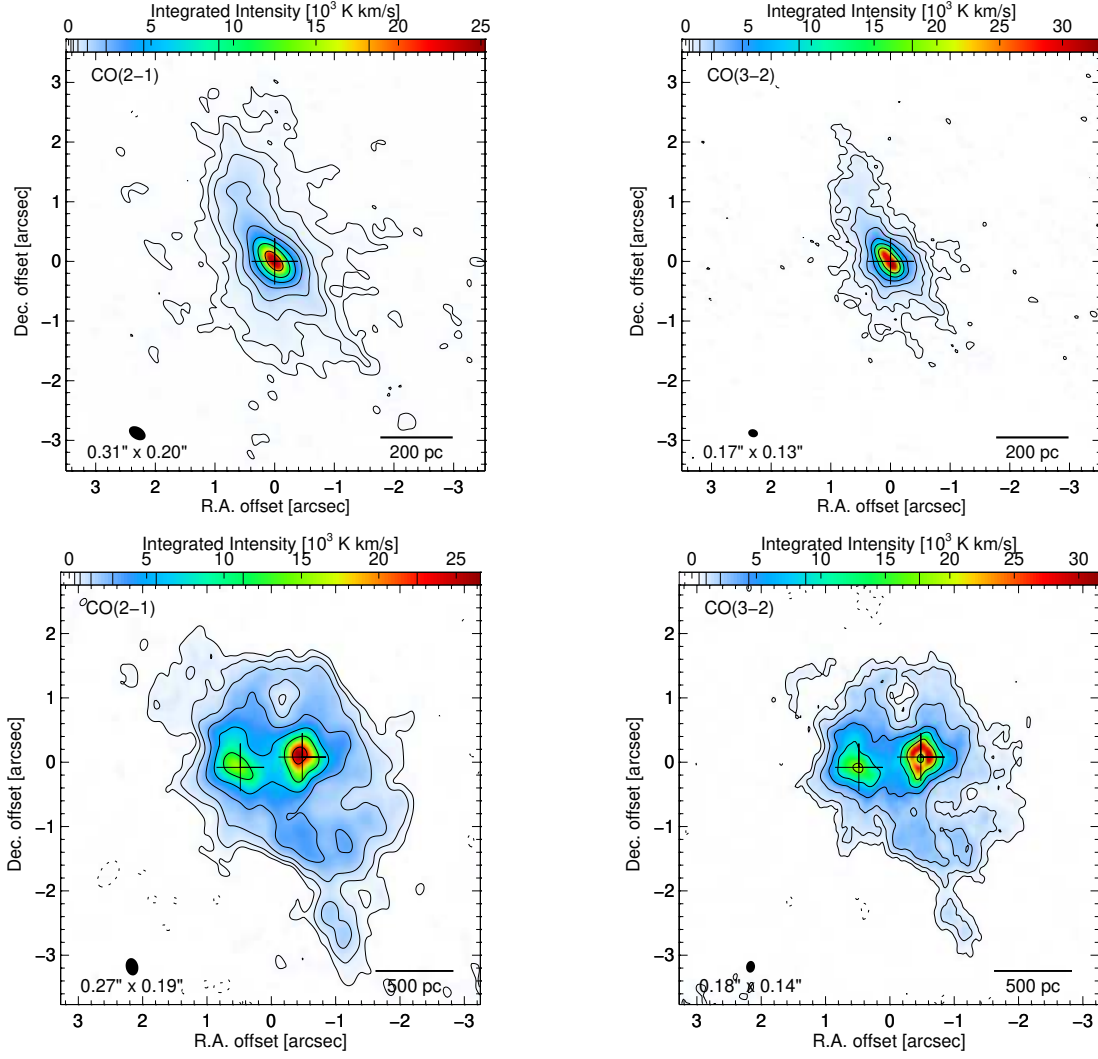


Figure 13. Integrated intensity images of NGC 4418 (top) and Arp 220 (bottom) in CO(2-1) and CO(3-2); the small-area images in Figs. 11 and 12 are plotted in a wider area. Attenuation by the primary beam pattern is corrected. Contours are at $\pm 3n^2\sigma$ for $n = 1, 2, 3, \dots$, where $\sigma = \sigma_{50\text{km/s}} \times (50 \text{ km s}^{-1}) \times \sqrt{N_{\text{ch}}}$, $\sigma_{50\text{km/s}}$ is in Table 3, and N_{ch} is 9 for NGC 4418 and 21 for Arp 220. Negative contours are dashed. Each nucleus is marked with a cross at its continuum position. The synthesized beam is shown in the bottom-left corner and labeled with its FWHM.

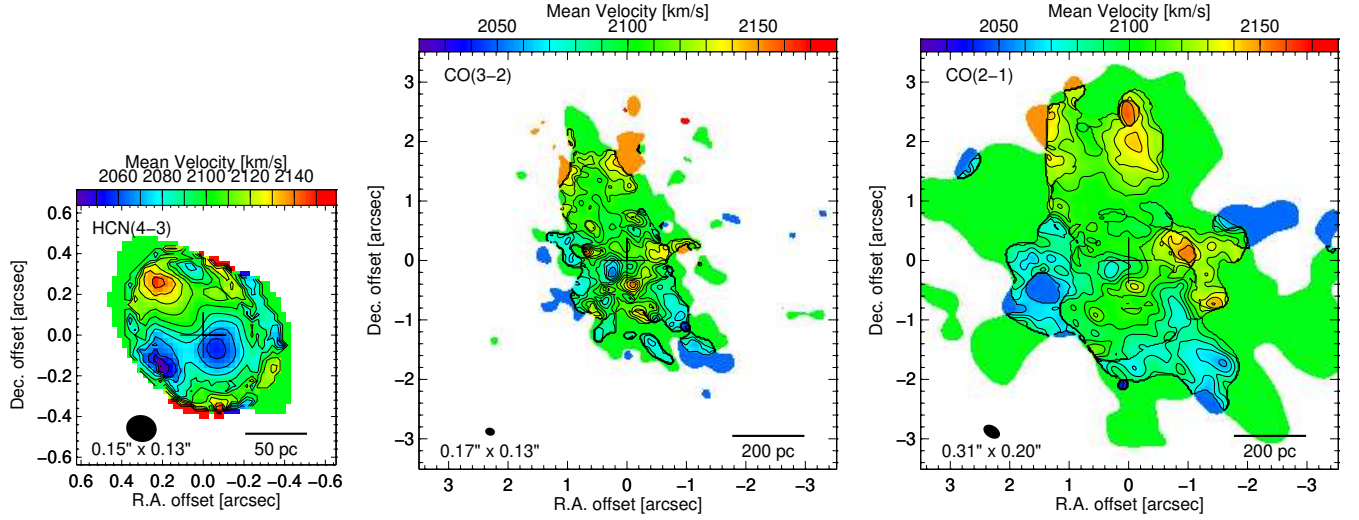


Figure 14. Mean velocity maps of NGC 4418 in HCN(4-3), CO(3-2), and CO(2-1). The cross in each map marks the position of the continuum nucleus.

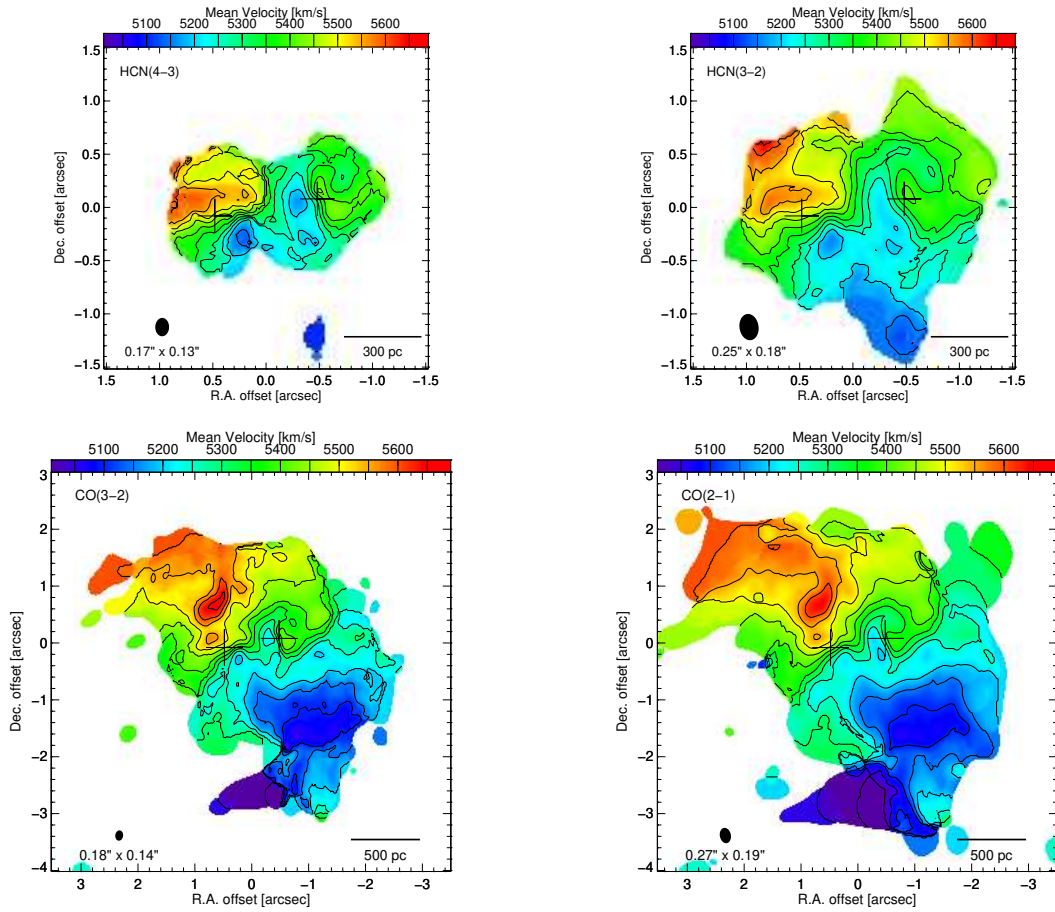


Figure 15. Mean velocity maps of Arp 220 in HCN(4-3), HCN(3-2), CO(3-2), and CO(2-1). The crosses mark the two nuclei.

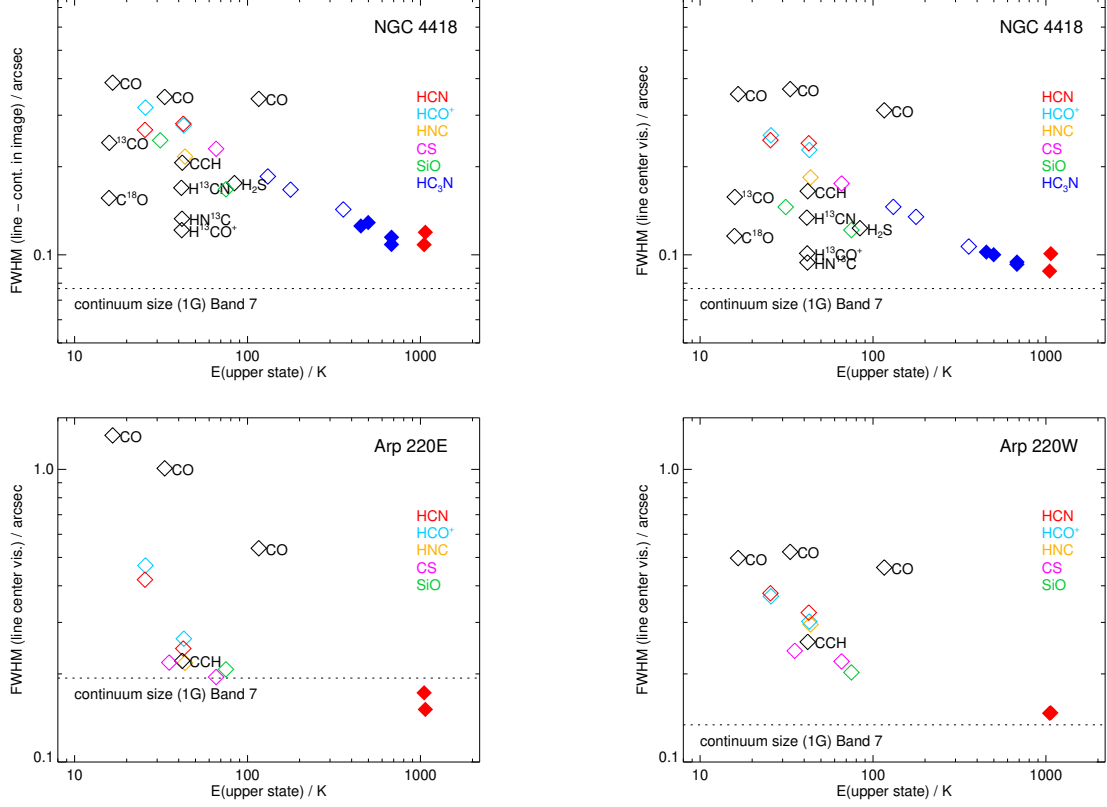


Figure 16. The extent of line emission in the nuclei of NGC 4418 and Arp 220 plotted against the upper-state energy of the individual lines. The lines are those in Bands 6 and 7 and CO(6–5). The top-left panel shows image-domain FWHM measured from the line integrated-intensity images in Figure 11. The top-right and bottom panels show FWHM measured from the visibility fitting without continuum subtraction in Paper I; channels within 100 km s^{-1} of the systemic velocities were averaged. All the FWHM sizes are the geometrical means of the deconvolved major- and minor-axis FWHM. Their formal errors are about the size of the symbols. Filled symbols are for lines in vibrationally excited states. Dotted horizontal lines are for the 1G (single-Gaussian) continuum size in Band 7 (Paper I). Note that each nucleus has a continuum structure that is more sharply peaked than the 1G fit. For example, the core component of the continuum emission of Arp 220E has an extent of $\sim 0''.07$.

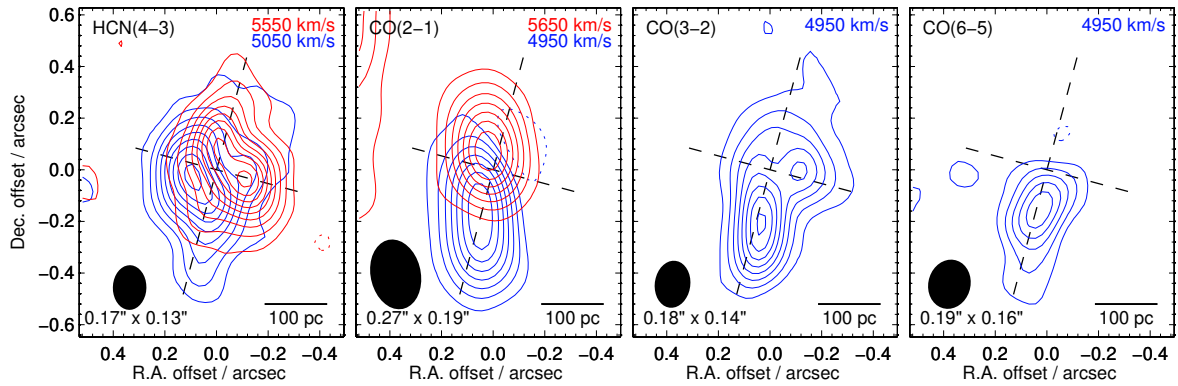


Figure 17. High-velocity gas around Arp 220W showing the bipolar outflow. The HCN(4–3) and CO(2–1) maps show emission at ± 250 and $\pm 350 \text{ km s}^{-1}$, respectively, from the fiducial velocity of the western nucleus, 5300 km s^{-1} . CO(3–2) and (6–5) data are only shown for $V_{\text{sys}} - 350 \text{ km s}^{-1}$ because of the contamination by H^{13}CN at $V_{\text{sys}} + 390 \text{ km s}^{-1}$. Each channel map integrates 50 km s^{-1} . Contours are at $\pm C n^p \sigma_{50 \text{ km/s}}$ with $(C, p) = (3, 1.5)$ for HCN, $(3, 1.3)$ for CO(2–1) and (3–2), and $(3, 1)$ for CO(6–5). Negative contours dashed. The rms noise, $\sigma_{50 \text{ km/s}}$, is in Table 3 for each line. The black dashed cross marks the continuum position of the western nucleus, which is the origin of the offset coordinates, and the major and minor axes of the continuum outflow measured at $\lambda = 3$ and 0.45 mm (major axis p.a. = -15° ; Sakamoto et al. 2021).

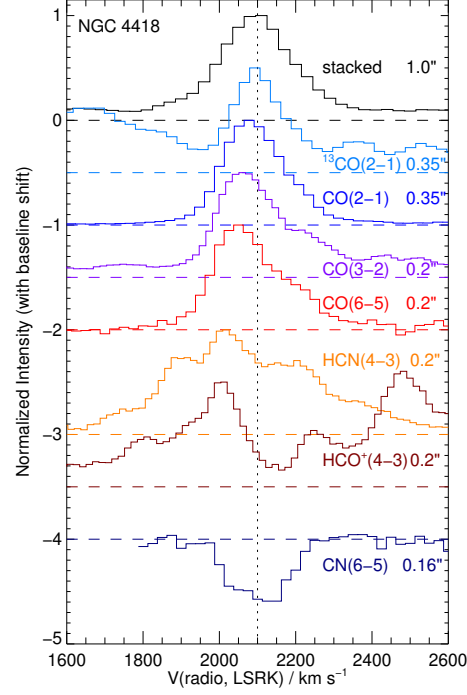


Figure 18. Continuum-subtracted line profiles toward the NGC 4418 nucleus. The top one is the normalized and stacked line profile in a $1''$ aperture and was used to decide V_{sys} in Fig. 1. The line profiles below, except for the one at the bottom, are from $0''.35$ (Band 6) and $0''.20$ (Band 7 and Band 9) beams. They are skewed in various degrees. Each spectrum, except for CN(6–5) at the bottom, is normalized by the peak intensity within 300 km s^{-1} from $V_{\text{sys}} = 2100 \text{ km s}^{-1}$. The CN(6–5) spectrum is normalized by the continuum intensity. The continuum is about 60% absorbed at the minimum. Baseline offsets in multiples of 0.5 are applied to reduce overlap between the spectra.

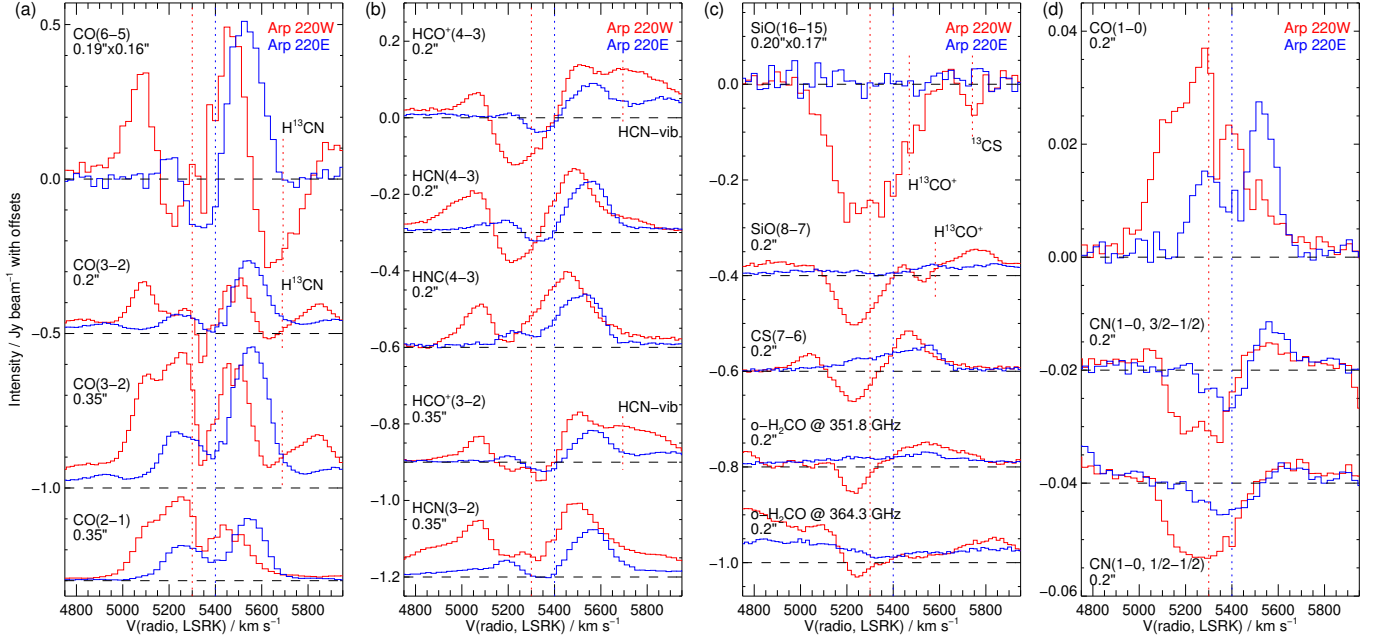


Figure 19. Continuum-subtracted line profiles toward the nuclei of Arp 220. The W nucleus is plotted in red and E in blue. Their fiducial systemic velocities at 5300 and 5400 km s⁻¹ are the vertical dotted lines in the same color scheme. The spectra are plotted with vertical shifts to reduce overlaps along with black dashed lines at the zero level. To the left of the individual spectra are the line names and the data resolution. In panel (c), ortho-H₂CO at 351.8 GHz is the (5_{1,5}–4_{1,4}) transition, and that around 364.3 GHz is a mixture of the (5_{3,2}–4_{3,1}) and (5_{3,3}–4_{3,2}) transitions. Major blended lines are marked with vertical dotted line segments in red at the systemic velocity of the W nucleus. CO(6–5) is blended with H¹³CN(8–7), CO(3–2) with H¹³CN(4–3), HCO⁺ lines with HCN(*v*₂=1, *l*=1f), SiO(16–15) with H¹³CO⁺(8–7) and ¹³CS(15–14), and SiO(8–7) with H¹³CO⁺(4–3). The spectra in panel (d) are from the 3 mm data in Sakamoto et al. (2017).

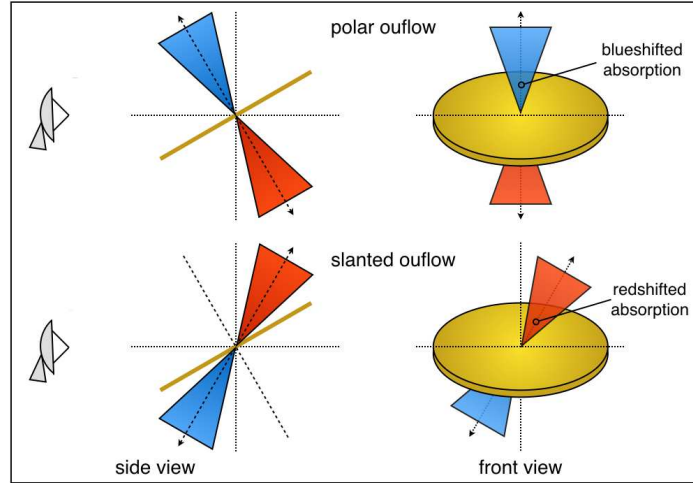


Figure 20. Configurations of a disk-outflow system and their effects on line absorption. To the left are the side views of two configurations of a bipolar outflow and a circumnuclear disk. To the right are their sky-plane projections. The outflow is along the polar axis of the disk in the top row while it is slanted in the bottom row. The outflow perpendicular to the disk has its approaching gas in front of the disk, and hence the outflow absorbs the disk light at blueshifted velocities. (If the disk is close to edge-on or the outflow opens wide enough, then a minor part of the foreground outflow can be redshifted while the majority is blueshifted.) For a slanted outflow that is not perpendicular to the disk, both blueshift and redshift are possible for the central velocity of the absorbing gas. In this illustration, the receding (i.e., redshifted) part of the slanted outflow is in front of the disk, and hence the line absorption by the outflow is redshifted.

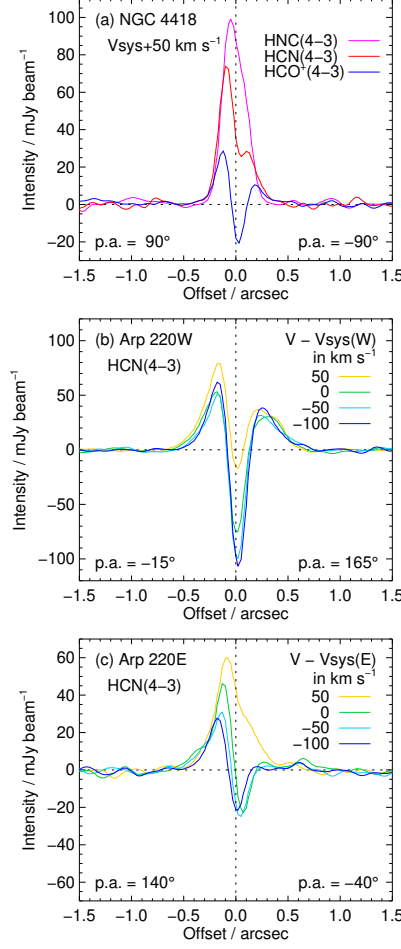


Figure 21. Lopsided line-intensity profiles across the three nuclei. The origin of the offset coordinate is at the continuum nucleus in each panel. Panel (a) is for NGC 4418 and shows the intensity profiles of three lines along p.a. = 90°. The profiles are from the channel maps at $V_{\text{sys}} + 50 \text{ km s}^{-1}$. Panel (b) is for Arp 220W and (c) for Arp 220E. Both show the HCN(4–3) intensity profiles along the minor axes of the two nuclear disks. The profiles are taken from the channel maps at (+50, 0, –50, –100) km s^{-1} from the systemic velocity of each nucleus.

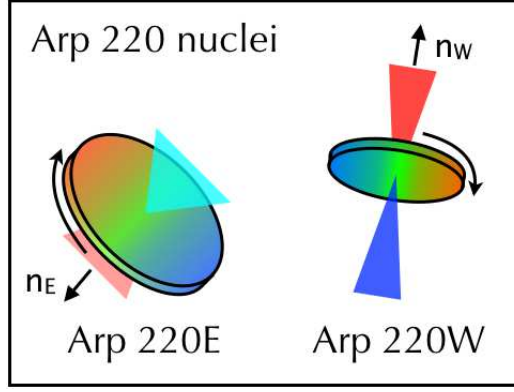


Figure 22. A schematic diagram of Arp 220 for the configuration of its nuclear disks and outflows. The color coding is blue(red) for blue(red)shifted gas and green for the gas near the systemic velocities of the individual nuclei. (Arp 220E is about 100 km s^{-1} more redshifted than Arp 220W.) The disk major axes and axial ratios are from our fitting of supernova distributions and 3 and 0.4 mm continuum emission (Sakamoto et al. 2021); both nuclei have inclinations $\gtrsim 60^\circ$. The near- and far-sides of the nuclear disks are determined from the spatially-lopsided line absorption explained in the main text. The normalized angular-momentum vectors of the disks are shown as \mathbf{n}_E and \mathbf{n}_W . The nuclear disks are in counter-rotation. In Arp 220E, only the blueshifted outflow has been detected; the redshifted lobe here is our prediction. We caution that this illustration is highly simplified for clarity. For example, the actual nuclear disks may well be thicker, distorted, and interacting with the surrounding outer disk.

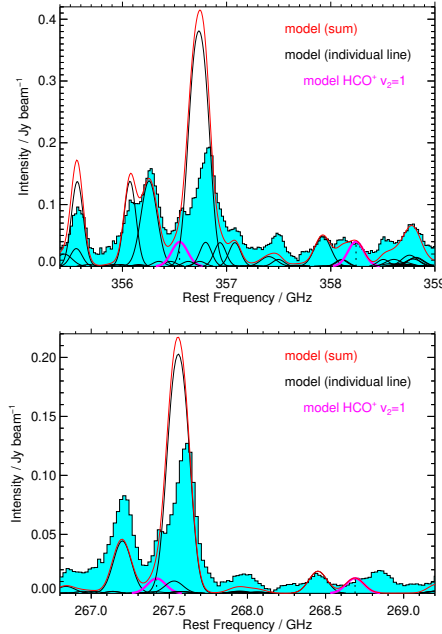


Figure 23. NGC 4418 spectrum around HCO^+ J=4–3 and 3–2 transitions. Our model fit in red is overlaid on the observed spectrum in light blue. Individual lines in the model are shown in black, and magenta for the vibrationally excited HCO^+ .

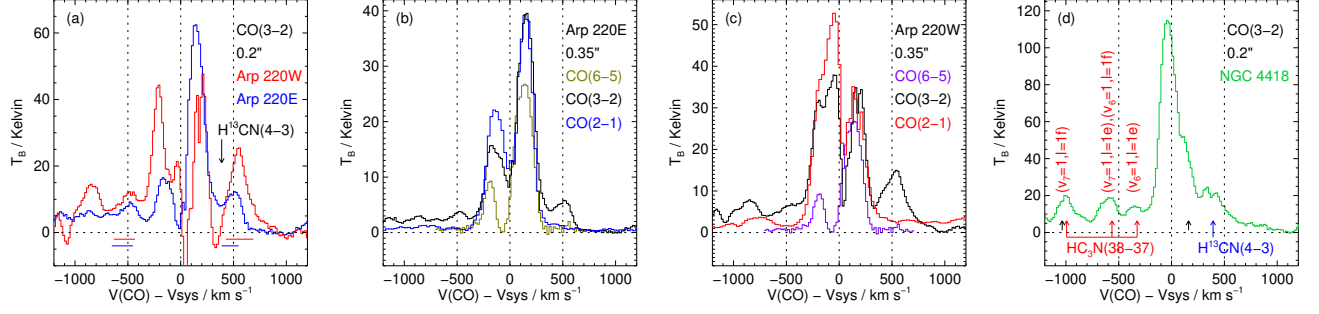


Figure 24. Line-blending around CO(3–2) to affect the search for high-velocity gas. (a) CO(3–2) spectra of the two Arp 220 nuclei; red for the W nucleus and blue for the E nucleus. The offset velocities are from the systemic velocity of each nucleus. The short horizontal bars around $\pm 500 \text{ km s}^{-1}$ mark the putative high-velocity emission that Wheeler et al. (2020) identified in their CO(3–2) data. Our spectra confirm the peaks in both nuclei. A black arrow is where $\text{H}^{13}\text{CN}(4-3)$ would be centered if its profile were symmetric. (b) Arp 220E spectra of CO in $J=6-5$, $3-2$, and $2-1$. The $\pm 500 \text{ km s}^{-1}$ features in CO(3–2) are absent in CO(2–1) and (6–5). (c) Same as (b) but for Arp 220W. (d) CO(3–2) spectrum of NGC 4418. The feature near $+400 \text{ km s}^{-1}$ is $\text{H}^{13}\text{CN}(4-3)$, whose double-peak may be due to a slight absorption. In negative CO velocities are three peaks due to four transitions of vibrationally excited HC_3N . The main text explains how $\text{H}^{13}\text{CN}(4-3)$ and vibrationally-excited $\text{HC}_3\text{N}(38-37)$ lines form the $\pm 500 \text{ km s}^{-1}$ features in the CO(3–2) spectra of Arp 220. For completeness, two short black arrows indicate the locations of $\text{H}^{13}\text{CO}^+(4-3)$ around -1030 km s^{-1} and $\text{HC}_3\text{N}(38-37)$ at $+160 \text{ km s}^{-1}$.

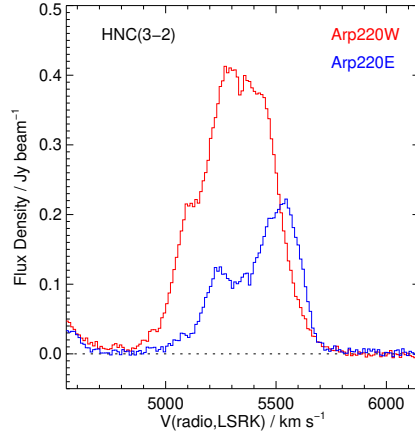


Figure 25. HNC(3–2) line profiles toward the Arp 220 nuclei. The continuum-subtracted data are from our companion spectral scan and have $0''.65$ and 11 km s^{-1} resolutions. The peak brightness temperature of the line is 16 K for the western nucleus.

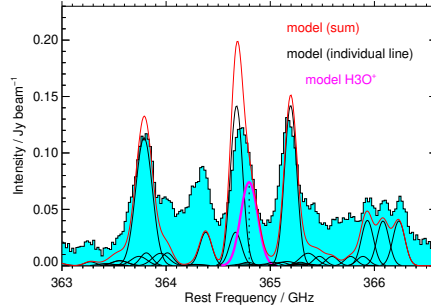


Figure 26. NGC 4418 spectrum around the $\text{H}_3\text{O}^+(3_2^+-2_2^-)$ line ($f_{\text{rest}} = 364.797 \text{ GHz}$). Our model fit in red is overlaid on the observed spectrum in light blue. Individual lines in the model are shown in black and, for the H_3O^+ , magenta.

!bht

Table 4. Species in the NGC 4418 spectral model

N_{atom}	Species
2	CO, ^{13}CO , C^{18}O , CO^+ , CS, ^{13}CS , ^{13}CN , NO, NS, N^{34}S , SiO, ^{29}SiO , ^{30}SiO , SO
3	H_2S , HCN, H^{13}CN , HC^{15}N , HNC, HN^{13}C , H^{15}NC , HCO^+ , H^{13}CO^+ , HC^{18}O^+ , HCO, HOC^+ , HCS^+ , CCH, ^{13}CCH , C^{13}CH , CCS, OCS
4	H_3O^+ , H_2CS , HNCO, p- H_2CO , o- H_2CO , C_3H , HOCO^+
5	CH_2NH , HC_3N , c- C_3H_2 , H_2CCN , NH_2CN , H^{13}CCCN , HC^{13}CCN , HCC^{13}CN
6	CH_3OH , CH_3CN , $\text{CH}_3^{13}\text{CN}$, $^{13}\text{CH}_3\text{CN}$
7	CH_3CCH , $\text{C}_2\text{H}_3\text{CN}$
9	$\text{C}_2\text{H}_5\text{CN}$, $\text{C}_2\text{H}_5\text{OH}$

NOTE— Major molecules can be absent if they have no transition in our spectral coverage.
Vibrationally excited states are in our model for HCN, HCO^+ , HC_3N , and CH_3CN .

APPENDIX

A. INITIAL SPECTRAL FITTING OF NGC 4418

Figure 27 shows our initial fitting to the $0''.35$ -beam spectrum toward the nucleus of NGC 4418. In each of the three panels, the top sub-panel shows the observed (light blue) and model (red) spectra. The middle sub-panel shows their difference (i.e., observed – model). The bottom sub-panel shows individual line transitions at their rest frequencies without smoothing them with the line widths. The modeling procedure is in Section 3.2, and the model line-emitting region was a Gaussian of $0''.3$ FWHM without continuum emission. Table 4 lists 55 species in our model. Four of them have their vibrationally excited states included. Table 5 lists 255 lines in the frequency ranges of our observations. It shows those lines having peak model intensities ≥ 10 mJy beam $^{-1}$ in Band 7 and ≥ 3 mJy beam $^{-1}$ in Band 6; the thresholds are about 3σ in our data. Our model spectral synthesis had no cutoffs. The table also gives the velocity-integrated intensity in our model for each line. Note that an entry here does not necessarily mean detection of the particular transition in our data. Since we fitted our entire spectrum rather than individual lines, the entry may be due to other brighter transitions of the same species and excitation modeling.

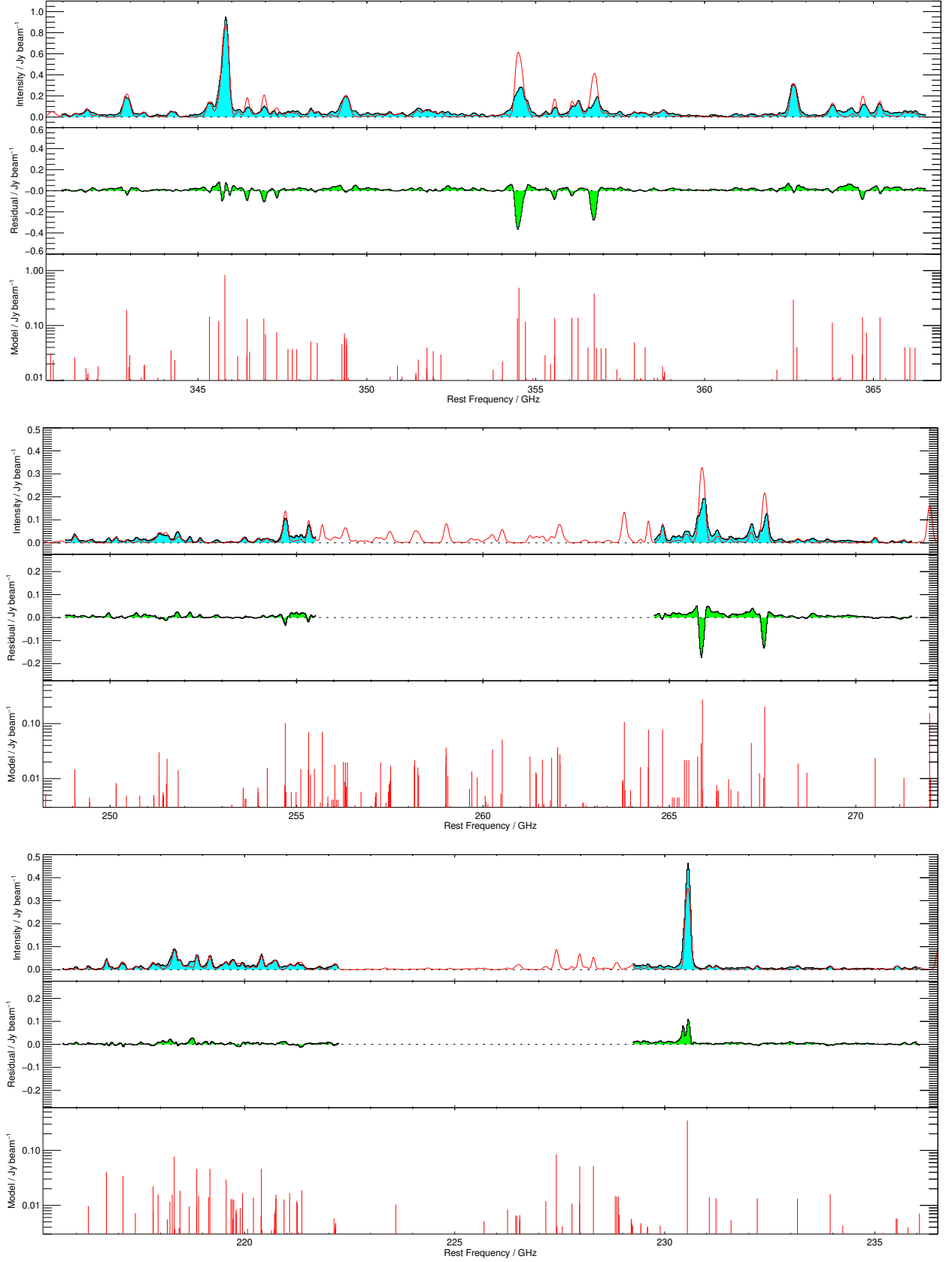


Figure 27. Spectral fitting of NGC 4418. In each panel, the top sub-panel shows in light-blue the continuum-subtracted spectrum at $0''.35$ and 20 MHz resolutions; it also shows the model spectrum fitted to the data in red. The middle sub-panel shows the fitting residual (i.e., observed – model spectrum). The bottom sub-panel shows peak intensities of the individual lines in the model.

Table 5. Initial Spectral Model of the nucleus of NGC 4418

f_{rest}	I_ν	S	Species
(1)	(2)	(3)	(4)
341.35083	26.2	4.3	HCS+
341.68257	16.8	2.7	CH ₃ CCH
341.71509	10.9	1.8	CH ₃ CCH
341.73461	12.8	2.1	CH ₃ CCH
341.74111	13.5	2.2	CH ₃ CCH
342.03807	18.2	2.9	NH ₂ CN
342.88300	192.3	37.2	CS
342.94437	17.7	2.8	H ₂ CS
342.97911	29.1	4.7	Si-29-O
343.31964	11.3	1.8	H ₂ CS
343.40812	19.1	3.1	H ₂ CS
343.41233	19.1	3.1	H ₂ CS
343.81076	11.3	1.8	H ₂ CS
344.20032	35.6	5.8	HCN-15
344.31061	23.6	3.8	SO
345.33976	144.1	26.0	HC-13-N
345.60901	118.8	19.4	HC ₃ N, v=0
345.63213	10.7	1.3	HC ₃ N, v5=1/v7=3
345.79599	831.9	192.0	CO
345.82329	10.6	1.7	NS
345.82467	10.7	1.3	HC ₃ N, v5=1/v7=3
346.17440	27.8	3.3	HC ₃ N, v6=1
346.22014	10.6	1.7	NS
346.44620	27.8	3.3	HC ₃ N, v6=1
346.45573	132.5	15.7	HC ₃ N, v7=1
346.52848	33.4	5.4	SO
346.94912	132.9	15.7	HC ₃ N, v7=1
346.99834	69.3	11.6	HC-13-O+
347.33063	76.1	12.8	SiO
⋮	⋮	⋮	⋮
⋮	⋮	⋮	⋮

NOTE— (1) Rest frequency in GHz. (2) Peak line intensity (in mJy beam⁻¹) of the model for our 0.''35 spectrum. (3) Velocity integrated line intensity (in Jy beam⁻¹ km s⁻¹) in the model. (4) Species (with vibrational states when necessary). The full contents of this table are provided online.